Experimental and Computational Investigations of Catalytic C_1 Upgrading Reactions

by

Gizem Ozbuyukkaya

B.S. in Chemical Engineering, Bogazici University

M.S. in Chemical Engineering, Bogazici University

Submitted to the Graduate Faculty of the

Swanson School of Engineering in partial fulfillment

of the requirements for the degree of

Doctor of Philosophy

University of Pittsburgh

2021

UNIVERSITY OF PITTSBURGH

SWANSON SCHOOL OF ENGINEERING

This dissertation was presented

by

Gizem Ozbuyukkaya

It was defended on

December 10, 2020

and approved by

Robert S. Parker, Ph.D., Professor, Department of Chemical and Petroleum Engineering

Robert M. Enick, Ph.D., Professor, Department of Chemical and Petroleum Engineering

Nathaniel L. Rosi, Ph.D., Professor, Department of Chemistry

Dissertation Director: Götz Veser, Ph.D., Professor, Department of Chemical and Petroleum Engineering

Experimental and Computational Investigations of Catalytic C_1 Upgrading Reactions

Gizem Ozbuyukkaya, PhD

University of Pittsburgh, 2021

Technological advances in horizontal drilling and fracking enabled a steep increase in recoverable natural gas reserves. The abundance of natural gas creates a strong incentive to utilize methane beyond combustion by converting it to higher-value chemicals. However, C_1 upgrading reactions are often challenging due to poor activity/selectivity and feasibility. This work aims to improve our understanding of such reactions via (i) increasing fundamental insights into the reaction mechanism for the rational design of catalytic processes, and (ii) improving the accuracy of the kinetic description of complex reaction systems. Herein, we studied oxidative coupling of methane (OCM) to ethylene, and synthesis of methanethiol from methanol and hydrogen sulfide. Initially, we experimentally investigated the unsteady-state kinetics of OCM over Mn_xO_y-Na_2WO_4 based catalysts to elucidate the role of metal oxide centers. By exploring the transient behavior of the catalyst under reducing conditions, we correlated lattice oxygen consumption and phase changes of each metal oxide to the formation of different carbon species. We found that while the presence of Mn-oxide is critical for methane activity, the gas phase dehydrogenation of ethane is the key step to form ethylene. Selective hydrogen removal on tungstate is found to promote higher C_2 yields, which could provide a new direction for rational catalyst design. Next, a statistical regression methodology is applied towards estimating kinetic parameters for methanol thiolation on a commercial alumina-based catalyst, yielding good agreement with experimental data and a considerable improvement over parameters predicted via conventional regression. The computational framework for modeling and optimization of reactors for a large-volume process is developed and used towards determining operating conditions and reactor design to achieve >90% methanethiol yields with negligible pressure drop. The general applicability of the implemented parameter estimation method for derivation of robust kinetics is further evaluated using synthetic data for a simple model reaction. The method is found to have similar or better accuracy in predicting true kinetics from limited and/or noisy data than advanced optimization routines with considerably less computation cost. Overall, this dissertation aims to provide both experimental and computational tools and insights to improve our understanding of reaction kinetics involving C_1 chemistry.

Table of Contents

List of Tables

List of Figures

1.0 Introduction

Global recoverable natural gas reserves have been rapidly increasing in recent decades due to the technological advances in horizontal drilling and hydraulic fracking, which is a trend that is projected to stay well into the 21st century[1,2]. Nowadays, natural gas, consisting primarily of methane, is typically used as a source of energy for heating and electricity generation. However, the increased abundance of natural gas combined with low prices creates a strong incentive to utilize methane by converting it to industrially relevant, higher-value chemicals[3]. One such example is ethylene, which is the largest petrochemical produced in the world by volume, since it is the building block for a vast array of chemicals from adhesives to solvents, paints, and plastics[4,5]. Ethylene is commercially predominantly produced via steam cracking of naphtha, a petroleum-based feedstock[3,6]. This process is considerably energy intensive as it involves thermal cracking of longer carbon chains at high temperatures. In addition, since the feedstock is a by-product of the petroleum industry, crude oil availability and price is anticipated to affect the feasibility of the process in near future.

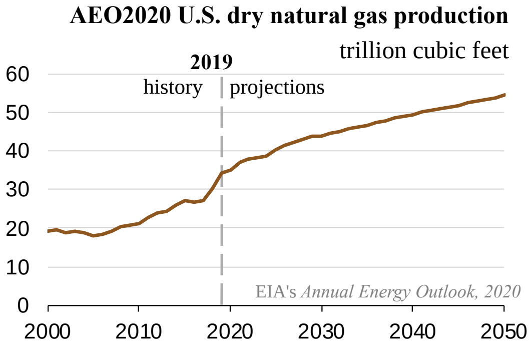

Figure 1 History and projections of U.S. natural gas production[1]

---

[1] Annual Energy Outlook 2020, U.S. Energy Information Administration (EIA)

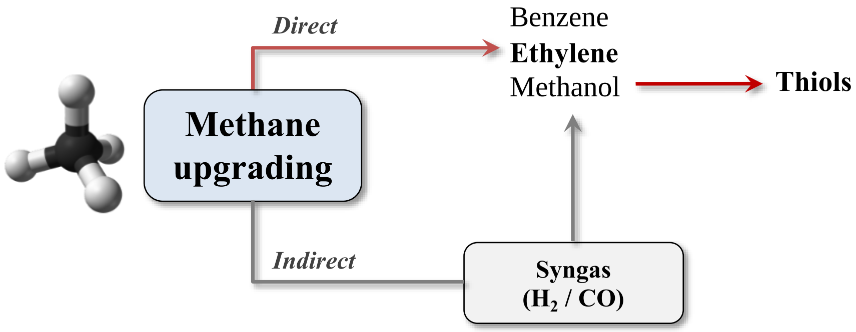

Figure 2 Simplified schematics of methane upgrading routes

An alternative route to producing ethylene is the “oxidative coupling of methane” (OCM), in which methane is directly converted to ethylene in a single, exothermic step at temperatures above 700°C[6-8]. Although this reaction has been studied for many decades, it is lacking an efficient catalyst that can procedure high ethylene yields, which makes the industrial-scale realization of OCM challenging[9]. Current economic estimations state that for the OCM reaction to be an economically feasible alternative to steam cracking, at least 30% per-pass ethylene yield should be achieved at the end of the reactor[10,11]. A large number of active materials have been tested such as Li/MgO, La_2O_3, and Mn/Na_2WO_4[10]. Amongst the catalyst tested, $Na_2WO_4/Mn/SiO_2$ has been shown to have good performance and stability by several publications, although different assessments are reported regarding the nature of the active site[12]. Therefore, we set out to experimentally investigate the OCM reaction over the $Mn\text{-}Na_2WO_4$ catalyst system to identify methane activation and conversion pathways leading to high C_2 selectivity. Earlier work on OCM proposed that the metal oxide catalyst provides its lattice oxygen via a Mars-Van Krevelen mechanism to activate methane by breakage of the C-H bond at 700-900°C, and the consumed lattice oxygen is replenished by gas phase oxygen in the consequent step[13,14]. Hence in this work, fixed-bed continuous flow experiments are carried out by feeding separate pulses of air and methane to the reactor, instead of co-feeding them, where metal oxides act as oxygen reservoirs or "oxygen carriers". Experiments conducted in the absence of molecular oxygen in the feed enables us to focus on surface-initiated reactions and observe reaction pathways that are not readily discernible otherwise. By exploring the transient behavior of the catalyst under reactive conditions, we can correlate lattice oxygen consumption and phase changes of the metal oxide center with the formation of different C_2 and CO_X species. Single component MnO_2/MgO and Na_2WO_4/MgO catalysts are also studied via thermogravimetric and fixed-bed reactor studies to determine their baseline methane activity and C_2 selectivity. Finally, the synergistic effect and lattice oxygen sharing mechanism between MnO_2 and Na_2WO_4 is examined by physically mixing individually synthesized samples of these two metal oxides and comparing their catalytic performance to the conventional Mn-Na_2WO_4 mixed-oxide catalyst. The results and outcomes of this work aim to enhance our understanding of the OCM reaction over the Mn-Na_2WO_4 catalyst system and suggest new directions for rational catalyst design to further improve C_2 yields towards the economical window.

In the next part, another value-added chemical formed through methane upgrading is studied. Methanethiol, an aliphatic thiol with the formula CH_3SH (Figure 2), is most commonly used as a raw material in the synthesis of the organo-sulfur compound methionine, which is an essential proteinogenic amino acid used as a feed additive for livestock[15]. Typical livestock diet consisting of plant sources lack the essential amino acid methionine, which is often overcome by the use of hormones[16,17]. Hormone use is undesirable due to adverse health effects, and co-feeding methionine can drastically reduce the use of hormones in livestock agriculture. Due to the projected increase in global food demand and organic production practices, the global market for methionine is expected to increase with an annual growth rate of 4.1% between 2020-2027[2].

Methanethiol is predominantly produced by the reaction of methanol with hydrogen sulfide at 160 to 500 °C and 1 to 35 bar[18]. At typical reaction conditions, dimethyl sulfide (DMS) is produced as a byproduct through dimerization reaction, which can be separated from the reactor effluent and cleaved with hydrogen sulfide (H_2S) to recover MeSH in a secondary reactor. From a thermodynamic view, the formation of the byproduct DMS is favored for stoichiometric hydrogen sulfide-to-methanol ratios[19]. To minimize the consecutive reaction of MeSH to DMS, a large excess of hydrogen sulfide is required to limit the conversion of MeSH to DMS[20,21]. Although methanethiol selectivities up to 90% could be achieved in a two-reactor system, the process is noticeably energy-intensive, since large excess of hydrogen sulfide needs to be circulated to suppress dimethyl sulfide formation[18-20,22]. This highlights the importance of reactor optimization to improve feed conversion and overall product yield. However, this requires determination of an accurate kinetic description of the reaction system.

Kinetic parameters derived based on limited experimental measurements, as typical for most industrial cases, often fail to predict kinetic behavior outside the known operating range and thus limit optimization of reactor and process development. To circumvent this issue and to improve the overall predictive ability of the kinetic model, a statistical parameter estimation strategy is adopted, which involves cross-validation (CV) implementation to non-linear least squares. CV is commonly used to solve classification problems in machine learning for accuracy reporting, which is based on the splitting of the experimental data into a “training set” to predict

---

[2] Methionine - Global Market Trajectory & Analytics, July 2020, Global Industry Analysts, Inc.

the model, and a “validation set” to assess the quality of the model. To examine the potential benefit of this implementation towards parametric regression, a model case study is performed by comparing cross-validation least squares (LS-CV) estimation to regular non-linear least-squares (LS) approximation. As a final result of the kinetic modeling, a fully parameterized model to describe each reaction step of the methanol thiolation reaction network on a commercial catalyst is obtained and used subsequently towards modeling and optimization of reactors for a large scale methanethiol production.

Finally, the general applicability of the implemented method for derivation of robust kinetic parameters is investigated based on a simple model reaction. This case study suggests that CV implementation in the parameter estimation improves the predictive ability of the kinetic model on unknown datasets. However, the level of improvement can be expected to depend on a number of conditions, such as the number of data points, quality of measured data (noise and outliers), number of parameters, and model complexity. In this work, we evaluate the general applicability of the implemented method for derivation of robust kinetic parameters from limited and noisy data, which is typical for the industry. Water-gas shift reaction ($CO + H_2O \rightleftharpoons CO_2 + H_2$) on a common $Cu/ZnO/Al_2O_3$ catalyst with previously determined lumped kinetics is used as a model reaction[23]. Synthetic data is generated over a range of reaction temperatures, inlet feed ratios and gas hourly space velocities, representing a broad range of conversions to avoid highly localized kinetic models. By applying controlled levels of randomized noise and outliers on synthetic data, we identify the critical dataset properties in which the implemented method would yield significant improvements in terms of accuracy and computational cost over more complex optimization routines such as Markov chain Monte Carlo[24] and genetic algorithm[25].

Overall, this dissertation aims to provide both experimental and computational insights to improve our understanding of heterogeneous reaction kinetics involving C_1 chemistry.

2.0 Kinetic Investigations on the Role of Sodium Tungstate Promoter in Mn_xO_y - Na_2WO_4 Catalyzed Oxidative Methane Coupling Reaction

2.1 Introduction

The combined technological advances in horizontal drilling and hydraulic fracking enabled a steep increase in global recoverable natural gas reserves[1,2]. This abundant natural gas, consisting primarily of methane, creates a strong incentive to utilize methane beyond combustion by converting it to higher hydrocarbons, such as ethylene, as intermediates for the production of value-added chemicals and fuels. Ethylene is the most important organic chemical in the world by volume, since it is the building block for a vast array of chemicals from adhesives to solvents, paints, and plastics[4,5]. Ethylene is commercially produced via steam cracking of ethane or naphtha, a petroleum-based feedstock[3,6]. An alternative route to producing ethylene is the "oxidative coupling of methane" (OCM), in which methane is directly converted to ethane and ethylene in a single reactor at temperatures above 700°C[6-8].

OCM follows a complex reaction mechanism which involves coupled heterogeneous (catalytic) and homogeneous (non-catalytic) reaction steps[26]: In OCM, a metal oxide catalyst provides its lattice oxygen via a Mars-Van Krevelen mechanism to activate methane by breakage of the C-H bond at 700-900°C, forming methyl radicals[13,14]. After desorption of methyl radicals from the catalyst surface, the carbon-carbon coupling reaction occurs homogeneously in the gas phase[27-30]. The ethane formed in this step then homogeneously dehydrogenates to yield ethylene in a subsequent step[13]. Finally, the hydrogen formed both in the latter step and the initial dissociative methane activation step is catalytically oxidized to form H_2O, yielding a net exothermic reaction: $2\ CH_4 + O_2 \rightarrow C_2H_4 + 2\ H_2O$, $\Delta H°_R = -281.4$ kJ/mol. However, the presence of gaseous O_2 in the feed mixture – needed both to replenish the lattice oxygen in the Mars-Van Krevelen activation step and the hydrogen combustion, results in unselective side reactions where both CH_4, intermediates, and C_2 products are totally oxidized to CO and CO_2, severely limiting the overall selectivity of the reaction[12,31]. This challenge is further exacerbated by the fact that total oxidation reactions are thermodynamically favored at high reaction temperatures[32].

Since the early work of Keller and Bhasin[33], numerous investigations have focused on OCM in pursuit of suitable catalysts for economically viable reaction yields, which are estimated to be ≥30% C_2 yield[10,32,34]. However, despite these intense efforts, no such catalyst has been identified to-date and OCM remains as one of the “holy grails” in catalysis[35]. One of the best performing catalysts identified in terms of activity and C_2 selectivity are Na_2WO_4 promoted Mn-oxides (most typically supported on silica, i.e. Mn–Na_2WO_4/SiO_2), first reported by Li et al.[36,37]. This catalyst has been studied across various reactor configurations, temperatures, catalyst compositions, oxidant species, and CH_4-to-oxidant feed ratios, and typically reported to yield CH_4 conversions of 15-30% at combined C_2 selectivity between 60-80%[12,38-44]. Pure Mn/SiO_2 has been shown to be unselective since both Mn-oxide and the amorphous SiO_2 support acts as a total oxidation catalyst[45,46]. Na_2WO_4 addition to Mn/SiO_2 was found to transform amorphous SiO_2 into α-cristobalite phase, which renders the support inert[12]. Na is believed to play a role in the phase transition of amorphous SiO_2, whereas the tungstate group (WO_4) is generally claimed to be a part of the catalytically active center[28,46-48]. Based on the mechanism first reported by Li et al.[36], O_2 is activated on Mn^{+3} sites whereas (selective) CH_4 activation occurs on the W^{6+} sites. The increased selectivity upon Na_2WO_4 addition is hence due to the presence of W-O-Si sites, and oxygen spillover from Mn_2O_3 to Na_2WO_4 is responsible for the enhanced activity of the catalyst[37,49].

Transient experiments further confirm that the catalyst provides its lattice oxygen for activation and has stable redox properties[50]. CO_x formation was detected in the absence of gaseous O_2. In contrast to Li et al., Lunsford and coworkers reported that the catalytic performance was inferior without Mn[13,14]. They reported a similar catalytic performance of Mn–Na_2WO_4/SiO_2, Mn–Na_2WO_4/MgO, and $NaMnO_4$/MgO, suggesting that tungsten or tungstate centers might not be part of the active site. Accordingly, Na-O-Mn was proposed as the active site since it was common in all three identical performing catalysts. Despite the extensive research on sodium tungstate doped manganese oxide catalysts for OCM, there is a lack of consensus on the nature of the active site for methane activation and the role of Na_2WO_4, although the prevalent view in the literature remains that an oxygen spillover mechanism between the manganese and the tungstate phases is key for the OCM activity of this catalyst[16].

The present work therefore revisits the reaction kinetics and mechanism over the Mn-Na_2WO_4 catalyst system to identify methane activation and reaction pathways leading to high C_2 selectivity. Supported Mn oxide-based catalysts were synthesized, characterized, and evaluated in kinetic studies to gain insights into metal oxide phases and their correlation with activity and selectivity. In particular, the synergistic effect between MnO_2 and Na_2WO_4 is examined by physically mixing individually synthesized samples of these two metal oxides and comparing their performance to a conventional mixed oxide catalyst. From these rather straightforward syntheses, characterizations, and reactive tests, a new view of the reaction mechanism emerges that does not require any shared lattice oxygen – nor even the immediate vicinity of Mn- and WO_4-centers – and instead suggests a concerted mechanism between two disjunct catalytic sites.

Overall, this work aims to provide both experimental and computational tools and insights to improve our understanding of reaction kinetics involving C_1 chemistry.

2.2 Experimental

2.2.1 Catalyst Preparation

Conventional Mn-Na_2WO_4 mixed oxide catalyst was prepared via simple wet impregnation method using magnesium oxide as support. Manganese (II) nitrate (Sigma Aldrich, 97.0%) and sodium tungstate dehydrate (Sigma Aldrich, ACS reagent, ≥99%) were dissolved in an aqueous solvent and added to magnesium oxide (Sigma Aldrich, ≥99% trace metals basis, -325 mesh) under continuous mixing to achieve 40wt% metal loading (Mn: Na_2WO_4 ratio was kept at 1:1). The slurry was mixed at 80°C for 3 h followed by overnight drying at 100°C. Dried catalyst was ground into a fine powder using mortar and pestle. The powder was calcined under air flow at 900°C for 10 h.

For the Mn-Na_2WO_4 physical mixture catalyst, the same procedure was applied for synthesizing pure metal oxides of Na_2WO_4/MgO and MnO_2/MgO, separately. After calcination, aliquots of supported MnO_2 and Na_2WO_4 catalysts are carefully mixed in a vial to prepare the physical mixture catalyst. The total weight loading and the Mn: Na_2WO_4 ratio of the physical mixture were kept identical to the mixed oxide. For clarity, we will refer to this catalyst as "physical mixture catalyst", PMC, in contrast to the "mixed oxide catalyst" Mn-Na_2WO_4/MgO, MOC).

2.2.2 Catalyst Characterization

Surface area. The specific surface area was determined via nitrogen sorption in a Micromeritics ASAP 2020 gas adsorption analyzer using the BET method at 77 K. Prior to the measurement, the samples were degassed for 2 h at 200°C under high vacuum. Low surface areas (<4 m^2/g) were observed for all materials tested due to high temperature treatment.

X-ray diffraction (XRD) characterization. The measurements were performed with a powder X-ray diffractometer (Bruker D8) in line focus mode employing Cu K radiation (k = 1.5418 Å) with typical 2h scans between 15° and 90°. The catalysts were characterized at different stages of the experiments, i.e. after synthesis and fixed-bed reactor tests. Crystal phases were identified based on the JCPDS database.

Electron microscopy. A JEOL JEM-2100F high-resolution transmission electron microscope (HR-TEM) was used to obtain images of the samples to evaluate the size and uniformity of the particles (Appendix Figure 1).

2.2.3 Reactive Testing

Thermogravimetric analysis (TGA). Thermal stability and the oxidation state of the catalysts were evaluated in a thermogravimetric analyzer (TA Instruments STD Q600). The catalyst (7-15mg) in an alumina pan was placed in the TGA cradle and heated under Argon flow (grade 5.0, 20sccm) to 900°C at 100°C/min ramp rate and kept isothermal throughout the experiment. CH_4 (grade 2.0, 10sccm) or H_2 (grade 2.0, 20sccm) was flown over the heated sample to simulate the fixed bed reaction until all lattice oxygen was consumed, monitored by the total weight loss. The reduced samples were oxidized with air in a consecutive step. The TGA cradle was purged with Argon in between reducing and oxidizing gas flow. N_2 (grade 5.0, 20sccm) was used as the carrier gas during all TGA runs. Weight loss between oxidized and reduced samples at reaction temperature was used to calculate the oxide phases associated with each state. The stability of the catalysts as reflected in repeatable redox cycles with identical maximum and minimum weights (i.e. identical oxidation states) was also studied over the runs with extended cycles.

Fixed bed experiments. Reactive test experiments are performed in a fixed bed reactor to evaluate the feed conversion and product selectivity. 50 mg of synthesized catalysts were packed inside the quartz-glass tubular reactor (1/4" ID), which was horizontally inserted into an electric oven (Thermo Electron Corporation – Lindberg/Blue M) set to 900°C. Quartz wool was placed on both sides of the catalyst bed for support. Reducing gases (CH_4, C_2H_6 and C_2H_4) and O_2 were flown to the reactor periodically at 3650 h^{-1} GHSV. All gases used in this study are high purity (>99.5%). The catalyst bed was purged with He between oxidation and reduction to avoid hydrocarbon – molecular oxygen mixtures and assure well-defined gas phase compositions. An ice-trap was placed at the reactor exit to condensate moisture before monitoring the effluent gases continuously using a mass spectrometer (Pfeiffer Omnistar QMS 200) and Micro GC 300 (Agilent). Product compositions were calculated by converting ion current signals from mass spectrometry to molar flowrates (n_i) using calibration factors of each gas species. The accuracy of data collection was assessed via a carbon balance, which closed to better than ±3.5% error for all experiments reported. CH_4 conversion, product selectivity, and yield were calculated using the equations shown below. Calculated selectivity and yield values of ethylene and ethane are cumulated and are denoted as C_2 throughout the manuscript.

$$\text{Methane conversion [\%]},\ X_{CH4}=\frac{\text{moles of CH}_4\text{ converted}}{\text{moles of CH}_4\text{ in feed}}\text{x}100 \tag{2-1}$$

$$\text{Product selectivity, species } i \text{ [\%]},\ S_i=\frac{\text{moles of species } i \text{ formed}}{\text{moles of total products}}\text{x}100 \tag{2-2}$$

$$\text{Product yield, species } i \text{ [\%]},\ Y_i = X_{CH4} * S_i \tag{2-3}$$

2.3 Results and Discussion

2.3.1 Evaluation of Catalytic Performance

As a baseline comparison, single component MnO_2/MgO and Na_2WO_4/MgO catalysts were studied individually via thermogravimetric and fixed-bed reactor studies prior to evaluating the catalytic performance of the Mn-Na_2WO_4/MgO MOC.

The reducibility of the metal oxides was initially evaluated by TGA at 900°C starting with fully oxidized catalysts. Figure 3A and Figure 3B show the weight change during oxidation and reduction steps for MnO_2/MgO and Na_2WO_4/MgO, respectively. Reduction by CH_4 is accompanied by weight loss whereas oxidation results in weight increase. A simple mass balance calculation enables the calculation of the maximum and minimum weight of the MnO_2/MgO catalyst with fully oxidized MnO_2 (i.e. Mn^{4+}) and reduced MnO (Mn^{2+}) oxidation states, respectively.

A close agreement between calculated and measured sample weights is observed, confirming conversion between these two oxidation states. After the reduction of the catalyst to MnO, a small weight increase was observed due to the thermal cracking of CH_4, which results in coke deposition.

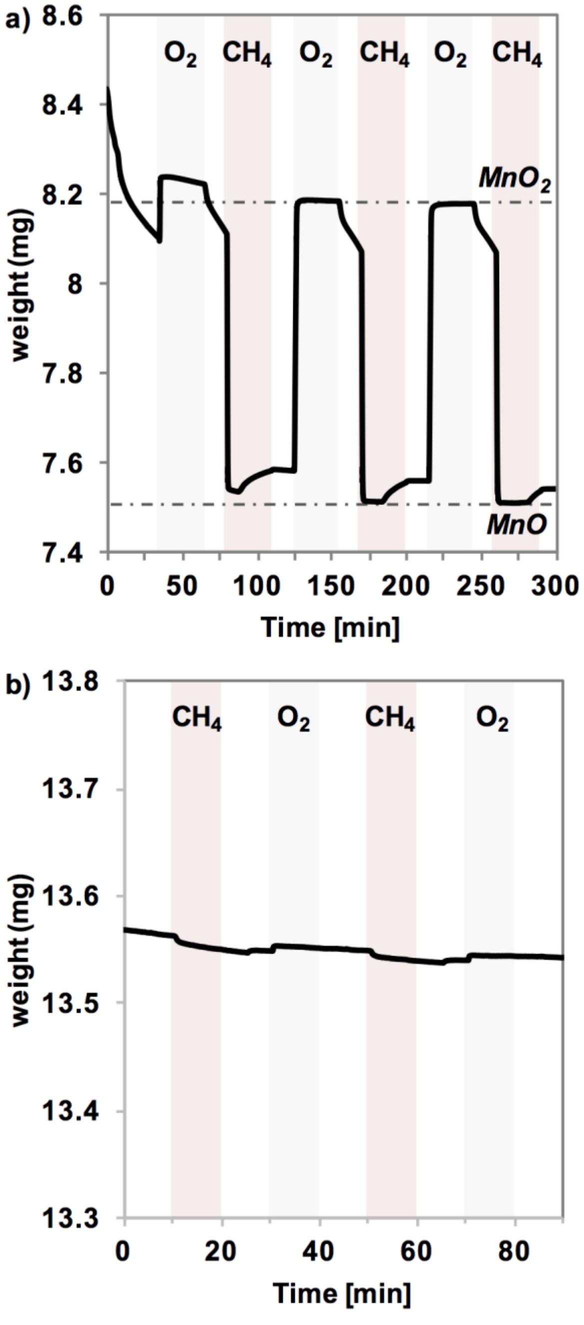

Figure 3 Thermogravimetric analysis of MnO_2/MgO a) and Na_2WO_4/MgO MOC b) at temperature=900°C. The oxidation and reduction cycles (grey shaded areas) were carried out consecutively with He purge in between.

Similarly, during the purge phase between the oxidation and reduction steps, a weight loss was observed for the fully oxidized MnO_2 sample (Figure 3A). This is due to the thermal decomposition of MnO_2 at high temperatures, which results in oxygen loss to the gas phase and consequent weight loss[51,52]. The rate of oxygen loss during the purge phase is quantified in separate TGA experiments and taken into consideration for material balances (Appendix Figure 2). In order to minimize the impact of this oxygen loss, the purge period was kept at exactly 10 minutes in all experiments. On the other hand, TGA experiments did not show any weight change of Na_2WO_4/MgO under CH_4 or oxygen flow (Figure 3B), indicating that this carrier shows no reactivity with methane and hence no lattice oxygen loss.

After establishing this baseline activity, the catalytic performances of Mn-Na_2WO_4/MgO MOC, MnO_2/MgO, and Na_2WO_4/MgO were evaluated in a fixed bed reactor at 900°C by flowing CH_4 (20vol% in He, total flowrate: 13.5 sccm) over a 50 mg pre-oxidized catalyst. After pre-oxidation at the reaction temperature, the catalyst bed was purged with He and CH_4 was continuously fed into the reactor until no C_2 signal was detected in the mass spectrometry. Since the reaction is performed at transient conditions, product formation rates and product distribution change continuously as the lattice oxygen is being consumed throughout the reaction progress. This mode of evaluation was chosen in order to avoid masking the true catalytic reaction rate by accompanying homogeneous oxidation steps in the presence of gaseous oxygen in the feed.

While unpromoted MnO_2/MgO shows significant coupling activity (Figure 4A), the lattice oxygen is quickly consumed due to the predominant formation of CO_2 (note that CO_2 and H_2O are shown on the secondary y-axis, i.e. their respective concentrations are more than an order of magnitude larger than those of the other products). MnO_2/MgO hence is not selective towards C_2 products despite the absence of gas phase O_2 (Figure 4D), which indicates that CO_x formation is easily initiated in contact with the surface oxygen. The source of CO_2 could either be direct deep oxidation of surface bound CH_3 (i.e. before desorption) or subsequent re-adsorption and oxidation of C_2 products, since these are known to be more reactive than CH_4 at reaction conditions[32]. After reduction of the oxide to MnO (i.e. after t ≈ 2 min), the onset of strong H_2 formation indicates coking of the catalyst due to methane cracking.

Addition of Na_2WO_4 to this catalyst to form a Mn-Na_2WO_4/MgO MOC catalyst results in a reduction of cumulative CO_2 production by ~30% and a >10-fold increase in C_2H_4 formation despite identical amounts of manganese oxide used in these experiments (Figure 4B). As a result, a strong increase in C_2 selectivity is observed (Figure 4E). The product spectrum for the Mn-Na_2WO_4 MOC (Figure 4B) shows furthermore that the highest C_2 concentrations occur at the onset of the reduction during the phase transition from Mn^{+4} transition to Mn_2O_3 (Figure 4E), with a maximum C_2 yield of 13% (19% conversion and 69% selectivity). The rapid onset of hydrogen formation at t ≈ 13.5 min again indicates methane cracking due to the reduction of the catalyst to (essentially non-reducible) MnO. Due to the much-improved selectivity of the reaction, which results in a much lower oxygen consumption per mole of methane, this point is much delayed in comparison to the pure Mn-MgO catalyst (from t ≈ 2 min to ~13.5 min).

Fixed bed experiments with pure Na_2WO_4/MgO did not yield any C_2 products nor any significant CH_4 consumption, consistent with the TGA results (Figure 3B) and hence are not shown here.

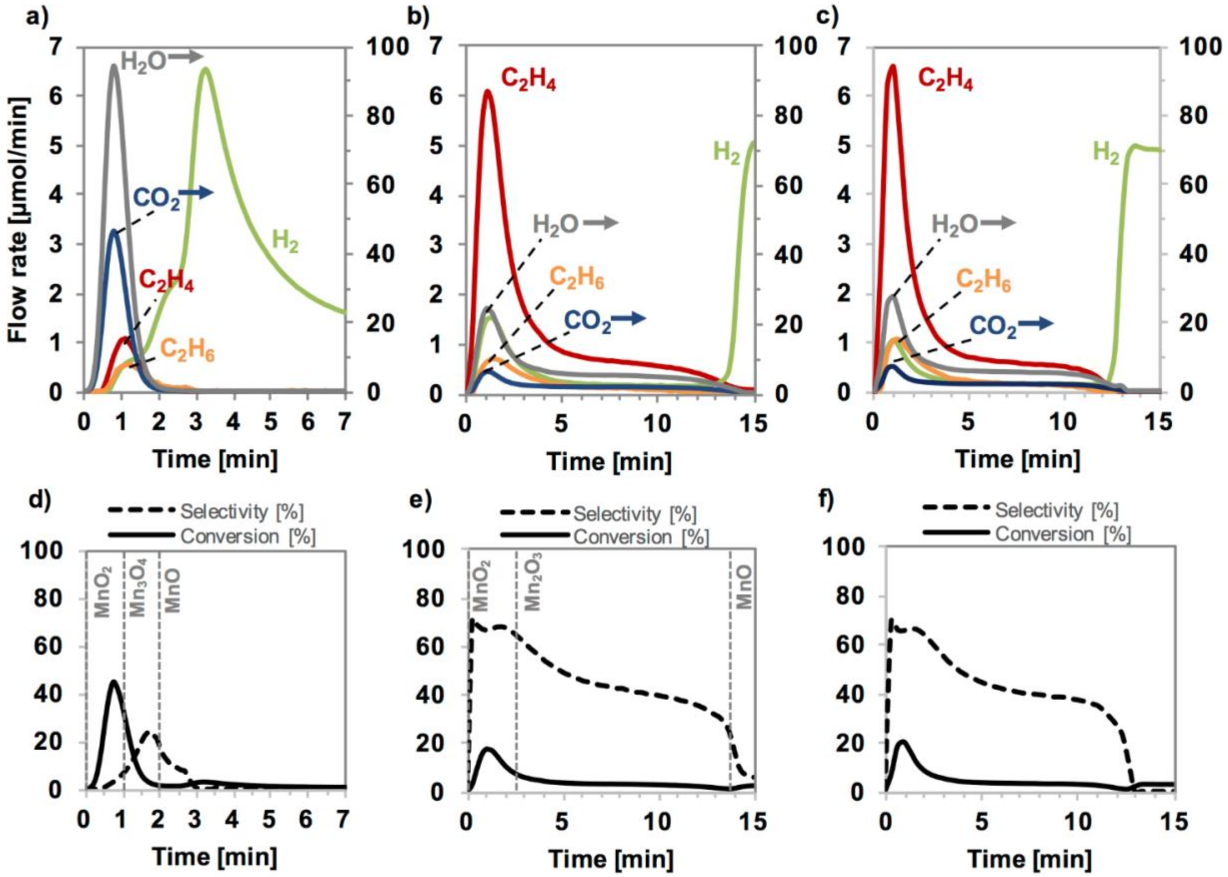

Figure 4 Product spectrum of a) of MnO_2/MgO b) Mn-Na_2WO_4/MgO MOC and c) Mn-Na_2WO_4/MgO PMC, temperature=900°C, GHSV=3650h-1. CH_4 (20% concentration in He, total flowrate:13.5 sccm) was flown over a 50 mg pre-oxidized catalyst. Products of total oxidation reaction, CO_2 and H_2O are shown on the secondary y-axis in panels a-b. Respective selectivity and conversion are shown in d-f.

Overall, the catalytic performances of the individual metal oxides hence were found to be much inferior to the Mn-Na_2WO_4 MOC. The results suggest that the Mn phase is required for methane activation and the addition of Na_2WO_4 renders the catalyst selective for C_2H_4 formation.

Although similar synergistic effects between manganese oxide and sodium tungstate have been reported previously, the reaction mechanism for OCM is very complex and significant disagreement exists over the nature of the active site. The majority of the mechanistic studies on

OCM has been performed with inert SiO_2 support due to its known stability over extended periods[12]. However, the mechanistic discussion of these studies is relevant and significant for MgO supported catalysts as well since MgO also constitutes as an inert support for OCM under the reaction conditions (as also confirmed here by the absence of any noticeable activity for Na_2WO_4/MgO).

In agreement with our results, Mn/SiO_2 was previously reported as an unselective OCM catalyst. However, the poor C_2 selectivity was attributed to the amorphous SiO_2 phase, which acts as a total oxidation catalyst[45,46]. Differentiation between the contributions of MnO_2 and SiO_2 was not possible in those studies. Na_2WO_4 addition to Mn/SiO_2 was found to transform amorphous SiO_2 into the α-cristobalite phase, which is inert[12]. Na was believed to essential for phase transition of SiO_2, whereas -WO_4 is generally claimed to be a part of the active center[28]. A widely accepted mechanism based on an oxygen spillover between metals for methane activation was proposed by Li et al. [49] and supported with studies from other research groups[12,36,37]. According to this mechanism, methane activation takes place on the W^{6+} sites, while activation of gas-phase oxygen occurs on the Mn^{3+} sites. The oxygen spillover from Mn_2O_3 to Na_2WO_4 then enhances the catalytic activity and C_2 selectivity of oxidative coupling of methane to ethylene[49]. The increased selectivity is attributed to the W=O and W-O-Si centers that are more selective towards methyl radical formation. This reaction mechanism seems to be inconsistent with our results since no CH_4 activation is observed over Na_2WO_4 without the presence of Mn.

In contrast to Li et al.[49], Lunsford and coworkers[13,14] tested Mn/Na_2WO_4/MgO, Mn/Na_2WO_4/SiO_2, and $NaMnO_4$/MgO catalysts for OCM in co-feed and pulse reactor studies. Due to the similar catalytic performances of these catalysts, the authors suggested that W might not be necessary, and Na-O-Mn is the most likely active site. In line with our findings, Mn was claimed to be the active center for methane activation center since its absence generally resulted in poor CH_4 conversion. Very similar selectivity and activity were reported for MgO and SiO_2 supported Mn-Na_2WO_4 catalysts, supporting our claim that the reaction mechanism is similar across different (inert) supports. In a follow-up study, though, the MgO supported catalyst was found to gradually deactivate in co-feed mode whereas the SiO_2 supported catalyst was stable up to 97 hours on stream[53].

To further test the previously claimed synergistic effect between MnO_2 and Na_2WO_4 via a spillover mechanism, we used Mn-Na_2WO_4/MgO PMC (which was prepared by mixing aliquots of separately prepared MnO_2/MgO and Na_2WO_4/MgO powders). The Na_2WO_4: Mn ratio and total catalyst weight loadings in the PMC were kept identical to the MOC for direct comparison. Clearly, a spillover mechanism requires that the performance of this PMC will perform essentially identical to the pure MnO_2/MgO catalyst (since the Na_2WO_4/MgO catalyst is completely inactive). The negligible interface between these oxides (limited to the negligible contact area between random adjacent catalyst particles) renders any spillover highly unlikely and very inefficient, i.e. the physical mixture allows neither molecular nor electron transfer between the two metal oxides. However, remarkably, we find that catalytic performance and product spectrum of the PMC (Figure 4F) and the MOC (Figure 4C) are essentially indistinguishable. This suggests that the prevalent mechanism for synergy between the two catalyst phases may be incomplete. Instead, the synergy between the two catalysts most likely result from gas-phase mediated interactions. Since our results above have shown that methane can only be activated on the surface of MnO_x, this suggests that interactions must be based on secondary reactions of primary reaction products formed on MnO_x with the added Na_2WO_4 catalyst.

2.3.2 Activation Mechanism and the Role of Na_2WO_4.

Based on the observations and discussion above, we hence propose a new pathway for the synergistic improvement between MnO_2 and Na_2WO_4 catalysts, which couples the two catalysts solely through gas phase interactions. The proposed mechanism is shown schematically in Figure 5, comparing the reaction mechanism over MnO_2 (Figure 5A) with that over Mn-Na_2WO_4 (Figure 5B), respectively.

On manganese oxide, methyl radicals are generated on the catalyst surface. These radicals desorb into the gas phase and "couple" to form C_2H_6, which then dehydrogenates to C_2H_4 in a non-catalytic gas phase reaction. However, due to the high reactivity of MnO_x, both products then get oxidized further to CO_x, resulting in only low C_2H_4 yields at the reactor exit (Figure 5A).

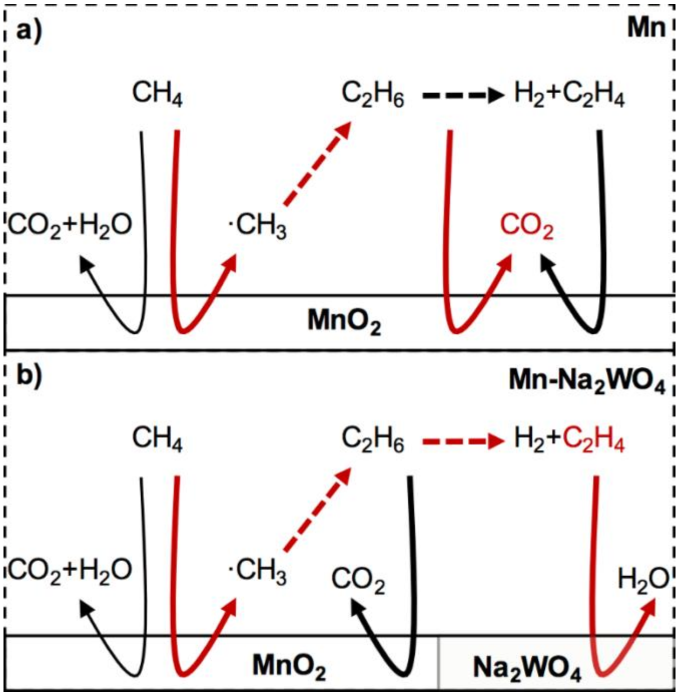

Figure 5 Proposed reaction mechanism on a) Manganese oxide b) Manganese-tungsten mixed oxide. Solid arrows represent surface reactions whereas dashed arrows indicate homogeneous gas phase reactions.

If we further hypothesize that Na_2WO_4 shows little to no activity for methane activation but can readily react with H_2 then, upon Na_2WO_4 addition, H_2 generated from homogeneous C_2H_6 dehydrogenation in the gas phase is oxidized in contact with tungstate lattice oxygen (Figure 5B). This selective H_2 removal pulls the ethane dehydrogenation reaction to the product side and hence decreases the rate of the competing parallel total oxidation of ethane on the manganese oxide surface.

Since manganese and tungsten oxides catalyze separate, independent reaction steps explain the fact that physical mixtures of monometallic oxides perform identically to a mixed oxide (Mn-Na_2WO_4) catalyst. This mechanism is also consistent with the observation that Na_2WO_4 is inactive towards OCM since it requires MnO_x to activate methane, i.e. form methyl radicals and hence enable the gas phase dehydrogenation reaction. In fact, Na_2WO_4/SiO_2 has been reported before to be a selective ODH catalyst[39,54].

However, the proposed mechanism is based on two key assumptions, which require validation: (1) According to the mechanism, C_2H_6 must show the fastest oxidation kinetics on Mn-based catalysts, so that the acceleration of the dehydrogenation (via removal of the H_2) and hence enhanced ethylene formation indeed “shelters” the C_2 products from rapid deep oxidation; and (2) tungstate lattice oxygen must selectively remove H_2, i.e., it must show negligible reactivity towards all hydrocarbons in the system. In the following, we will validate these assumptions.

2.3.3 Validation of Hypothesis

A key observation upon tungstate addition to the reaction system is the strong reduction in CO_2 formation. While one could speculate in the case of a mixed oxide catalyst that the addition of the second phase moderates the oxidation activity of the first phase and hence reduces its tendency towards total oxidation, this is clearly not a possible explanation for a purely physical mixture due to the complete absence of any direct interactions, i.e. electronic or structural modification of the catalyst phases. Hence, if the addition of the tungstate removes hydrogen and hence results in an enhanced dehydrogenation rate, as proposed here, this increased ethylene formation will only result in reduced CO_x formation if ethylene shows lower reactivity with MnO_x than ethane.

We hence tested the relative reactivity of methane, ethane, and ethylene over MnO_2/MgO catalysts in separate fixed bed experiments by flowing CH_4, C_2H_4, and C_2H_6, respectively, over a pre-oxidized MnO_2/MgO catalyst at 900°C. CO_2 formation rates for all three hydrocarbons were determined and are shown in Figure 6. The results confirm that C_2H_6 shows indeed the highest CO_2 formation rate among these hydrocarbons, with a maximum reduction rate that is ~1.5 times faster than that of C_2H_4 and ~3 times faster than that of CH_4. Similar experiments with a pure Na_2WO_4/MgO catalyst under identical experimental conditions furthermore confirmed that this catalyst indeed shows negligible reactivity with all three hydrocarbons, further supporting our mechanistic hypothesis (see inset in Figure 6). Peak reaction rates are reduced by more than an order of magnitude compared to MnO_2, and only 2% of the available lattice oxygen in the tungstate is consumed with C_2H_4 and less than 0.5% for C_2H_6 and CH_4 over the course of ~10 minutes required for total oxygen consumption by hydrogen.

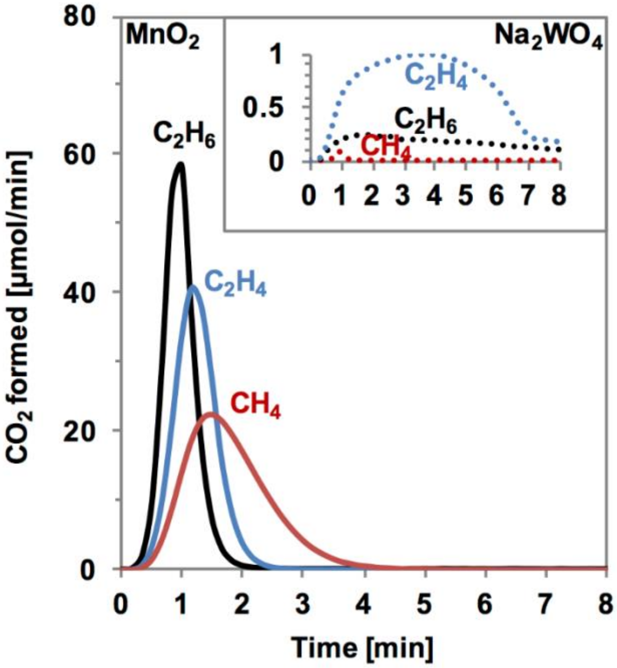

Figure 6 CO_x formation rate from CH_4, C_2H_4, and C_2H_6 on MnO_2/MgO and Na_2WO_4/MgO (inset). CH_4 (10vol% in He, total flowrate:13.5 sccm) was flown over a 50 mg pre-oxidized catalyst at T=900°C.

We furthermore carefully tested the possibility that a partial reduction of the tungstate by hydrogen could alter the activity of this phase. We quantified the oxygen loss via elemental balance and post-run characterization. For this purpose, total oxygen consumption was calculated based on the amount of CO_2 and H_2O formed during the reaction on the Mn-Na_2WO_4 catalyst (no other oxygenates were detectable at experimental conditions). Based on the initial oxygen content of the catalyst and the calculated cumulative oxygen consumption throughout the reduction of the catalyst, tungsten oxide is calculated to account for ~20wt% of total mass loss (Appendix Figure 3, which corresponds to a partial reduction of Na_2WO_4 from +6 to ~ +4. The oxygen loss is further confirmed by post-reaction analysis via XRD on the used sample, which shows the reduction of MnO_2 to MnO and reduction of tungstate to tungsten bronze during the reaction (Figure 7).

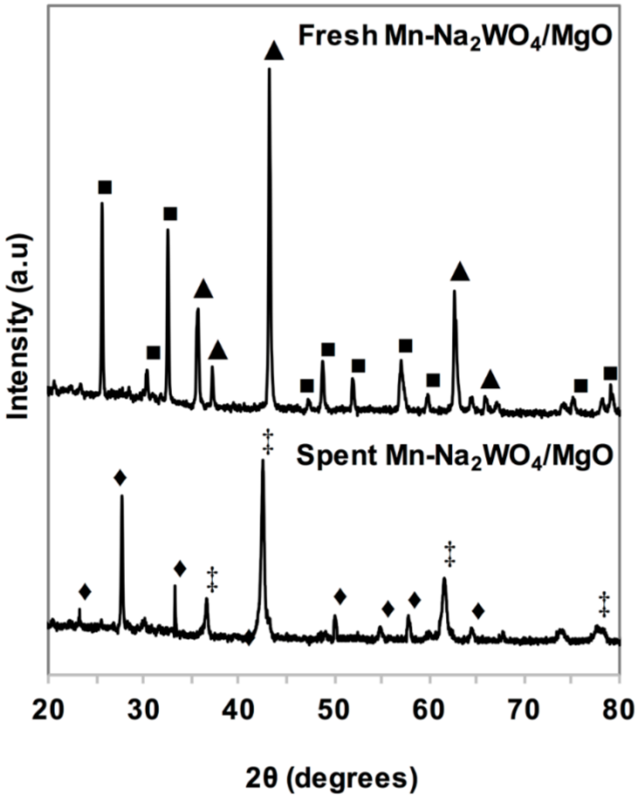

Figure 7 XRD data obtained from fresh and spent Mn-Na_2WO_4/MgO MOC under CH_4 flow over the pre-oxidized catalyst at 900°C. The labels indicate the following crystal phases: ▲, MnO_2; ■, Na_2WO_4; ‡, MnO; ♦, $NaWO_3$.

The observed partial reduction of the tungstate by hydrogen opens the possibility that, unlike the fully oxidized phase, this partially reduced phase could show reactivity with methane and hence open a new reaction pathway. To exclude this possibility, another set of experiments was performed by exposing a pure tungstate catalyst to a hydrogen/methane mixture with various H_2:CH_4 ratios. Figure 8 shows the results, confirming only minimal methane conversion at all three conditions. No coupling activity was observed in any case, confirming that hydrogen removal on tungstate is selective throughout the reaction. Overall, these tests hence support our proposed mechanism.

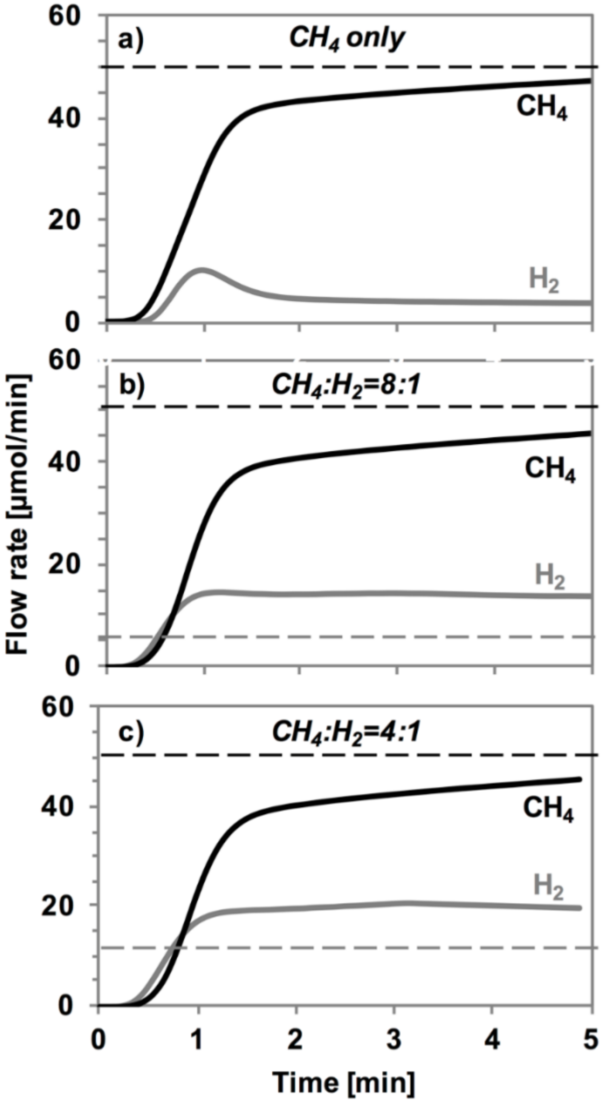

Figure 8 Product spectrums of a) pure CH_4 b) 8:1 CH_4 to H_2 ratio c) 4:1 CH_4 to H_2 ratio on Na_2WO_4/MgO, temperature=900°C, CH_4 (10% concentration in He, total flowrate: 13.5 sccm) was flown over a 50 mg pre-oxidized catalyst. Dashed lines represent the reference feed flowrate for each gas.

2.3.4 Mn-phase Activity-Selectivity Relationship and Optimal Na_2WO_4:Mn Ratio

The transient reactive tests so far enabled us to identify phase changes and the catalytic activity associated with the tungstate phase. To further identify the role of the various Mn oxide phases, we further investigated the relative rates of CO_2 vs C_2H_4 formation over unpromoted MnO_2/MgO and the mixed Mn-Na_2WO_4/MgO catalysts.

On the pure MnO_2/MgO catalysts, maximum CO_2 formation occurs in the presence of partially reduced Mn oxide (~Mn^{3+}), while C_2H_4 formation occurs (at much lower rates) with a significant delay during the transition from Mn_3O_4 to MnO (Figure 9A main figure and inset, solid lines). In contrast, in the presence of Na_2WO_4, the maxima for both CO_2 and C_2 formation are shifted strongly towards higher Mn-oxide phases, i.e. towards Mn^{4+} (Figure 9B main figure and inset, solid lines). Most significantly, both the total oxidation product and the coupling product occur at identical times ($t \approx 1$ min), i.e. over the same Mn oxidation states. This suggests that the intrinsic activity for C_2 and CO_2 formation may be directly coupled, i.e. CO_2 formation may occur via a rapid, sequential pathway from C_2. For both catalysts (pure MnO_2/MgO and the mixed oxide), methane activation occurs solely on the Mn oxide phase, resulting in the formation of methyl radicals which desorb into the gas phase and couple to C_2H_6. C_2H_6 can subsequently either (homogeneously) dehydrogenate to C_2H_4 or (catalytically) oxidize to CO_2 (see also Figure 5). Over pure MnO_2/MgO, the high reactivity of ethane results in rapid oxidation to CO_2 and hence rapid reduction of the Mn oxide phase. The concomitant slowing of the oxidation reaction eventually reduces the rates sufficiently to allow a small fraction of C_2H_4 to survive (while essentially all C_2H_6 is being oxidized due to the higher reactivity). Upon addition of the tungstate phase, the removal of hydrogen from the dehydrogenation reaction via catalytic oxidation of H_2 with WO_4

enhances C_2H_4 formation. Since C_2H_4 has significantly lower reactivity with Mn oxide (see Figure 6), this results simultaneously in an increase in C_2H_4 selectivity and much reduced CO_2 formation.

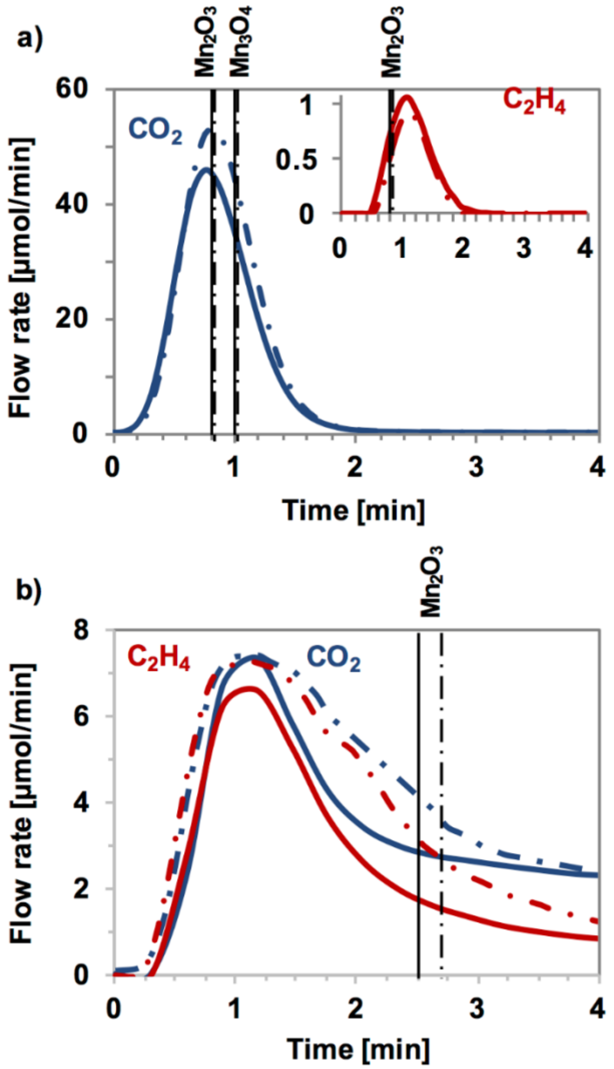

Figure 9 CO_2 and C_2H_4 spectra of a) MnO_2/MgO and b) Mn-Na_2WO_4/MgO MOC. GHSV=3650h^{-1}, temperature=900°C, CH_4 (20% concentration in He, total flowrate: 13.5 sccm) was flown over a 50 mg pre-oxidized catalyst. Solid curves represent 10 min purge whereas dotted curves represent 4 min purge.

The impact of the Mn oxidation state was further studied by altering the initial Mn oxidation state by manipulating the purge period. It is well established that Mn oxide loses ("uncouples") lattice oxygen at temperatures above 500°C[55,56], which allows the use of various purge durations to adjust the initial oxidation state. The typical purge period of 10 minutes (used to avoid the formation of potentially explosive mixtures between methane and air) was hence lowered to 4 minutes to increase the available amount of lattice oxygen (i.e. increase the initial oxidation state of Mn). The results are shown in the dotted lines in Figure 9. One can see that for the pure manganese oxide catalyst the increase in oxidation state results in a small increase in maximum CO_2 formation and decrease in C_2H_4 formation, while for the mixed oxide a significant increase in cumulative C_2H_4 production (by ~20% over the 4 min duration of the experimental window) was observed (Figure 9B). This further confirms that the reactivity of the sample, but not the selectivity of the reaction, is directly correlated with the oxidation state of the Mn content.

Finally, if the presence of Na_2WO_4 affects the selectivity of the reaction via the removal of hydrogen, the relative amount of tungstate to Mn oxide in the catalyst bed is expected to affect the selectivity. Broadly, one should expect that selectivity will initially increase proportionally with increasing tungstate content (since hydrogen removal will be proportional to the available tungstate surface area), and then saturate once the rate of hydrogen removal balances the rate of the dehydrogenation reaction (i.e. hydrogen production).

This hypothesis was tested by changing the ratio of Na_2WO_4-Mn in a physical mixture, keeping the amount of MnO_2/MgO (and hence the activation of methane) fixed while increasing the Na_2WO_4 content. The Na_2WO_4:Mn mass ratio was varied via physically mixing the respective oxides at ratios of 1:6, 1:4, 1:2, 1:1 (default), and 2:1. (Note that the mass ratio is based on metallic Mn, so that a ratio of 1.0 corresponds to a Na_2WO_4:MnO_2 mass ratio of 0.63. Furthermore, BET surface areas of both catalysts are similar with 3.0 and 3.4 m^2/g for Na_2WO_4/MgO and MnO_2/MgO, respectively). Figure 10 shows the results in terms of methane conversion (diamonds) and C_2 selectivity (squares) vs Na_2WO_4: Mn ratio taken at maximum methane conversion.

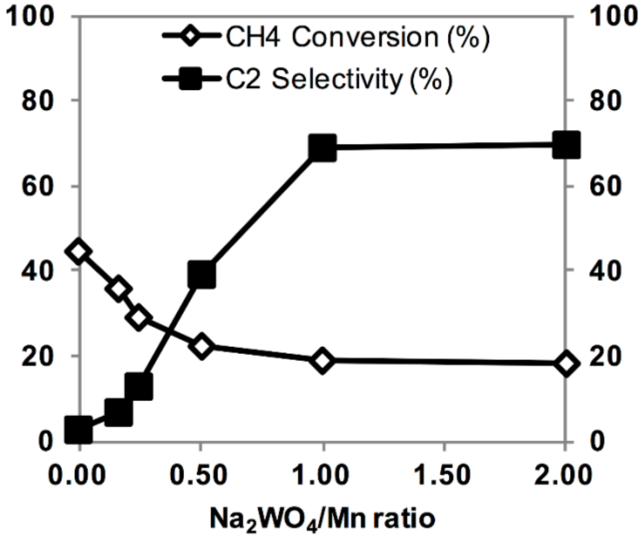

Figure 10 Conversion and selectivity at maximum CH_4 conversion while varying the Na_2WO_4 to Mn mass ratio in PMC. Fixed bed experiments are performed at 900°C, GHSV=3650h-1, CH_4 (20% concentration in He, total flowrate: 13.5 sccm) was flown over pre-oxidized catalysts.

One can see that the maximum instantaneous methane conversion (i.e. highest methane conversion at any moment in time during reduction) decreases with increasing Na_2WO_4 to Mn ratio due to suppression of rapid CO_2 formation at the onset of the reaction. In parallel, C_2 selectivity increases from 2.5% to 69%. As predicted, the initial increase is near-linear with increasing tungstate content (the small initial deviation from linearity is likely due to the concomitant change in conversion), and then saturates at high tungstate content (above 1.0). This suggests that at Na_2WO_4 to Mn mass ratio of 1:1, H_2 removal on Na_2WO_4 balances H_2 formation via homogeneous dehydrogenation of C_2H_6 at the reaction conditions and thus adds further support to the suggestion that tungstate indeed acts as a co-catalyst for hydrogen removal.

2.4 Conclusion

Oxidative coupling of methane remains one of the most promising – and one of the most elusive – pathways for methane upgrading to value-added chemicals. The present work revisits OCM on Mn-Na_2WO_4/MgO – one of the most effective catalysts for this reaction to-date – to gain further insights into the role of the two metal oxide phases in this catalyst system. A series of comparative fixed bed reactive tests, thermogravimetric analyses, and materials characterizations were conducted on both mixed oxide and single metal oxide catalysts in order to elucidate methane activation and the role of Na_2WO_4. Experiments were conducted in the absence of molecular oxygen in the reactor feed which enabled us to focus on surface-initiated reactions and observe reaction pathways that are not readily visible otherwise.

In agreement with prior studies, both individual metal oxides show poor OCM performance at 900°C: Na_2WO_4 is completely inactive towards methane activation, while manganese oxides favor unselective total oxidation followed by rapid deactivation via coking. The combination of the two oxides in a mixed Mn-Na_2WO_4 catalyst decreases the cumulative CO_2 production by 30% and yields a 10-fold increase in C_2 production, resulting in a steep increase in C_2 selectivity to 69% at 900°C. In order to test the widely accepted attribution of this synergistic effect of Mn and Na_2WO_4 to oxygen spillover between the metal centers, separately prepared aliquots of single-metal oxides were carefully mixed, and the catalytic performance of this simple physical mixture was evaluated and compared to that of the (chemically) mixed oxide. Remarkably, identical performance in terms of both activity and selectivity was obtained.

Further analysis and experimental verification lead us to propose a new mechanism for this catalyst, which is based on a concerted reaction over two independent catalysts (the MnO_2 and the Na_2WO_4 based catalysts), mediated through the gas phase: MnO_2 is responsible for CH_4 activation and desorption of methyl radicals into the gas phase, where they combine to form C_2H_6 and then dehydrogenate to C_2H_4. In the absence of a co-catalyst, the high, but unselective activity of the manganese oxide catalyst then results in rapid oxidation of these primary C_2 products to CO_2 and hence very low coupling selectivity. In the presence of a Na_2WO_4 catalyst, which we showed to be highly active for H_2 oxidation but essentially inactive for any hydrocarbon conversion, H_2 is rapidly oxidized, promoting the dehydrogenation of C_2H_6 to (much less reactive) C_2H_4 and thus resulting in strongly reduced CO_2 and enhanced C_2H_4 formation. The proposed mechanism relies on the coordination of two essentially independent catalysts, one for the generation of CH_3 radicals and the other for reactive H_2 removal, and thus suggests that novel, more effective catalysts could be found by searching for catalyst systems that are optimized for these two reaction steps – a much simpler and more well-defined task than the elusive search for a catalyst that promotes the highly complex OCM reaction.

However, in recent years, an in-situ characterization study of the catalyst surface revealed that sodium salt is molten at the typical OCM reaction temperatures (>800°C)[57,58]. In an attempt to capture the change in Na_2WO_4 crystal structure, in situ XRD was performed by Takanabe et al.[58] at high temperatures under air flow. XRD patterns of Na_2WO_4/TiO_2 at 500-800°C revealed that XRD peaks associated with Na_2WO_4 at room temperature disappear above 700°C (no clear signal), suggesting the formation of a molten state. The original phase recovers with a cool down to room temperature, which is consistent with our ex-situ XRD measurements on the spent sample that shows clear sodium tungsten peaks (Figure 7). This new evidence brings out the possibility that Na_2WO_4, due to its high mobility in the molten state at the reaction temperature, can wet adjacent Mn oxide particles, removing or reducing the “physical separation” introduced into the system, and hence allow oxygen or cation exchange to proceed easily. In addition, the liquid phase can block the surface of MnO_2 particles, possibly hindering interactions with gaseous species and partially inhibiting complete oxidation reactions[59]. However, no study to-date explored the direct effect of surface wetting and increased mobility on metal oxide interactions. Therefore, to investigate the physical behavior of the catalyst at high temperatures, a series of in-situ environmental TEM (E-TEM) experiments with elemental mapping on physical mixture catalyst is planned as a follow-up study. Details of the suggested experiments are provided in Section 5.1.1 of this thesis. Proposed in situ characterizations, along with the kinetic experiments presented and discussed here, would enable us to gain an even deeper understanding of the synergistic interaction between Na_2WO_4 and MnO_x at reaction conditions.

3.0 Kinetic Modeling, Reactor Design and Optimization of Catalytic Reaction Systems: Application to Methanethiol Production

3.1 Introduction

Similar to ethylene, another value-added chemical that can be synthesized through methane upgrading is methyl mercaptan or methanethiol, which is an aliphatic thiol with the formula CH_3SH. Methanethiol is a chemical feedstock for the production of agricultural products, plastics, jet fuel, and more prominently for the synthesis of methionine[60-62].

Methionine is an essential proteinogenic amino acid, which is mainly used as a feed additive in livestock production, predominantly poultry[63]. Food and Agriculture Organization of the United Nations predict that poultry is expected to have the largest growth and share of global meat demand by 2050[64] (Figure 11). It has been reported that their typical diet consisting of plant sources lack essential amino acid methionine, which is critical for their metabolic activity and egg laying[61]. Typically, the complications of methionine deficiency are overcome by hormone use[16,17], which may result in other adverse health effects. Therefore, feeding synthetic methionine to livestock is a more sustainable approach, and the National Organic Program (NOP) permits certain levels of synthetic methionine to be used in organic production[65]. Due to the projected increase in global food demand and organic production practices, the global market for methionine, which is estimated at US$3.6 Billion in the year 2020, is expected to reach a size of US$4.8 Billion by 2027, with an annual growth rate of 4.1% between 2020-2027[3].

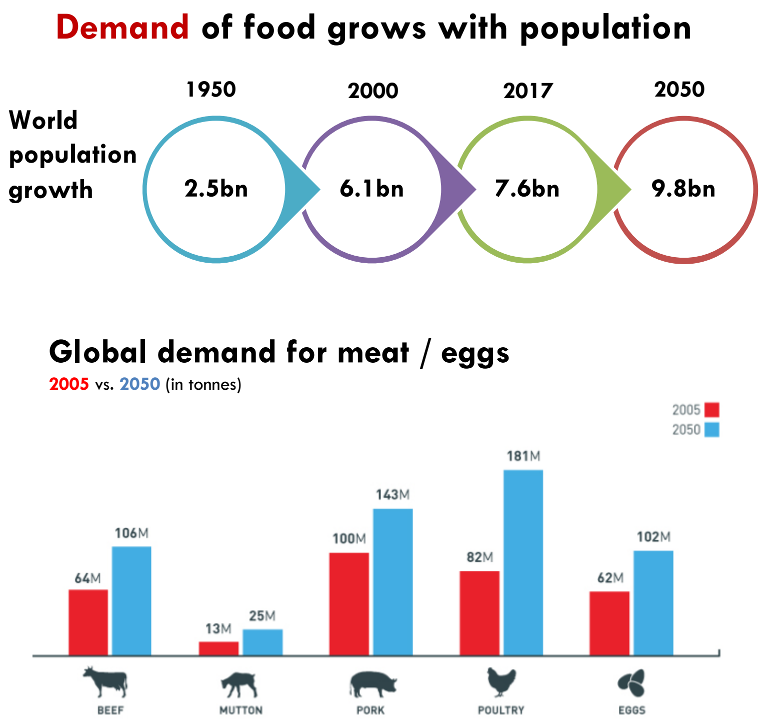

Figure 11 Population and global meat demand growth by 2050[64,66]

The catalytic methanethiol formation is first reported in 1910 by Sabatier[22], who observed the formation of thiols when passing alcohols and H_2S over thorium dioxide at elevated temperatures. Today, on an industrial scale, methanethiol (methyl mercaptan, MeSH) can be produced through the reaction of methanol (MeOH) with hydrogen sulfide (H_2S) over metal modified alumina catalysts[20,67,68]. The reaction ($CH_3OH + H_2S \rightarrow CH_3SH$) is usually carried out at temperatures between 160 and 500 °C and pressures of 1 to 35 bar[18]. Significant yields of dimethyl ether (DME) and dimethyl sulfide (DMS) are also formed along with MeSH at typical

---

[3] Methionine - Global Market Trajectory & Analytics, July 2020, Global Industry Analysts, Inc.

reaction conditions[69]. In a non-recycle reactor system, these byproducts are separated from MeSH and disposed, resulting in a loss of carbon and sulfur[70]. Alternatively, DMS can be cleaved with hydrogen sulfide (H_2S) to recover MeSH via the following reaction in a secondary reactor: $(CH_3)_2S + H_2S \leftrightarrow CH_3SH$. This recovery will translate to higher overall methanethiol yield or decreased methanol and hydrogen sulfide raw material cost per yield. Although methanethiol selectivity values up to 90% could be achieved in a two-reactor system, the process is noticeably energy-intensive, since large excess of hydrogen sulfide needs to be circulated to suppress dimethyl sulfide formation[18-20,22]. This highlights the importance of reactors optimization to improve feed conversion and overall product yield, which initially requires obtaining an accurate kinetic description of the reaction system.

Kinetic modeling of catalytic reactions briefly consists of: i) conducting laboratory experiments, ii) model development, which includes the law of conservation equations and rate definitions, and iii) applying regression to determine kinetic parameters using all available experimental data. Since the ultimate aim of kinetic modeling is to improve the process by increasing throughput or reducing energy consumption, it is important to be able to predict kinetic behavior outside the current operating range with the estimated kinetic parameters[71,72]. If the model gets trained with data points including noisy and/or inaccurate entries, it may not categorize the data correctly, resulting in an over-fit and hence potentially spurious predictions. Ideally, to prevent this issue, a reasonable portion of the experimental measurements should be held out from model training, and the derived kinetic parameters should be tested on the unknown or hidden portion of the experimental dataset[73-75]. However, due to the limited number of experimental data available in this study, as typical for most industrial cases, holding out a portion of data to test derived kinetic parameters would result in significant information loss during kinetic model training. Instead in this work, cross-validation (CV) methodology, which is typically used in classification problems in machine learning[76-78], is implemented to estimate kinetic parameters with nonlinear least-squares robustly. CV is based on the splitting of the experimental data into two sets: “training set”, to build and predict the model, and “validation set”, to assess the model. The efficiency of this method stems from the fact that the fitting is repeated multiple times so that each data point is tested at least once to yield the final kinetic parameter set[73,79,80]. In this work, 10-fold CV is implemented, where splitting is repeated ten times with random subsets in each run. Within each iteration, a different fold of the data is left out for validation while the remaining nine folds are used for training the model[78,81]. Each run is weighted based on their sum of square errors on the respective test set to determine overall fit parameters. This methodology is adopted and tested towards obtaining the kinetic parameters of the methanol thiolation reaction network on CoMo/Al_2O_3 catalyst.

Subsequently, the construction of two-dimensional reactor models and reactor optimization is carried out. Although lab-scale experiments could be performed under isothermal conditions, temperature changes in both axial and radial direction are often observed in industrial-scale reactors due to increased throughput, and the lack of heavy inert dilution. Therefore, in this chapter, two-dimensional pseudo-homogeneous reactor models are built to accurately simulate the large-scale production of methanethiol. Conservation of mass, energy, and momentum equations describing the behavior of the system are derived, including modules for physical and thermodynamic property estimations. These mathematical models are further used to determine the operating conditions and reactor design to achieve optimum methanethiol yields.

3.2 Computational Methods

In this work, we aim to perform precise model-based development of optimal catalytic reactors for methanethiol production. The experimental data used here is provided by our industrial collaborators, which consist of steady state concentrations of species at different temperatures, inlet feed ratios, and residence time values. The scope of the computational work consists of kinetic modeling, reactor model development, and optimization. Computational tools developed in this thesis can be found at github.com/gio-veserlab.

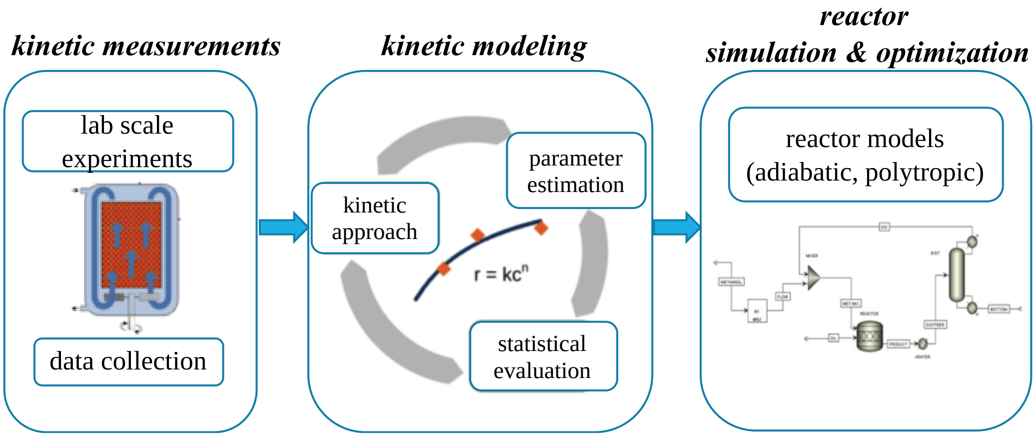

Figure 12 Workflow of the computational work

3.2.1 Kinetic Modeling

The kinetic model of the methanethiol (methyl mercaptan, MeSH) formation from methanol and hydrogen sulfide on CoMo/Al_2O_3 catalyst is adopted based on the reaction network proposed by Mashkina[82]. According to the literature research, the methanol thiolation is operated with a gas phase at high pressures (1-35 bar) and temperatures (160-500°C)[18]. For thermo-physical property estimation, Aspen Property Method Selection Assistant[83] is utilized. Peng-Robinson equation of state (EOS) model is selected, which is suitable for gases and liquids at high temperature and pressure values, and can describe non-ideal gas phase behavior even close to the critical point[84,85]. The relevant properties (molecular weight, density, and enthalpy) of all components are collected from the DETHERM[86] database in Aspen Properties software.

In the experiments, due to dilution of feed flow with inert, the temperature profile across the reactor is constant. Therefore, energy balance is not included in the kinetic model. The detailed derivation of model equations along with all relevant assumptions is given in Appendix B. The fixed-bed reactor is modeled as pseudo-homogeneous, in which only concentration gradients of the fluid transport are considered. Homogeneity assumptions are validated using Mears[87] criterion for external diffusion limitation and Weisz-Prater[88] criterion for internal diffusion limitation (Appendix C). The rate constants (k_i) are modeled in Arrhenius form including adsorption terms. The concentrations along the catalyst bed and at the reactor outlet are calculated with the reaction rate equations and the component balances. Accordingly, the kinetic model is constructed based on the following equations of conservation.

Component balance:

$$\frac{\partial C}{\partial t} = 0 = -\frac{1}{A_{CS}} \cdot \frac{\partial \dot{n}_j}{\partial z} + \frac{m_{Cat}}{V_R} \cdot \sum_i \nu_{ij} \cdot r_i \tag{3-1}$$

$$\text{at } z = 0\text{: } c_j = c_{j,inlet}, \text{ at } z = L\text{: } \frac{\partial c_j}{\partial z} = 0$$

where C is the concentration of each component (mol/m^3), A_{CS} is the cross-sectional area of the tube (m^2), $\dot{n}$ is the molar flowrate of each component (mol/s), m_{cat} is the catalyst weight (kg), V_R is the volume of the reactor (m^3), ν is the stoichiometric coefficient of each component and r is the rate of each reaction (mol/kg$_{cat}$/s).

Rate equations:

$$r_i = k_i \cdot \prod C_j^{e_j} \tag{3-2}$$

$$k_i = k_{i,0} \cdot \frac{\exp\left(-\frac{E_{A,i}}{R \cdot T}\right)}{\left(1 + \sum_j k_{a,j} \cdot c_j\right)^2} \quad , \quad k_{a,j} = k_{a,j,0} \cdot \exp\left(\frac{E_{A,a,j}}{R \cdot T}\right) \tag{3-3}$$

where k is the rate constant, k_0 is the pre-exponential factor and E_a (J/mol) is the activation energy of each reaction, k_a is the adsorption rate constant, $k_{a,0}$ is the adsorption pre-exponential factor and $E_{A,a}$ (J/mol) is the adsorption activation energy of each component. Conversion and selectivity values are calculated with the following equations:

$$\text{Conversion, species } i \;\; X_i = \frac{\text{moles of } i \text{ converted}}{\text{moles of } i \text{ in feed}} \tag{3-4}$$

$$\text{Product selectivity, species } j \;\; S_j = \frac{\text{moles of species } j \text{ formed}}{\text{moles of total products}} \tag{3-5}$$

$$\text{Product yield, species } j \;\; Y_j = X_i \times S_j \tag{3-6}$$

3.2.1.1 Parameter Estimation

Ordinary differential equations mentioned above are solved with a sparse system adaptive ODE solver “ode15s”, using Mathworks Inc. MATLAB® R2017a. For nonlinear data-fitting, “lsqnonlin” function is used through the Levenberg-Marquardt[89] approach with default tolerance values. The following objective function is used for the parameter estimation of pre-exponential factors ($k_{i,0}$), activation energies ($E_{a,i}$) and reaction orders:

$$Objective\ function = \sum_{i=1}^{m} \sum_{j=1}^{n} \left(C_{i,j}^{Exp} - C_{i,j}^{Model}\right)^2 \tag{3-7}$$

where C refers to the concentrations, i refers to the components (e.g. methanol or MeOH, hydrogen sulfide or H_2S, methanethiol or MeSH, dimethyl sulfide or DMS, dimethyl ether or DME, and dimethyl disulfide or DMDS), and j is the experiment index.

In the cross-validation[90] least squares (LS-CV) method, the experimental data is divided into two segments: One segment is used to train the model, while the other segment is then used for model validation. The typical form of cross-validation is a so-called "k-fold". In this approach, the data set is first divided into k equally sized folds. Within each iteration, a different fold of the data is left out for testing (or validation) while the remaining folds are used for training the model using non-linear least-squares. Random partition of the experimental data is carried out using the "crossvalind" function in MATLAB. k=10 is used for this work, i.e. the data is broken down into ten segments (Figure 13).

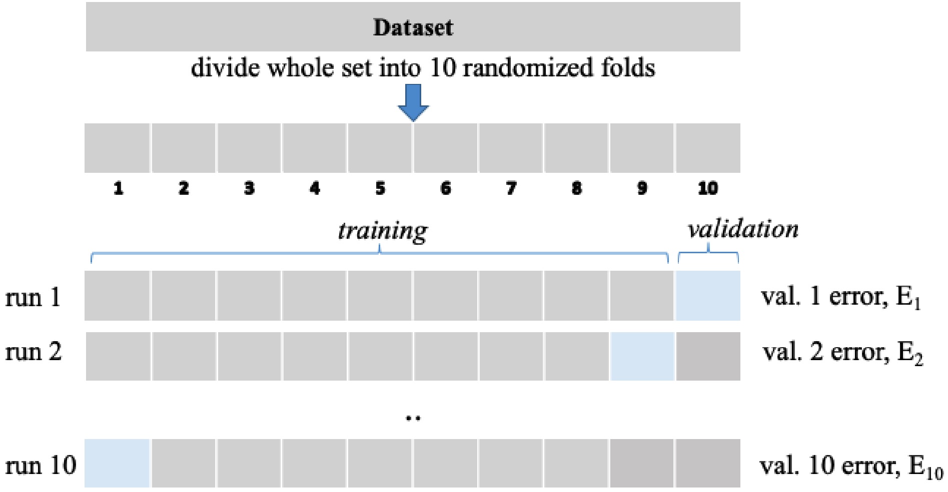

Figure 13 Schematic representation of 10-fold cross-validation[91]

Nine segments are used for model training via non-linear least-squares and the remaining segment is used for validation with the fitted parameters. All ten permutations of ten sets are used for full cross-validation. The final kinetic parameters are calculated by averaging each run weighted by their respective validation set error. Final values are obtained by the following:

$$\Theta = \sum_{i=1}^{10} \omega_i \theta_i , \qquad \omega_i = \frac{f_{i,test}}{\sum_{i=1}^{10} f_{i,test}} , \qquad f_{i,test} = \frac{1}{E_{i,test}^2} \tag{3-8}$$

where θ is the fitted parameters of each run, ω is validation error weight of each run and E is the validation set error of each run.

3.2.1.2 Sensitivity Analysis

Following the determination of kinetic parameters, local sensitivity analysis is performed to establish the significance of the reaction steps. Sensitivity analysis steps are as followed:

I. One parameter is varied at a time, keeping other parameters constant. The range of parameters span one order of magnitude from the original value.

II. Model output distribution (conversion, selectivity) is calculated.

III. Box and whisker plots are generated, which graphically show the distribution and variability of the model outputs (Figure 14). The boxes denote the interquartile range between 25% and 75%, which spans 50% of the outputs. The height of the box is proportional to the relative change of outputs, which shows the degree of sensitivity of the output to the specific parameter.

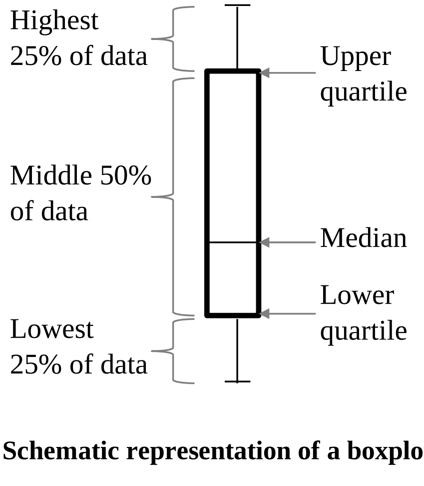

Figure 14 Schematic representation of a boxplot

3.2.2 Reactor Modeling

Following kinetic parameter determination, two-dimensional pseudo-homogeneous reactor models are built-in MATLAB environment to gain full autonomy for optimization. Conservation of mass, energy, and momentum equations describing the behavior of the system are derived. A brief description of 2D model equations is provided below. The detailed derivation of model equations, relevant assumptions, and numerical methods are given in Appendix B, Appendix C and Appendix D, respectively. Modules for physical and thermodynamic property estimations including mixing effects for Peng-Robinson equation of state are also scripted (see Section 3.2.3 and Appendix E). These modules are capable of accurately calculating relevant properties at elevated temperature and pressure values without requiring a connection to a database or an external software such as Aspen Properties.

Mass balance:

- *Component (mass) balance equations:*

$$\frac{\partial C}{\partial t} = 0 = -\frac{1}{A_{CS}} \cdot \frac{\partial \dot{n}_j}{\partial z} + \frac{m_{Cat}}{V_R} \cdot \sum_i \nu_{ij} \cdot r_i \tag{3-9}$$

$$\text{at } z = 0\text{: } c_j = c_{j,inlet}\text{, at } z = L\text{: } \frac{\partial c_j}{\partial z} = 0$$

where C is the concentration of each component (mol/m^3), A_{CS} is the cross-sectional area of the tube (m^2), $\dot{n}$ is the molar flowrate of each component (mol/s), m_{cat} is the catalyst weight (kg), V_R is the volume of the reactor (m^3), ν is the stoichiometric coefficient of each component and r is the rate of each reaction (mol/kg_{cat}/s).

- *Rate equations:*

$$r_i = k_i \cdot \prod C_j^{e_j} \tag{3-10}$$

$$k_i = k_{i,0} \cdot \frac{\exp\left(-\frac{E_{A,i}}{R \cdot T}\right)}{\left(1 + \sum_j k_{a,j} \cdot c_j\right)^2} \quad , \quad k_{a,j} = k_{a,j,0} \cdot \exp\left(\frac{E_{A,a,j}}{R \cdot T}\right) \tag{3-11}$$

where k is the rate constant, k_0 is the pre-exponential factor and E_a (J/mol) is the activation energy of each reaction, k_a is the adsorption rate constant, $k_{a,0}$ is the adsorption pre-exponential factor and $E_{A,a}$ (J/mol) is the adsorption activation energy of each component.

2D energy balance (final form):

$$\frac{\lambda_e}{r}\left(\frac{\partial\left(r\frac{\partial T}{\partial r}\right)}{\partial r}\right) + \lambda_e \frac{\partial^2 T}{\partial z^2} + \Delta H_{Rx} r_i \rho_c - \left(U \sum C_i C_{Pi}\right)\frac{\partial T}{\partial z} = 0 \tag{3-12}$$

where λ_e is the bed thermal conductivity (W/mK), T is the fluid temperature (K), ΔH is the heat of reaction (J/mol), r is the rate of each reaction (mol/kg/s), ρ_c is the catalyst density (kg/m^3) and C_p is the fluid heat capacity (J/molK).

- *Boundary conditions:*

at r = 0: $\frac{\partial T}{\partial r} = 0$ (symmetry condition)

at z = 0: $T = T_{inlet}$, at z = L: $\frac{\partial T}{\partial z} = 0$ (inlet and finite condition at the exit)

(3-13)

at r = R_t: $-\lambda_e \cdot \frac{\partial T}{\partial r} = \alpha_W \times (T - T_W)$ for polytropic case (coolant)

at r = R_t: $-\lambda_e \cdot \frac{\partial T}{\partial r} = 0$ for adiabatic case

where R_t is the radius of a tube (m), T_w is the coolant temperature (K), and α_w is the coolant heat transfer coefficient (W/m^2 K).

- *Bed thermal conductivity (Bauer and Schlünder, 1978[92]):*

$$\frac{\lambda_e}{\lambda_f} = \left(1 - \sqrt{1-\varepsilon}\right) + \frac{2\sqrt{1-\varepsilon}}{1 - B\kappa^{-1}} \frac{B(1-\kappa^{-1})}{(1-B\kappa^{-1})^2} ln\left(\frac{\kappa}{B}\right) - \frac{B-1}{1-B\kappa^{-1}} - \frac{B+1}{2} \tag{3-14}$$

$$B = 1.25 \frac{1 - \varepsilon^{1.11}}{\varepsilon} \tag{3-15}$$

where λ_e and λ_f are the bed thermal conductivity and the fluid thermal conductivity (W/mK), respectively, ε is the void fraction, κ is the ratio of fluid thermal conductivity to bed material thermal conductivity without any geometric specification.

Momentum Balance (Ergun[93] equation):

$$\frac{dp}{dz} = -f_1 u_0 - -f_2 {u_0}^2 \tag{3-16}$$

$$f_1 = 150 \frac{(1-\varepsilon)^2}{\varepsilon^3} \frac{\eta_f}{\left(d_p^v\right)^2} \qquad f_2 = 1.75 \frac{1-\varepsilon}{\varepsilon^3} \frac{\rho_f}{d_p^v} \tag{3-17}$$

where u_0 is the linear flow velocity (m/s), ε is the void fraction, η_f is the flow viscosity (Pa-s), ρ_f is the flow density (kg/m^3) and $d^v{}_p$ is the particle diameter (m).

The reactor model equations are solved using ode15s function in MATLAB. Relative and absolute tolerances are selected as 1E-6 and 1E-9, respectively. Explanation of numerical methods for solving energy balance PDEs is given in Appendix D.

3.2.3 Physical Property Estimation

In contrast to kinetic measurements taken under isothermal conditions, developed reactor models include energy balance equations to account for axial and radial temperature changes across the reactor. Therefore, temperature dependent thermophysical and transport properties of the gaseous species in the reactor should be estimated. Due to typical elevated operating pressure and temperature values of the reaction system, cubic equations of state (EOS) are used in addition to the ideal gas law. Based on the property method selection assistant of Aspen Properties, Peng-Robinson EOS[94] is selected, which is suitable for high-pressure real nonpolar gases. Correlations for transport properties are listed in Table 1 and the relevant equations are given in Appendix E.

Table 1 Property correlations

Property	Correlation	Ref.
Density	Peng-Robinson EOS	94
Heat Capacity (enthalpy)	Peng-Robinson EOS	
Viscosity	Pure: DIPPR Equation # 102	95
	Mixture: Chapman-Enskog Brokaw with Wilke mixing rule	96
	Pressure correction: Stiel-Thodos	
Thermal conductivity	Pure: DIPPR Equation # 102	95
	Mixture: Wassiljewa-Mason-Saxena	96,97

3.2.4 Reactor Optimization

Prior to optimization, constructed reactor models are used for parameter sensitivity analysis to determine reasonable upper and lower bounds for each free parameter. Sensitivity analysis is performed on base operating conditions (temperature, pressure, WHSV) and reactor geometry (number of tubes, tube diameter, tube length, catalyst weight) for both rectors, which is determined by published patents on methyl mercaptan production[20,98,99] and company operations.

Reactor optimizations are carried out with nonlinear constraint minimization of an objective function using MATLAB’s GlobalSearch algorithm (fmincon). This algorithm uses a scatter-search mechanism to generate multiple start points within given parameter bounds to achieve a global minimum. The objective function for the optimization is determined as -methanethiol productivity (outlet MeSH rate per gram of catalyst, kg/h^{-1}g), or -methanethiol yield (Y_{MeSH}). Optimal process conditions and reactor specifications for adiabatic and polytropic operation are determined based on 1) base geometry and 2) new reactor design. Tube length to tube diameter ratio is not allowed to be below 20 to avoid axial dispersion. For all optimizations, the only fixed parameter is the inlet MeOH flowrate of 6250 kg/h, which is the pre-determined target throughput.

3.3 Results and Discussion

This section has been removed from the public version of this dissertation due to confidential data.

3.4 Conclusion

This section has been removed from the public version of this dissertation due to confidential data.

4.0 Determining Robust Reaction Kinetics from Limited Data

4.1 Introduction

Precise knowledge of kinetic parameters of a chemical reaction system is fundamental not only for improving our understanding of underlying chemical processes, but also for the accurate design, optimization, and robust operation of reactors[100-102]. Kinetic models of reactive systems allow rapid exploration of the reaction outcome over a wide range of operating conditions[103], the design of new experiments, and are even used for safety training[104,105].

In practice, a kinetic model is typically derived from of the fundamental material, energy and momentum balances, equilibrium or reaction rates[106-108]. Training of the kinetic model parameters then requires a set of laboratory experiments or availability of data from an operating plant, where the acquisition of data is often expensive or challenging[109-111]. While much focus is currently on high-throughput screening and "big data" approaches, in industrial practice, availability of data is typically limited and often a relatively small number of data points have to suffice to identify kinetic parameters of a chemical reaction[112,113]. Regular nonlinear least-squares fitting is most commonly used in kinetic fitting of the experimental data[114-116]. However, the method is well-known to be sensitive to noise and, due to the deterministic nature of the method, least-squares estimation can get stuck at local minima[117,118]. To circumvent this issue, more sophisticated optimization methods such as Markov chain Monte Carlo (MCMC), or genetic algorithm (GA) are used to explore parameter spaces more efficiently[103,119,120]. MCMC performs a random walk in parameter space and may accept "bad" moves probabilistically (movements in the direction of increasing objective function) to escape local minima[24,121]. GA, on the other hand, is a population-based algorithm that performs parameter estimation based on the "survival of the fittest" in real life evolution[25,122]. However, both of these methods require expert knowledge and higher computation cost, although all implementations of GA and some implementations of MCMC are parallelizable[123].

In recent decades, significant advancements have been made towards building supervised learning models from big data for fault detection, process modeling and control of chemical reactions[124-127]. However, statistical validation of model-based reaction kinetics from limited data, which is still typical in industrial practices, is often overlooked. Regardless of the choice of algorithm, the accuracy of the kinetic prediction is often assessed by the error value of the regression which shows how well the model parameters match the experimental data[71,128]. However, assessing the accuracy of the model based on the very same data that it was trained on may result in significant overfit, in which the model "memorizes" the specific set of data, rather than "learning" the underlying trends[126,129,130]. This severely limits the capability of the model to truly predict system behavior. Moreover, complex algorithms are more likely to overfit when data is limited[71]. To prevent overfitting, models need to be validated on data they have not seen yet[131,132]. For this purpose, a portion of the experimental data, the "hold-out" (ideally 10-30% of the available data), is set aside to be used for validating after the model is trained[133,134]. However, it can be challenging to hold out or exclude a fraction of the available data from model training in particular if availability of data is already limited. Besides, the selection of data for hold-out may not be straightforward. For example, if the noise level or the number of outliers present in the validation data is significantly higher than in the training data, model assessment can become highly inaccurate[132].

As a solution to this problem, a cross-validation (CV) methodology can be applied to the kinetic parameter regression[135]. This method is commonly used in classification problems in machine learning for accuracy reporting, in which the prediction output belongs to a discrete set of categories or classes[136-138]. CV, similar to the "hold-out" method described above, is based on the splitting of the experimental data into two sets: a "training set" to build and predict the model parameters, and a "validation set" to assess the quality of the model. For this purpose, the experimental dataset is partitioned into k nearly equal-sized subsets or "folds". The model is trained using (k-1) folds, and the accuracy of the model is then validated on the fold that was left out (i.e. the k^{th} fold). This step is repeated k times for each possible permutation of folds with a different subset left out each time as the validation fold. Upon completion, kinetic parameters from all runs are then averaged based on the error of their respective validation subset[135].

In contrast to classification problems and machine learning, application of CV to nonlinear regression problems is rarely used for kinetic parameter estimation to-date[127,139-141]. Yet, it can be implemented in a straightforward extension of the conventional nonlinear least-squares fitting procedure and can be expected to yield significant benefits towards obtaining robust kinetics. This is particularly true for cases with limited data availability, since CV ensures that the model is ultimately trained with each data point, and, similarly, each data point has a chance of being validated against the model parameters. In addition, due to the statistical averaging of the successive runs, the possibility of an overfit is minimized, improving the model's true predictive ability.

In the present work, a straightforward proof-of-concept study is employed to compare different algorithms for robust kinetic parameter estimation with limited data availability. Specifically, cross-validation is applied to nonlinear least-squares fitting, and compared to regular non-linear least-squares[142], MCMC[24], and GA[25] algorithms for kinetic parameter estimation. The analyses are performed on synthetic data for the purpose of probing dataset properties such as size (number of experimental points), noise level, and number of outliers. The water-gas shift reaction (WGS: $CO + H_2O \rightleftharpoons CO_2 + H_2$) with simple, well-established lumped kinetics is used as the basis for a simple one-step model reaction[23]. Synthetic data is generated by simulating the kinetic model over a series of operating conditions and adding controlled levels of Gaussian white noise and outliers to the generated data points. Method performance measured in both accuracy (prediction accuracy of the true reaction kinetics) and numerical efficiency (number of function evaluations) are critically compared. The overall aim of the study is to yield guidelines for the practitioner towards improved, robust kinetic data fitting without requiring advanced training in mathematical methods.

4.2 Computational Methods

4.2.1 Model Construction

A simple isothermal steady-state kinetic plug-flow reactor model is constructed using conservation of mass equations and typical Arrhenius-type reaction kinetics:

$$\frac{\partial Cj}{\partial t} = 0 = -\frac{1}{A_{CS}} \cdot \frac{\partial \dot{n}_j}{\partial z} + \frac{m_{Cat}}{V_R} \cdot \sum_i \nu_{ij} \cdot r_i \qquad (4\text{-}1)$$

$$\text{at } z = 0\text{: } c_j = c_{j,inlet}, \quad \text{at } z = L\text{: } \frac{\partial c_j}{\partial z} = 0 \qquad (4\text{-}2)$$

where C is the concentration of each component (mol/m^3), A_{CS} is the cross-sectional area of the tubular reactor (m^2), $\dot{n}$ is the molar flowrate of each component (mol/s), m_{cat} is the catalyst weight (kg), V_R is the volume of the reactor (m^3), r_i is the rate of each reaction (mol/kg$_{cat}$/s) and ν is the stoichiometric coefficient of each component. Rate equations are described by typical power law kinetics:

$$r_i = k_{i,0} \cdot \exp\left(-\frac{E_{A,i}}{R \cdot T}\right) \cdot \prod C_j^{e_j} \tag{4-3}$$

where r_i is the rate of each reaction (mol/kg$_{cat}$/s), $_{i,0}$ is the pre-exponential factor of ith reaction, E_a (J/mol) is the activation energy of each reaction. Conversion values are calculated with the following equation:

$$\text{Conversion, species } i \;\; X_i = \frac{C_{i,0} - C_i}{C_{i,0}} \tag{4-4}$$

In this work, water-gas shift (WGS) is chosen as a simple, industrially relevant model reaction as a starting point with well-known kinetics[23]. However, an initial model evaluation revealed that one of the existing parameters, $k_{0,bwd}$, is not identifiable (explained further below in this section) due to the relatively low backward reaction rate, which may result in wrong interpretation of the analyses. The value of $k_{0,bwd}$ is hence increased by an order of magnitude for generating synthetic data to ensure that all parameters are identifiable. Therefore, the model reaction is presented as a generic reaction throughout the paper ($A + B \rightleftharpoons C + D$) with parameters given in Table 2. Synthetic data is generated by using kinetic parameters and reactor geometry for the model reaction and solving the material balance equations to determine concentration of each species at the reactor exit.

Table 2 Kinetic parameters and reactor specifications of the model reaction

Parameters			Specifications		
$\mathbf{k_{0,fwd}}$	3.0E05	molgcat^{-1} h^{-1}atm^{-2}	**tube dia.**	0.5	inch
$\mathbf{k_{0,bwd}}$	2.5E08	molgcat^{-1} h^{-1}atm^{-2}	**tube length**	1	ft
$\mathbf{E_{a,fwd}}$	5.0E04	J/mol	**catalyst wt.**	1	kg

Experimental data (inlet and outlet concentration values) is generated over the following parameter ranges: temperature (150-250°C), molar inlet A to B ratio (0.25-4), and gas hourly space velocity (GHSV) (0.25-2.5h^{-1}). After synthetic data is generated, varying levels of gaussian white noise are added to concentration values. If the added noise generates a concentration that is out of physical range (e.g. negative values), the procedure is repeated.

- *Local sensitivity*

Following model construction and data generation, sensitivity analysis is carried out to determine how strongly a given parameter and the model outcome are correlated[143,144]. The analysis is performed via calculating finite-difference based sensitivity coefficients by applying a small change to one parameter at a time for a given axial displacement (z):

$$s_{i,j}(z) = \frac{\partial x_i}{\partial \theta_j} = \frac{x_i(\theta_j + \Delta\theta_j, z) - x_i(\theta_j, z)}{\Delta\theta_j} \tag{4-5}$$

where θ is the fit parameter, x is the dependent variable (e.g. concentration). These sensitivity coefficients are then normalized for direct comparison:

$$\overline{s_{i,j}}(z) = s_{i,j}(z) \times \frac{\theta_j}{x_i} \tag{4-6}$$

Finally, relative sensitivity (RS) is calculated for each parameter:

$$RS_{i,j} = \frac{1}{Q_Z}\sqrt{\sum_{k=1}^{Q_z}\left|\overline{s_{i,j}}(z_k)\right|^2} \tag{4-7}$$

where z_k ($k \in [1, Q_Z]$) are discrete axial displacements where concentrations are calculated and Q_Z is the total number of calculations.

- *Profile likelihood*

Finally, profile likelihood analysis is performed to determine if model parameters are identifiable with the generated experimental data set. For this purpose, a log-likelihood (LL) value is calculated from model fitting, which is proportional to the normalized sum of square errors[145]:

$$LL \cong -\frac{1}{2}\sum_i \frac{\left(y_i - g(z,\theta)\right)^2}{\sigma^2} \tag{4-8}$$

where y is the experimental data (e.g., concentration), g is the model-predicted output at independent variable z (axial displacement) calculated with fit parameter set θ, σ is the standard deviation of the experimental data. Profile likelihood is the maximum log-likelihood, i.e., the value of LL when the objective function is minimized:

$$PL_j(p) = \max_{\theta \in (\theta | \theta_j = p)} LL(y|\theta) \tag{4-9}$$

where p is the fixed parameter value, LL is the log-likelihood and θ is the parameter set. The profile-likelihood (PL) is calculated by optimizing fit parameters while keeping one parameter at a time, θ_j, at a pre-set value p. The optimization is repeated for a discrete range of the fixed parameter ($\theta_j \in [\theta_{j,min}, \theta_{j,max}]$) and PL values of each estimation are plotted. If the resulting PL landscape does have a unique minimum, and exceeds the 95% confidence threshold, the parameter is termed identifiable and estimable from the experimental data[145].

4.2.2 Parameter estimation

In order to assess the predictive ability of each parameter estimation method, 20% of the synthetic data is held out for external testing, and the remaining 80% of the data is used towards model training. For the purpose of distributing the synthetic data evenly between training and test sets, stratified sampling is carried based on input conditions (e.g., temperature) instead of random sampling. After adding the same level of noise to each set, the model is trained with the generated data (Figure 15).

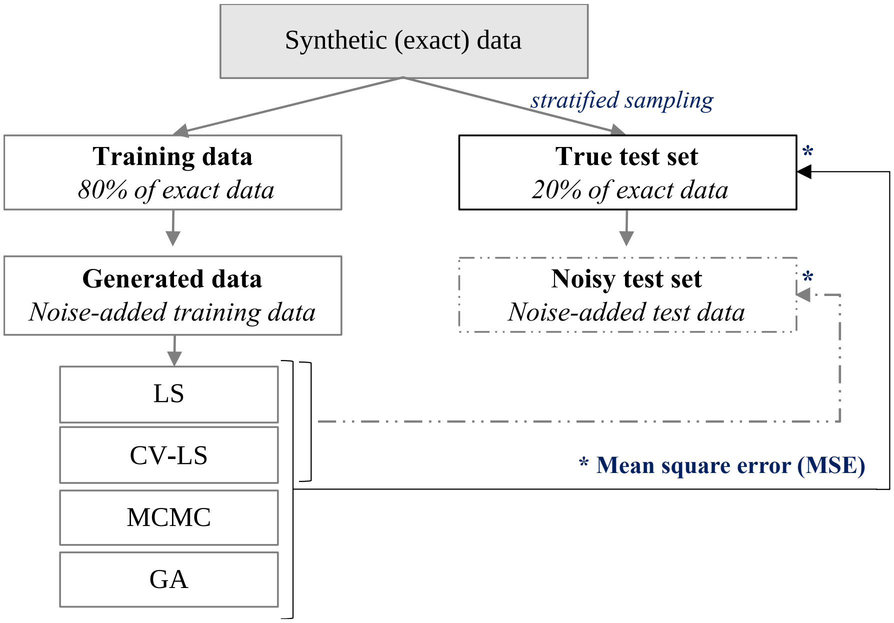

Figure 15 The simplified schematic of the computational workflow

Agreement with true kinetics is determined by calculating the mean square error (MSE) of the “true test set”, which is generated from real kinetic parameters. Comparison of estimated and real parameters is also tabulated in Table S1-3. In addition, the MSE of the “noisy test set” is reported as a representative metric of a real-life scenario where the true kinetics is not known, and only noisy experimental data will be available for testing. The number of function evaluations is also used to directly compare the computational cost of all four methods. 50 repeat runs are carried out for each analysis to report statistical significance of the results. For the direct comparison of all methods where the same generated data is used for parameter estimation, t-tests are carried out. For statistical comparison of LS and LS-CV methods where a different dataset is generated for each repeat run, paired t-tests are performed. Prior to paired t-testing, Kolmogorov-Smirnov test is performed to ensure the generated datasets are normally distributed[146,147].

Non-linear least-squares (LS): The LS regression is performed using MATLAB’s *lsqnonlin* function based on Levenberg-Marquardt (LM) method with default tolerance values[142]. LM method optimizes the objective function by searching a new direction in the parameter landscape moving in the minimized-gradient direction:

$$Objective\ function = \sum_{i=1}^{m}\sum_{j=1}^{n}\left(C_{i,j}^{Exp} - C_{i,j}^{Model}\right)^2 \tag{4-10}$$

where C refers to the concentrations, i refers to the components and j refers to the experimental (generated) data point for each component.

Cross-validation nonlinear least-squares (LS-CV): For LS-CV, data is divided into folds via stratified sampling using *crosvalind* function in MATLAB. Stratified sampling assures that the distribution of the input conditions (e.g., temperature) on the overall dataset is represented similarly on the individual folds[148]. Within each run, a different fold of the data is left out for validation while the remaining folds are used for training the model using nonlinear least-squares fitting[78,81]. The runs are repeated k times (the number of folds). As a result, an ensemble of parameters and the associated validation errors are obtained from each run, which are then weighted based on their respective validation errors to determine overall fit parameters:

$$\Theta = \sum_{i=1}^{k} \omega_i \theta_i, \ \ \omega_i = \frac{1/E_{i,test}^2}{\sum_{i=1}^{k} 1/E_{i,test}^2} \tag{4-11}$$

where θ is the fitted parameters of each run, ω is validation error weight, E is the validation error of each run, and k is the number of folds, which was chosen to be 5 for a dataset size of 25, and 10 for all others.

Markov chain Monte Carlo (MCMC): MCMC is performed using the Metropolis Hasting algorithm[149]. The random walks are sampled from a log-normal distribution for pre-exponential factors and from a normal distribution with a standard deviation of 5000 kJ/mol for activation energies. Each move that reduces the objective function is accepted. Moves that increase the objective function are accepted if the calculated Metropolis criterion is larger than a uniformly generated random number. The Metropolis criterion is calculated using the following formula:

$$\beta = e^{\frac{-(SSE_{new} - SSE_{old})}{2\sigma^2 T}} \tag{4-12}$$

where β is the Metropolis criterion, SSE is the sum square error, σ^2 is the variance of the SSE values and T is the temperature factor which adjusts the stringency of the algorithm, which is selected as 3 for dataset size of 25 and 5 for others. Metropolis Hasting is implemented with a simulated annealing algorithm, which slowly decreases the probability of accepting worse solutions as the solution space is explored[150,151]. Based on 20 initial realizations performed using three different noise level and data set size combinations with 50000 iterations, the maximum number of iterations is selected as 20000 since no improvement after 20000th step is observed.

From the analysis on the same set of realizations, the runs are terminated if the best objective function does not change for 2000 steps.

Genetic algorithm (GA): The GA generates a group of candidate parameters (population) which are generated from a given parameter space with Latin hypercube sampling[152]. The initial population size is selected as 400, and the elitism parameter is selected as 0.1, which discards the parameter candidates that rank below the top 10% based on the objective function. The elite population is used to generate a new population using a "crossover" procedure, in which the parameters of two randomly selected samples from the elite population are averaged with random weights generated from standard uniform distribution to create new offspring. This procedure is repeated until population size reaches 400. Lastly, 10% of candidate parameters are subjected to mutation, which introduces diversity into the population by allowing random walk (factored by a log-normal random variable) of the parameter space. The optimization is terminated if the best objective function does not improve for 20 generations.

4.3 Result and Discussion

4.3.1 Model Evaluation

Initially, synthetic data is generated by simulating the constructed reaction model at steady state conditions with varying operating conditions, and by adding controlled levels of noise, as described in Section 4.2.1. Ranges of these operating conditions are selected to ensure that the data covers a wide range of conversion values to avoid a highly localized kinetic model. A representative noise-added generated data along with the distribution of conversion is shown in Figure 16.

Prior to parameter estimation, local sensitivity and profile likelihood analysis is performed on the kinetic model to ensure that the model parameters are identifiable and have a significant effect on the model outcome, i.e. that the problem is well posed. In practice, kinetic modeling studies are typically conducted under the assumption that the model parameters are identifiable based on the available experimental data without verifying this assumption. These pre-analysis tools could be useful for experimentalists and practitioners to establish confidence in fitted parameters, model reduction, and the design of experiments[153]. Accordingly, the calculated relative sensitivities, which are expressed as the percent change in output concentrations of all species due to a slight change (1%) in model parameters, are shown in Table 3. Model outputs are sensitive to all kinetic parameters, activation energy having the highest relative sensitivity due to exponential relation in the Arrhenius equation.

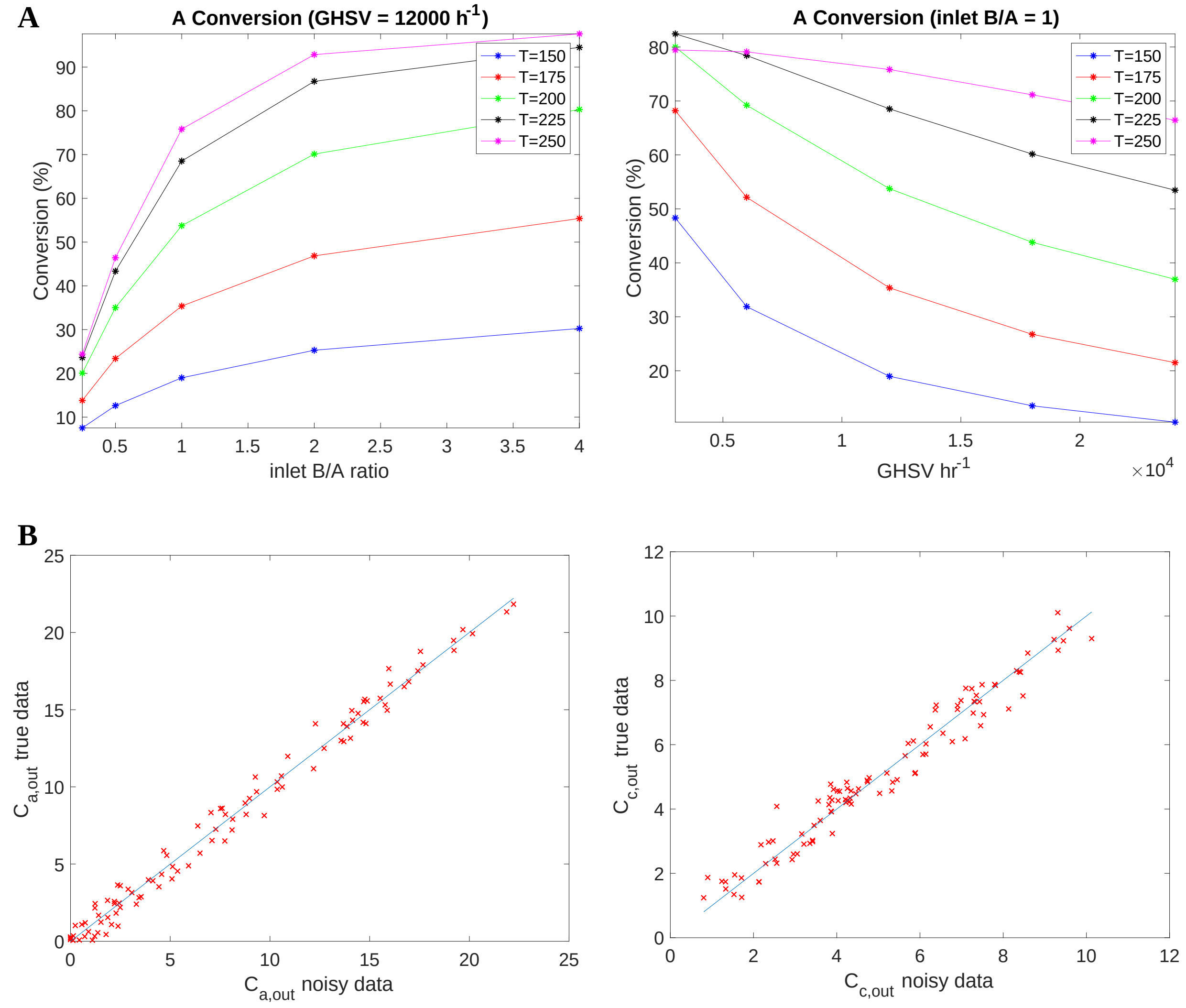

Figure 16 A) The distribution of species A conversion under varying operating conditions (inlet temperature, input ratios and GHSV values), and B) Representative generated concentration data of species A and species C (dataset size: 100, noise level:0.1)

Table 3 Relative sensitivities of kinetic parameters to output variables

Relative Sensitivity (%)	C_A	C_B	C_C	C_D
$k_{0,fwd}$	7.47	7.47	7.43	7.43
$k_{0,bwd}$	6.27	6.27	3.50	3.50
$E_{A,fwd}$	86.26	86.26	89.07	89.07

Similarly, likelihood profiles are generated using representative generated data, which are given in Figure 17. The presence of clearly defined minima in the identifiability plots for the pre-exponential factors and the activation energy confirms that the model parameters are estimable within the temperature range tested here (150-250℃).

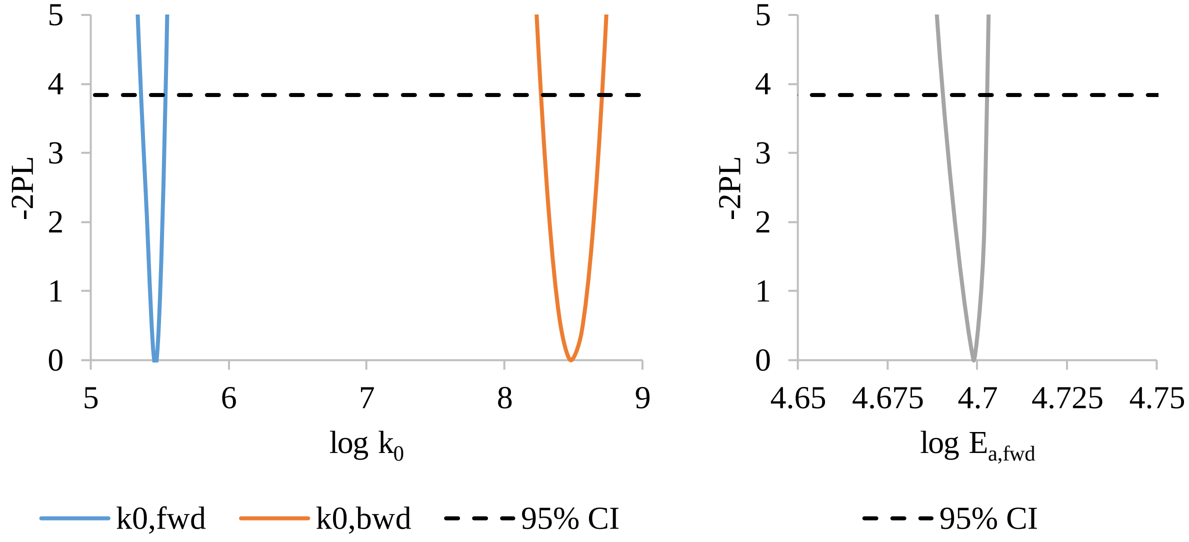

Figure 17 Profile likelihood plots for the model parameters (For plotting purposes, the minimum of -2PL is subtracted from all -2PL values.)

4.3.2 Accuracy and Efficiency Comparison of All Methods

In the first stage of our comparative study, all four methods (LS, LS-CV, MCMC, and GA) are comparatively evaluated with regard to their accuracy and computational efficiency. This comparative parameter estimation study is carried out using three different pairs of dataset size (n) and noise levels (nl) to observe the effect of dataset properties on model performances. All 3 operating variables can take on 5 discrete values (Figure 16A), resulting in a maximum dataset size of 125 datapoints. Three subset sizes (n = 25, 50, and 100) were chosen, each with a different noise level (decreasing from nl=0.5 for the smallest dataset to nl = 0.1 for the largest one), resulting in the following combinations for the analysis: data set 1: n=25, nl=0.5; dataset 2: n=50, nl=0.2; dataset 3: n= 100, nl=0.1. The accuracy of the methods is determined based on their closeness to the true kinetics, as indicated by the MSE against the test set (Figure 18). In addition, the efficiency or computational cost is determined by the number of function evaluations required to derive the parameters (Figure 19). For stochastic methods (MCMC, GA, LS-CV), 50 repeat runs are carried out on the same generated dataset and training-test split for direct comparison and the statistical significance is reported by p-values (Table 4 and Table 5).

Kinetic accuracy comparison of all methods with different dataset size and noise level combinations are shown in Figure 18. Distribution of test set MSE values for LS-CV, MCMC and GA methods are shown in boxplots, in which mean and median values are shown by “x” and “–”, respectively. The interquartile range is shown by box, whereas the outliers are denoted by the dots. The list of derived kinetic parameters is given in Appendix F. As apparent in the MSE distribution plots, LS-CV and the stochastic methods are able to predict the true kinetics with comparable accuracy for the cases with larger number of datapoints (n:50,100) and lower noise levels (nl:0.1, 0.2), and all three outperform the simple nonlinear least-squares (LS) method (Figure 18A-B). Similar to MCMC and GA, LS-CV is able to escape local minima due to statistical averaging of successive runs. Slight differences in mean errors are observed for LS-CV, MCMC and GA methods, but they are not statistically significant for these datasets (Table 4). In contrast, for the runs with a smaller number of datapoints and relatively higher noise (n:25, nl:0.5), LS-CV significantly outperforms both MCMC and GA methods in terms of accuracy of true kinetics (see Figure 18C). In these runs, both MCMC and GA had the lower training errors amongst all methods, i.e. they appear to fit to the data much better. However, since these methods also overfitted to experimental noise in the data, they failed to capture underlying kinetics, hence higher MSE on true test set. On the other hand, CV implementation efficiently filters out noise in the data due to the model validation which is based on all possible permutations of the (noisy) data.

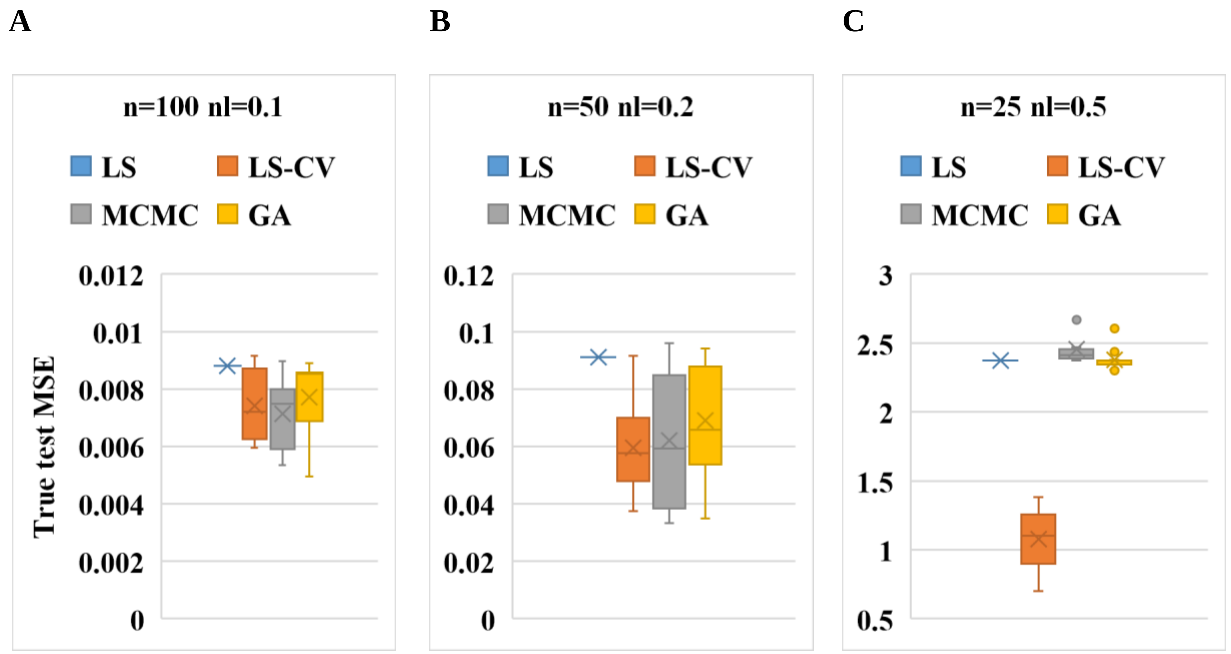

Figure 18 Kinetic accuracy (test set MSE) comparison of all methods with different dataset size and noise level combinations (A: n=25, nl=0.5; B: n=50, nl=0.2; C: n= 100, nl=0.1). Mean and median values are denoted by "x" and "–", respectively. Note that the magnitudes of y-axes are different.

The number of function evaluations necessary to perform the parameter estimation task is used to compare the computational efficiency of the four different methods. As expected, LS requires the lowest number of function evaluations due to the deterministic nature of the optimization algorithm. The total number of objective function evaluations is increased significantly for more complex algorithms, MCMC and GA, due to their stochastic nature, smart random walk strategies, and implemented rules against local minima. Due to population size, GA requires the highest number of function evaluations, although estimations with independent candidate parameter sets could be run in parallel. LS-CV, although less efficient than regular LS, requires 3- to 10-fold lower number of function evaluations compared to MCMC and GA.

Similarly, an order of magnitude increase in run time from LS-CV to the probabilistic methods are also observed (all runs were performed on Intel(R) Core(TM) i7 3.70GHz, 6 Cores.) This increased efficiency of LS-CV is found consistently across the datasets, as confirmed by t-test performed on different data set size and noise level combinations (Table 5), and suggests that CV implementation to LS can provide a straightforward solution to parameter estimation problems with minimal complexity while obtaining comparable or better accuracy than more complex stochastic methods.

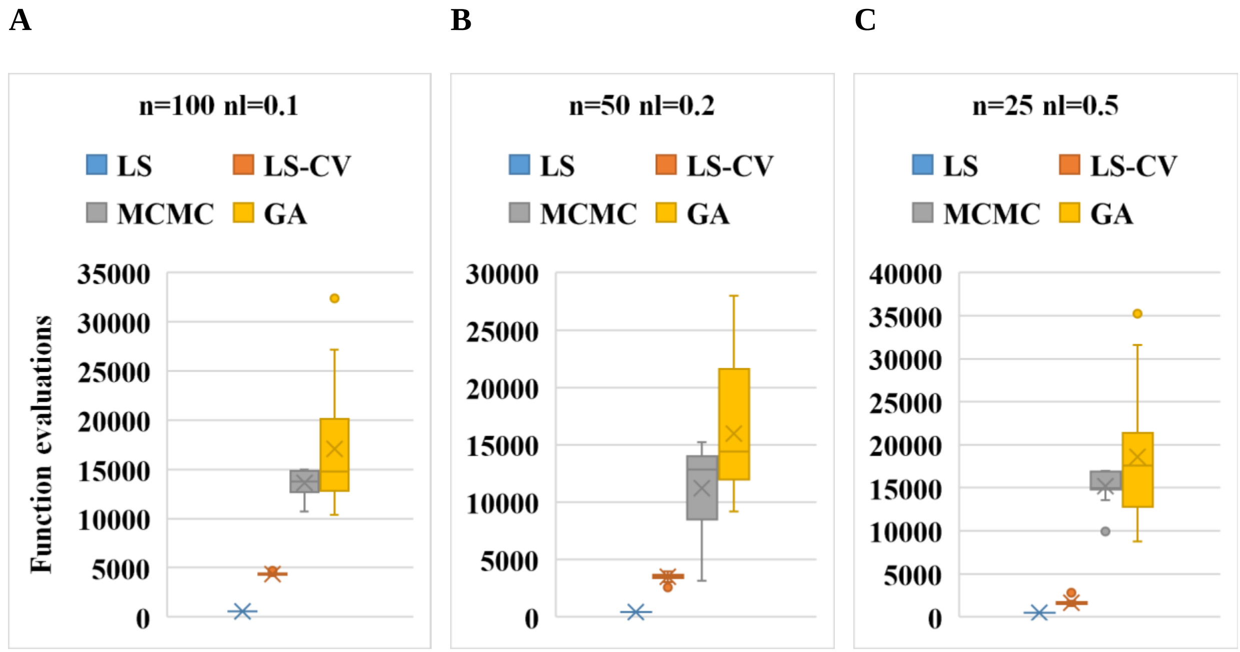

Figure 19 Computational cost (number of function evaluations) comparison of all methods with different dataset size and noise level combinations (A: n=25, nl=0.5; B: n=50, nl=0.2; C: n= 100, nl=0.1). Mean and median values are denoted by "x" and "–", respectively.

Table 4 Statistical analysis of kinetic accuracy (test set MSE) comparison of all methods with different dataset size and noise level combinations (p-value code: *<<0.00001)

	n=100 nl= 0.1			n=50 nl= 0.2			n=25 nl= 0.5		
	LS-CV	MCMC	GA	LS-CV	MCMC	GA	LS-CV	MCMC	GA
mean	0.0074	0.0071	0.0077	0.0596	0.0622	0.0690	1.0789	2.3916	2.2023
variance	1.2E-03	1.2E-03	1.3E-03	1.4E-02	2.5E-02	1.9E-02	2.1E-01	9.2E-02	2.6E-01
p-value		>0.05	>0.05		>0.05	>0.05		*	*

Table 5 Statistical analysis of computational cost (number of function evaluations) comparison of all methods with different dataset size and noise level combinations (p-value code: *<<0.00001)

	n=100 nl= 0.1			n=50 nl= 0.2			n=25 nl= 0.5		
	LS-CV	MCMC	GA	LS-CV	MCMC	GA	LS-CV	MCMC	GA
mean	4381	13657	17089	3494	11212	15973	1652	15198	18582
variance	132	1314	5975	259	3972	5452	285	1648	6960
p-value		*	*		*	*		*	*

4.3.3 Effect of Dataset Size, Noise and Outliers

Based on the above comparison between the three advanced methods (LS-CV, MCMC, and GA), LS-CV is down-selected for a more detailed investigation of the effect of dataset properties, namely dataset size, noise, and outliers, in comparison to simple LS. Performance comparisons are conducted on independently generated datasets for each run to ensure that results are reproducible on different datasets. In other words, using the same kinetic model and noise level, multiple random dataset generations and training-test splits are performed. Hence, paired t-tests are carried out to evaluate statistical significance after conducting Kolmogorov-Smirnov Test of Normality[146,147] to confirm data distribution can be assumed to be normal. The analyses are conducted with all possible combinations of three levels of dataset sizes (25,50,100) and four levels of noise (0.1, 0.2, 0.3, 0.5). The accuracy of the parameter estimation, similar to the previous study, is determined based on the MSE against the test set.

Kinetic accuracy (test set MSE) comparison of LS and LS-CV methods with increasing level of noise and dataset size is illustrated in Figure 20 by a representative run whereas the statistical analysis of all repeat runs is shown in Table 6. The list of derived kinetic parameters is given in Appendix F. Accordingly, LS-CV outperforms the regular LS fitting in all cases with varying levels of improvement. Paired t-tests for all runs show statistical significance of the results ($p < 0.01$).

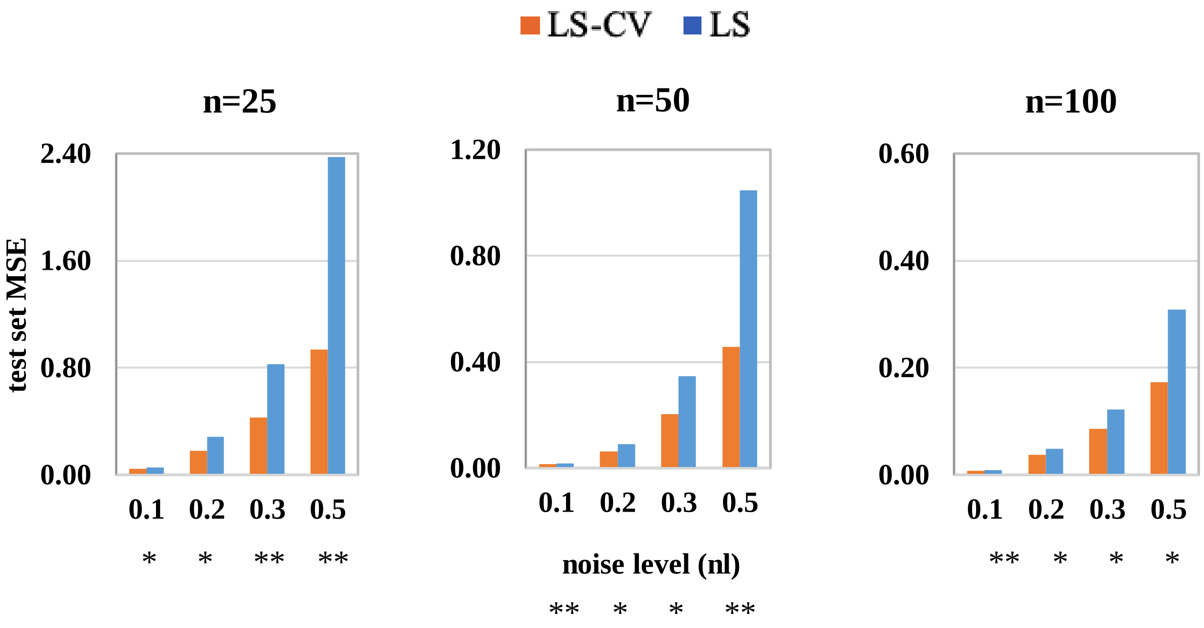

Figure 20 Kinetic accuracy (test set MSE) comparison of LS and LS-CV methods with all dataset size and noise level combinations (p-value codes: *<0.0001, **<0.01)

Table 6 Statistical analysis of kinetic accuracy (test set MSE) comparison of LS and LS-CV methods with all dataset size and noise level combinations (p-value codes: *<0.0001, **<0.01)

	nl	LS	LS-CV	%imp.	p-value
n=25	**0.1**	0.06	0.04	20.3%	*
	0.2	0.28	0.18	36.1%	*
	0.3	0.83	0.43	48.3%	**
	0.5	2.37	0.94	60.6%	**
n=50	**0.1**	0.017	0.016	9.32%	**
	0.2	0.09	0.06	30.31%	*
	0.3	0.35	0.20	41.08%	*
	0.5	1.05	0.46	56.43%	**
n=100	**0.1**	0.009	0.008	7.9%	**
	0.2	0.04	0.03	23.3%	*
	0.3	0.12	0.09	30.0%	*
	0.5	0.31	0.17	43.9%	*

For both methods, the MSE decreases as expected with increasing number of datapoints since more information is available to train the kinetic model. Although LS-CV is consistently more accurate than LS in predicting true kinetics, the relative improvement is more pronounced on limited and more noisy data since LS is prone to overfitting. In LS-CV, this tendency is countered by the fact that the training folds with higher noise will have a relatively larger validation error and hence will be weighted low in the final kinetic parameter value. LS-CV is therefore exceptionally robust against experimental noise. Further comparison of the estimated parameters from these methods shows that LS-CV consistently matches the absolute values of real parameters better compared to LS.

In practice, the "true kinetics" are of course not available, and the goodness of the fit hence needs to be tested against the experimental test data, i.e., the hold-out from the original data set. This data will have the same noise level as the training data (since it is part of the same experimental data set). To mimic this, MSE values of the same runs are also calculated against noisy test set as a real-life representative metric, where synthetic (non-noisy) data do not exist. Consistent with the above discussed findings, the relative improvement of LS-CV decreases with increasing dataset size for the same noise level, and larger datasets are more tolerant to noise. However, while LS-CV significantly improves the prediction accuracy of true kinetics, it predicts noisy test data only marginally better than simple LS (Table 7). Remarkably, a "naïve observer" would hence rate both methods (almost) equally competent in deriving accurate kinetic parameters, while in fact LS-CV was able to unveil the true kinetics underlying the noisy data with significantly improved accuracy as shown above.

Table 7 Kinetic accuracy (noisy test MSE) comparison of LS and LS-CV methods with all dataset size and noise level combinations (p-value codes: *<0.005, **<0.05)

Noisy test MSE	**n=25**			**n=50**			**n=100**		
nl	**LS**	**LS-CV**	**p-val.**	**LS**	**LS-CV**	**p-val.**	**LS**	**LS-CV**	**p-val.**
0.1	1.75	1.74	**	1.73	1.73	*	1.90	1.90	**
0.2	7.16	7.07	**	7.93	7.87	*	7.88	7.86	*
0.3	15.90	15.49	**	14.19	13.97	*	13.17	13.11	**
0.5	44.77	41.94	*	38.96	37.48	**	28.31	27.81	**

Beyond noise, experimental data, and in particular data from industrial operations, is often subject to outliers, i.e. “bad” data with errors above the general experimental noise level which can be caused by operator error, temporary malfunctioning of sensor, or similar unpredictable effects. To evaluate the ability of LS-CV and LS to handle such outliers, their effect is investigated by progressively increasing the number of outliers in the data. In order to reliably assess the method performances against outliers, they are only added to the training data. For all outlier analyses, the same dataset is used for direct comparison (n:50, nl:0.2). Outliers are generated by either adding or subtracting one standard deviation of the variable value to the noise-added training data. The MSE against the “true kinetics” test set are tabulated in Table 8. Clearly and unsurprisingly, LS fitting becomes significantly worse at predicting true kinetics with increasing number of outliers. The accuracy of the LS-CV prediction also decreases with more outliers, although the adverse effect is significantly lower compared to LS. Similar to its handling of noise, LS-CV can effectively filter out outliers via statistical averaging.

Table 8 Effect of outliers in training data on the kinetic accuracy (test set MSE) comparison of LS and LS-CV methods (p-value codes: *<0.0001, **<0.01)

	n=50 nl= 0.2 no outliers - training				**n=50, noise nl = 0.2 2 outliers - training**			
	LS	**LS-CV**	**%imp.**	**p-val.**	**LS**	**LS-CV**	**%imp.**	**p-val.**
true MSE	0.091	0.064	30%	*	0.115	0.066	42%	*
	n=50 noise nl = 0.2 5 outliers - training				**n=50, noise nl = 0.2 10 outliers - training**			
	LS	**LS-CV**	**%imp.**	**p-val.**	**LS**	**LS-CV**	**%imp.**	**p-val.**
true MSE	0.290	0.092	67%	*	0.953	0.265	72%	**

Table 9 Effect of outliers in test data on the comparison of LS and LS-CV methods

	n=50 nl= 0.2 no outlier			**n=50, nl= 0.2 5 outliers - training**			**n=50, nl= 0.2 5 outliers - test**		
	LS	**LS-CV**	**%imp.**	**LS**	**LS-CV**	**%imp.**	**LS**	**LS-CV**	**%imp.**
noisy test MSE	7.93	7.87	0.76%	8.79	8.12	8%	26.53	26.53	0.015%

Note that addition of outliers to the test dataset will throw off any fitting method, unless data is preprocessed with existing outlier filtering tools. A separate run, in which five outliers are added only to the noisy test dataset, shows no significant improvement between LS and LS-CV methods, as shown in Table 9. In this case, the model is trained with comparatively good data and then its “accuracy” is tested again bad data, which is of course inherently doomed since the measure of accuracy is fundamentally flawed. This simple “sanity test” highlights the importance of sampling when using real-life experimental test dataset for model validation purposes: Great care should be taken to assure that any test data is as free of outliers as possible since the calculated accuracy of the fitting may otherwise result in wrong interpretation of the results. While here the “flawed” test data (i.e. test data with outliers) was kept artificially constant, CV methods will minimize the danger of this occurring, due to the partition of dataset into folds and repeated estimations based on all permutations of these folds. This assures a sampling of data in a way that is more resistant to the presence of outliers since only a subset of the runs will contain outliers in the test data (as illustrated further above).

4.4 Conclusion

Precise knowledge of chemical reaction kinetics is fundamental for rapid exploration of the reaction outcome over a wide range of operating conditions, reactor design, and process safety. However, in industrial practice, the availability of data available for identification of kinetic parameters is often limited since acquisition of data is time-consuming, expensive, and/or challenging. This is further exacerbated by the fact that the quality of available data can be compromised by noise and the presence of outliers. Furthermore, derived kinetic parameters are rarely tested/validated against overfit, which may result in wrong interpretation of kinetics outside known operating conditions.

In this work, a straightforward proof-of-concept study is employed to investigate robust kinetic parameter estimation with limited data availability. In an attempt to minimize model overfit, cross-validation (CV) methodology is implemented to simple, conventional nonlinear least-squares fitting. This method is widely used to assess the accuracy of machine learning classifiers, although a similar implementation of the same strategy to parametric regression problems could also allow robust derivation of reaction kinetics. This method was furthermore comparatively evaluated against two stochastic methods, Markov chain Monte Carlo and genetic algorithm, using synthetic data with varying level of data set size and noise levels. A simple one-step kinetic model, loosely based on previously published reaction kinetics for the catalytic water-gas shift reaction, is used for the investigation. Prior to parameter estimation, the model is evaluated to confirm that kinetic parameters are identifiable and model outcomes are sensitive to all parameters within the studied variable range.

As expected, the analysis of the results shows that although LS is the fastest method, it is overall the least accurate method in predicting true kinetics. While GA and MCMC are found to be effective for larger data set sizes, both methods tend to overfit to noise when data availability is limited. LS-CV, on the other hand, strongly outperforms these methods when high noise level is present in the training data. In addition, regardless of the dataset properties, LS-CV requires significantly fewer objective function evaluations compared to stochastic methods, i.e. its computational efficiency is significantly higher. Finally, while GA and MCMC both require sufficiently sophisticated operators, i.e. they require significant experience in tuning computational parameters to achieve robust progress in the stochastic calculations, LS-CV is a rather straightforward extension of the well-established nonlinear least-squares (LS) approach implemented in virtually all numerical software packages as well as process simulation and optimization tools.

A more detailed comparison between LS-CV and LS confirms that the former is consistently more accurate in predicting true kinetics, more notably for limited data. Similar to noise, LS-CV is also found to be effective in filtering out outliers in the training data due to the use of repeated estimations on random partitions of the dataset which are then averaged weighted on their respective MSE. The randomized partition of CV also allows the data to be sampled more homogeneously and make use of the entire available data set, which is critical for accurate model validation in particular for limited data availability. In the present work, the analysis was performed on a simple one-step model reaction. While we expect the results to hold for systems with higher dimensionality, systematic extension onto more complex models is needed to validate this expectation.

Overall, our study indicates that the implementation of a cross-validation routine with nonlinear least-squares fitting can provide a robust, easy-to-use, and highly efficient approach to parameter estimation and regression problems in the face of restricted and/or noisy data, and hence constitutes a valuable tool for researchers and practitioners alike.

5.0 Summary and Outlook

5.1 Oxidative Coupling of Methane

In Chapter 2.0, oxidative coupling of methane (OCM) reaction was experimentally investigated as a promising route for methane upgrading to value-added chemicals. To this end, the OCM reaction was revisited on Mn-Na_2WO_4/MgO – one of the most effective catalysts for this reaction to-date – to gain insights into methane activation and reaction pathways leading to high C_2 selectivity. The catalytic reactivity tests were conducted in the absence of molecular oxygen in the feed, which enabled us to observe surface-initiated reaction pathways that are not readily visible otherwise. Supported single component MnO_2 and Na_2WO_4 catalysts were also studied via thermogravimetric and fixed-bed reactor studies to determine their baseline methane activity and C_2 selectivity. Both individual metal oxides showed poor OCM performance at 900°C. Na_2WO_4 was completely inactive towards methane activation, while manganese oxide favored unselective total oxidation followed by rapid catalyst deactivation via coking. On the other hand, the use of Mn-Na_2WO_4 mixed oxide catalyst (MOC) decreased the cumulative CO_2 production by 30% and yields a 10-fold increase in C_2 production, resulting in a steep increase in C_2 selectivity to 69% at 900°C. Furthermore, the synergistic effect and lattice oxygen sharing mechanism between MnO_2 and Na_2WO_4 was examined by physically mixing individually synthesized samples of these two metal oxides which, remarkably, showed the identical performance to conventional mixed oxide catalyst in terms of both CH_4 activity and C_2 selectivity. Additional unsteady state kinetic and XRD analyses suggested that while the presence of Mn-oxide is critical for methane activity, the gas phase dehydrogenation of ethane s the key step to form ethylene. Selective hydrogen removal on tungstate was found to promote higher C_2 yields, providing a new direction for rational catalyst design where metal oxide components of the catalyst could be individually optimized towards different functions. However, recent in situ characterization studies of the surface revealed that Na_2WO_4 promoter melts at temperatures above 700°C, which could increase its mobility at reaction temperatures and wet adjacent Mn oxide particles, removing or reducing the “physical separation” introduced by the physically mixed catalyst. To test the direct influence of surface wetting on the metal oxide interactions at high temperatures, a series of in-situ environmental TEM (E-TEM) experiments with elemental mapping on physical mixture catalyst is proposed in the next section.

5.1.1 Future Work

To investigate the physical behavior of the catalyst, the following E-TEM experiments will be conducted. Initially, the elemental distribution of the catalyst will be characterized via spatially resolved EDX or EELS scan for the “as prepared” Mn-Na_2WO_4 physical mixture catalyst (PMC) at room temperature. Following the identification of areas that show well-positioned adjacent MnO_2 and Na_2WO_4 particles, the sample will be heated up to temperatures above 800°C while observing the catalyst structure in TEM. At the high temperature, another elemental mapping will be conducted to capture the melting and spreading process. Lastly, the sample will be cooled down to room temperature and re-mapped again to see whether de-wetting occurs during the cool-down, recovering a physically well separated mixture. These experiments would enable us to gain a much better understanding of the synergistic interaction between Na_2WO_4 and MnO_x at reaction conditions, which is key for rational catalyst design.

5.2 Design and Optimization of Chemical Reactors

In Chapter 3.0, another value-added chemical that can be synthesized through methane upgrading, methyl mercaptan or methanethiol (CH_3SH, MeSH) was investigated, which is the building block of an essential amino acid, methionine. Towards this goal, we performed precise model-based development of optimal catalytic reactors for methanethiol production. The computational work consisted of the derivation robust kinetic parameters for the production of methanethiol, development of reactor models, and subsequent optimization to determine optimum operating conditions and reactor design for a large-scale process. Due to the limited number of experimental data points available, a statistical kinetic fitting methodology combining nonlinear least-squares fitting with cross-validation was implemented to improve the robustness of the derived kinetics. This approach was found to significantly increase the predictive ability of the model on unseen experimental datapoints. By performing model reduction based on local sensitivity analysis of derived parameters, a thermodynamically consistent kinetic parameter set was obtained to describe both MeOH reactor and DMS cleavage reactor kinetics.

Next, two-dimensional pseudo-homogeneous reactor models were built to accurately simulate the large-scale production of methanethiol. Conservation of mass, energy and momentum equations describing the behavior of the system were derived, including modules for estimating temperature dependent thermophysical and transport properties of the gaseous species in the reactor. These mathematical models were subsequently used to determine the operating conditions and reactor design to maximize methanethiol yields. Optimal process conditions and reactor specifications for standalone reactors as well as reactor combinations were determined considering both adiabatic and polytropic operation. Through the optimization of both reactor geometry and product yield, up to~4-fold improvement in MeSH productivity and ~20% improvement in MeSH selectivity from base conditions was attainable with minimal pressure drop. Suppressed formation of side products also allowed a steep reduction in reactor volume (by 75%) and the number of tubes (by an order of magnitude) through optimization of the secondary reactor. The polytropic operation for the MeOH reactor was also investigated, and various design strategies were investigated to improve cooling and reduce the peak temperatures. However, due to high flowrates, optimization through diameter reduction and catalyst bed dilution still resulted in a minimum of ~35℃ temperature rise in a conventional tubular reactor. For the polytropic operation to be feasible, it appears that the reactor should be run at a lower capacity, and/or the number of tubes should be increased up to ~30000. Alternatively, process intensification strategies, such as a spinning disc reactor, could be explored to potentially improve cooling through dramatically increasing surface-area-to-volume ratio.

Overall, in this work, a rigorous computational framework for modeling and optimization of chemical reactors was showcased for a large-volume industrial process. The mathematical models constructed here are easily adaptable towards reactor design and optimization of other homogeneous or pseudo-homogeneous reaction systems. Furthermore, for heterogeneous systems, the reactor models could be expanded to include appropriate concentration gradients to account for mass transfer limitations inside and/or outside catalyst particles, if needed.

The kinetic and reactor model constructed does not consider catalyst deactivation since the required experimental data for long-term catalyst stability was unavailable. However, a time-dependent term describing catalyst deactivation could be added to the models. Moreover, additional optimizations could be performed in which the catalyst deactivation data is used as a constraint to minimize or prevent reactor downtime.

5.3 Robust Kinetic Parameter Estimation of Chemical Reactors

In Chapter 4.0, motivated by the results of the kinetic modeling work of Chapter 3.0., a straightforward proof-of-concept study was employed to compare different algorithms/methods for robust kinetic parameter estimation with limited data availability. Accurate determination of reaction kinetics is fundamental for rapid exploration of the reaction outcome over a wide range of operating conditions. However, in industry practice, the number of data points available for kinetics derivations is often very limited. Furthermore, kinetic parameters obtained are rarely tested and validated against a possible overfit, which may result in a wrong interpretation of kinetics. As a potential mitigation strategy for this problem, cross-validation methodology was implemented to kinetic parameter regression (LS-CV) and compared to regular non-linear least squares (LS), Markov chain Monte Carlo (MCMC), and genetic algorithm (GA). The analyses were performed on synthetic reactivity data to probe dataset size (number of experimental points), noise level, and number of outliers, and the performance of the different algorithms were compared in terms of accuracy (closeness to true reaction kinetics) and efficiency (computational cost). P-values were also calculated to assure statistical significance of the results. Overall, the LS-CV method was found to be the most efficient in filtering out the noise and outliers present in limited data due to the statistical averaging of repeated estimations on different partitions of the dataset. In addition, LS-CV required a significantly smaller number of objective function evaluations compared to stochastic methods, MCMC, and GA. Although LS was the fastest, it was overall the least successful method in predicting true kinetics. On the other hand, CV implementation to LS appears to yield a robust approach towards kinetic parameter estimation.

As a starting point, a simple reaction of type “A + B = C + D” was used a model reaction. However, the parameter estimation study employed here could be expanded to a kinetic model with higher complexity, such as a multistep reaction mechanism that includes a combination of parallel and series reaction steps. Least-squares based methods are more prone to get stuck on local minima with increased model complexity, whereas stochastic methods such as MCMC and GA can be expected to be much more effective in predicting true kinetics. It would be of interest to validate whether the simple LS-CV approach would still outperform the more advanced MCMC and GA methods in this case. If not, a similar CV implementation strategy may be applied to these stochastic methods to allow model validation and minimize overfit.

In parallel, to provide more generalized guidelines for the use of the proposed CV strategy, a detailed hyperparameter tuning study could be carried out, which are configuration parameters that are algorithm or method specific. For instance, the number of folds, weight function of the folds, and the number of repeated estimations may be considered as the hyperparameters of the LS-CV method. Effect of these hyperparameters could be investigated and fine-tuned based on the dataset properties such as size and experimental noise. Such investigations would further improve our understanding of the general applicability of the LS-CV method.

Appendix A Kinetic Investigations on the Role of Sodium Tungstate Promoter in Mn_xO_y-Na_2WO_4 Catalyzed Oxidative Methane Coupling Reaction

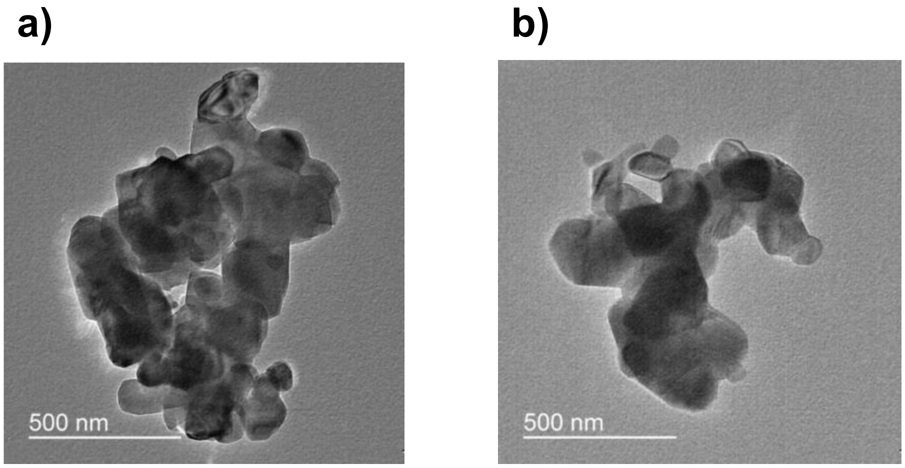

Appendix Figure 1 TEM images of A) Mn-Na_2WO_4/MgO MOC B) Mn/MgO fresh catalysts

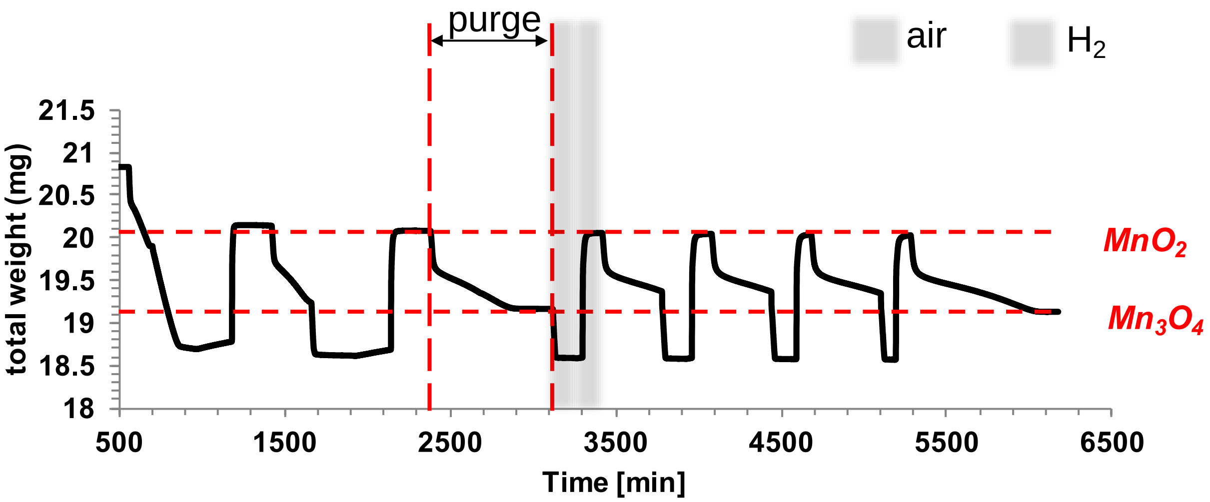

Appendix Figure 2 Thermogravimetric analysis of Mn-Na_2WO_4/MgO MOC at 900°C. The weight loss under inert flow indicated by dashed lines occur due to thermal instability of MnO_2 at high temperatures (>500°C). Oxygen loss rate during purge period at reaction temperature is quantified and used for accurate oxygen material balance calculation.

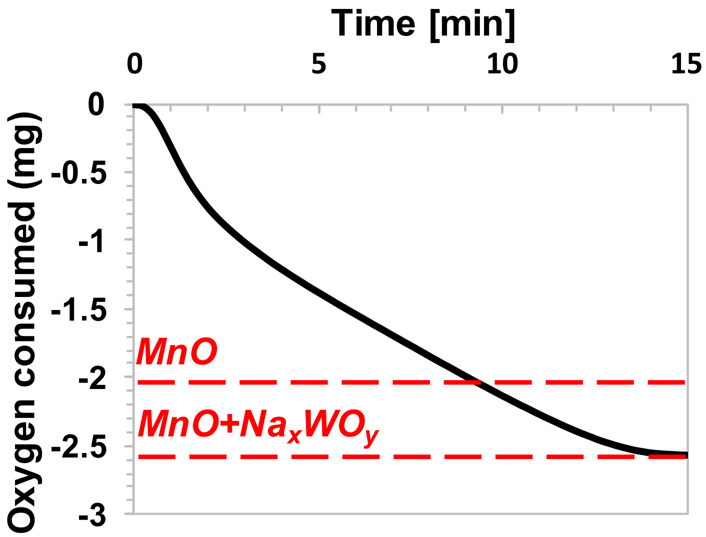

Appendix Figure 3 Temporal total lattice oxygen consumption of Mn-Na_2WO_4/MgO MOC during reduction, quantified by material balance calculations. Top dashed line marks the oxygen consumption when MnO_2 completely reduces to MnO. Residual lattice oxygen loss (bottom dashed line) is observed due to selective H_2 removal occurring on Na_2WO_4.

Appendix B Derivation of Model Equations

Mass Balance

In plug flow reactors, composition of the fluid varies along the flow path. The material balance for a reaction component must be made from a differential volume element. The mole balance equations hence are derived using the flux balance in an infinitesimal cylindrical shell.

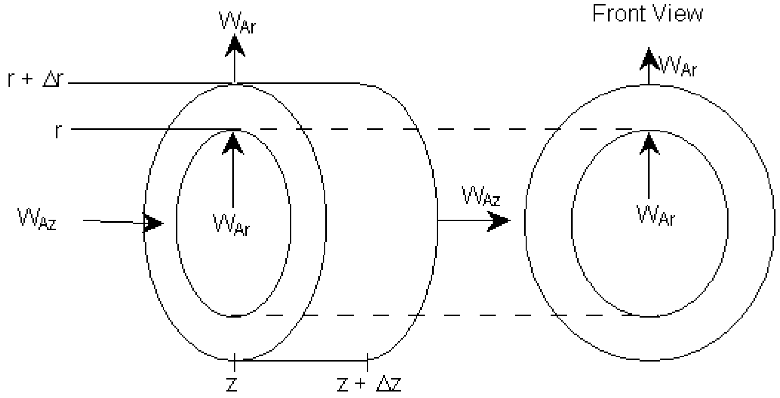

Appendix Figure 4 Cylindirical shell of thickness Δr and Δz[102]

Flux terms are denoted as W_A and calculated as the combination of diffusion and bulk flow in axial and radial directions:

$$W_{Az} = -D_e \frac{\partial C_A}{\partial z} + U_z C_A \tag{B-1}$$

$$W_{Ar} = -D_e \frac{\partial C_A}{\partial r} + U_r C_A \tag{B-2}$$

where D_e denotes the diffusion coefficient and the U is the linear velocity in either axial or radial direction. The total molar flowrates are estimated via the following equations:

$$\begin{pmatrix} Moles\ In \\ at\ r \end{pmatrix} = W_{Ar} \begin{pmatrix} cross\ sectional\ area \\ normal\ to\ radial\ flux \end{pmatrix} = W_{Ar} 2\pi r \Delta \tag{B-3}$$

$$\binom{Moles\ In}{at\ z} = W_{Az}\binom{cross\ sectional\ area}{normal\ to\ axial\ flux} = W_{Az}2\pi r\Delta r \tag{B-4}$$

where r is the radial distance from the center, and Δr and Δz are radial and axial thickness of the cylindrical shell. From these equations, the mole balance is constructed as following:

$$\binom{Moles\ in}{at\ r} - \binom{Moles\ out}{at\ r+\Delta r} + \binom{Moles\ in}{at\ z} - \binom{Moles\ out}{at\ z+\Delta z} + Generation \\ = 0\ (Accum.) \tag{B-5}$$

By substituting accumulation and generation terms in the mole balance equation, the following equation is obtained:

$$\Delta W_{Az}2\pi r\Delta z|_r - \Delta W_{Az}2\pi r\Delta z|_{r+\Delta r} + \Delta W_{Ar}2\pi r\Delta r|_r - \Delta W_{Ar}2\pi r\Delta r|_{r+\Delta r} \\ + r_A 2\pi r\Delta r\Delta z = \frac{\partial C_A(2\pi r\Delta r\Delta z)}{\partial t} \tag{B-6}$$

Both sides or the equations are divided by the volume of the shell ($2\pi r\Delta r\Delta z$) and the mole balance equation is reduced to:

$$-\frac{1}{r}\frac{\partial(rW_{Ar})}{\partial r} - \frac{\partial W_{Az}}{\partial z} + r_A = \frac{\partial C_A}{\partial t} \tag{B-7}$$

Substituting the flux terms and removing time derivative due to modeling at steady state, the mole balance equation is reduced to:

$$-\frac{1}{r}\frac{\partial}{\partial r}\left[\left(-D_e\frac{\partial C_i}{\partial r}r\right) + U_r C_i\right] - \frac{\partial}{\partial z}\left[-D_e\frac{\partial C_i}{\partial z} + U_z C_i\right] + r_i = 0 \tag{B-8}$$

Since the diffusivity of gases are relatively high, the radial concentration gradient assumed to be 0 ($\frac{\partial C_i}{\partial r} = 0$). Velocity profile of the gas in the axial direction is also assumed constant ($U_z = constant$). For long enough reactors (L/d>>20), axial dispersion can be neglected, since the difference in concentration approaches zero[154]. The majority of the gas transport occurs in the bulk form due to fluid flow, in which diffusion term would be significantly small[155]. Based on these assumptions, the second order concentration derivative in axial direction can be neglected ($D_e \frac{\partial^2 c_i}{\partial z^2}$ = 0). Hence, the final mole balance equation becomes:

$$-U_z \frac{\partial C_i}{\partial z} + r_i = 0 \ or \ -\frac{dC_i}{dz} + \frac{A_{cs}}{\nu_0} r_j = 0 \tag{B-9}$$

$$\text{where } U_z = \frac{\nu_0}{A_{cs}}$$

Energy Balance

Similar to the mass balance, the energy balance is also derived on an infinitesimal cylindrical shell with energy fluxes denoted by e. Energy flux is composed of a conduction and a convection part:

$$e = q + \sum W_i H_i \tag{B-10}$$

The first term on right hand-side of the equation is the conduction term, q, which is calculated using Fourier's law. The second term is the convection term, which is calculated from the molar flux (W) and the enthalpy (H). The Fourier's law is given as:

$$q_z = -\lambda_e \frac{\partial T}{\partial z} \tag{B-11}$$

where λ_e is the bed thermal conductivity (W/mK). The overall energy balance is determined by energy entering and leaving the shell:

$$\begin{pmatrix} Energy\ Flow \\ in\ at\ r \end{pmatrix} - \begin{pmatrix} Energy\ Flow \\ out\ at\ r + \Delta r \end{pmatrix} + \begin{pmatrix} Energy\ Flow \\ in\ at\ z \end{pmatrix} - \begin{pmatrix} Energy\ Flow \\ out\ at\ z + \Delta z \end{pmatrix} = 0\ (Accum.) \tag{B-12}$$

$$e_r 2\pi r\Delta z|_r - e_r 2\pi r\Delta z|_{r+\Delta r} + e_z 2\pi r\Delta r|_z - e_z 2\pi r\Delta r|_{z+\Delta z} = \frac{\partial \sum H_i C_i (2\pi\Delta r\Delta z)}{\partial t} \qquad \text{(B-13)}$$

The accumulation term on the right-hand side is zero since the model is built for steady state analysis of the system. The left-hand side of the equation is divided by the volume of the cylindrical shell ($2\pi\Delta r\Delta z$), and following equation is obtained:

$$-\frac{1}{r}\frac{\partial(re_r)}{\partial r} - \frac{\partial e_z}{\partial z} = 0 \qquad \text{(B-14)}$$

By substituting the energy flux term with Fourier's law and the convection terms, the energy balance becomes:

$$-\frac{1}{r}\frac{\partial r[q_r + \sum W_{ir}H_i]}{\partial r} - \frac{\partial[q_z + \sum W_{iz}H_i]}{\partial z} = 0 \qquad \text{(B-15)}$$

The derivative of bulk energy flow can be defined as the following:

$$\frac{\partial \sum W_{iz}H_i}{\partial z} = \sum H_i \frac{\partial W_{iz}}{\partial z} + \sum W_{iz}\frac{\partial H_i}{\partial z} \qquad \text{(B-16)}$$

By substituting the equation above into the energy balance, the overall energy balance becomes:

$$-\frac{1}{r}\frac{\partial(rq_r)}{\partial r} - \frac{\partial q_z}{\partial z} - \sum H_i\left(\frac{1}{r}\frac{\partial rW_{ir}}{\partial r} + \frac{\partial W_{iz}}{\partial z}\right) - \sum W_{ir}\frac{\partial rH_i}{r\partial r} - \sum W_{iz}\frac{\partial H_i}{\partial z} = 0 \qquad \text{(B-17)}$$

Next mole balance equation is recalled and substituted into energy balance:

$$-\frac{1}{r}\frac{\partial(rW_{ir})}{\partial r} - \frac{\partial W_{iz}}{\partial z} + r_i = 0 \qquad \text{(B-18)}$$

$$-\frac{1}{r}\frac{\partial(rq_r)}{\partial r} - \frac{\partial q_z}{\partial z} + \sum H_i r_i - \sum W_{ir}\frac{\partial rH_i}{r\partial r} - \sum W_{iz}\frac{\partial H_i}{\partial z} = 0 \qquad \text{(B-19)}$$

The enthalpy of reaction is defined as:

$$\sum H_i r_i = -\sum \nu_i H_i(-r_A) = \Delta H_{Rx} r_A \tag{B-20}$$

where $r_A = r_i \rho_c$. The derivatives of enthalpy could be defined in terms of heat capacity using the following equation:

$$\frac{\partial H_i}{\partial z} = C_{pi}\frac{\partial T}{\partial z} \tag{B-21}$$

After substituting the enthalpy of reaction, derivatives of enthalpies and the conduction term with Fourier's law, the final form of the energy balance equation becomes:

$$\frac{\lambda_e}{r}\left(\frac{\partial\left(r\frac{\partial T}{\partial r}\right)}{\partial r}\right) + \lambda_e\frac{\partial^2 T}{\partial z^2} + \Delta H_{Rx} r_i \rho_c - \left(\sum W_{ir} C_{Pi}\right)\frac{\partial T}{\partial r} - \left(\sum W_{iz} C_{Pi}\right)\frac{\partial T}{\partial z} = 0 \tag{B-22}$$

Using the similar assumption due to the high diffusivity of gas species, the radial flux term neglected ($W_{ir} = 0$). Similarly, since axial dispersion is neglected (L/d>20), the energy balance becomes:

$$\frac{\lambda_e}{r}\left(\frac{\partial\left(r\frac{\partial T}{\partial r}\right)}{\partial r}\right) + \lambda_e\frac{\partial^2 T}{\partial z^2} + \Delta H_{Rx} r_i \rho_c - \left(U\sum C_i C_{Pi}\right)\frac{\partial T}{\partial z} = 0 \tag{B-23}$$

Appendix C Model Assumptions and Validations

Fixed-bed catalytic reactors could either be modeled as pseudo-homogeneous or heterogeneous. In pseudo-homogeneous reactor models, only concentration and temperature gradients of the fluid transport is considered. In heterogeneous reactor models, concentration gradients between the bulk fluid and the external surface of the particles and/or within the pores of the particles are also modeled. Homogeneity conditions should be checked prior construction of mass balance equations. If said gradients are significant, they reduce, or limit, the rate of reaction.

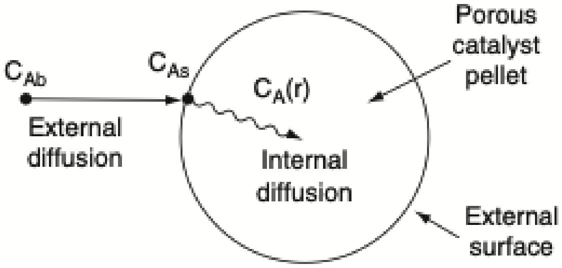

Appendix Figure 5 Mass transfer in a reaction[102]

In this thesis, the reactors are modeled as pseudo-homogeneous since mass transfer limitations are calculated based on the experimental data and found to be negligibly small. Two correlations are used to determine internal and external diffusion limitations of the model, namely Mears and Weisz-Prater criterion. Mears criterion determines if external mass transfer from the bulk gas phase to the catalyst surface can be neglected with the following equation:

$$MR = \frac{-r_{A,obs}\rho_b R n}{k_c C_{Ab}} \tag{C-1}$$

where $r_{a,obs}$ is the observed rate of reaction, kmol/kg-cat/s, R is the radius of the catalyst particles, m, ρ_b is the bulk catalyst density, kg/m^3, n is the reaction order, k_c is the mass transfer coefficient, m/s, C_{Ab} is the concentration of gas at the bulk, mol/dm^3. If the MR is less than 0.15, the external mass transfer effects could be neglected. The second correlation for the internal diffusion is Weisz-Prater criterion, which determines if mass transfer limitations inside catalysts particles exists:

$$C_{WP} = \frac{-r_{A,obs} R^2 \rho_c}{D_e C_{As}} \tag{C-2}$$

where $r_{a,obs}$ is the observed rate of reaction, R is the radius of the catalyst particles, ρ_c is the catalyst density, D_e is the effective diffusivity of gas molecules, C_{As} is the concentration of the gas at the particle surface. If there is no external diffusion limitation, C_{As} is equal to C_{Ab}, bulk concentration. If calculated C_{WP} is at least two order of magnitude smaller than the unity (<<1), the internal mass transfer limitations within the catalyst could be neglected. Since both of these numbers are below the provided thresholds for the methanol thiolation system studied here, the reactor is accurately designed as a pseudo-homogeneous reactor.

Appendix D Numerical Methods

The energy, mass and momentum balance equations are constructed as a set of partial differential equations (PDEs). Although final versions of the mole momentum balance equations reduced to ordinary differential equations (ODEs), the energy balance equations still have both radial and axial component. In general, the PDE solvers are less efficient and could lead to stability issues during integration. Therefore in this work, PDEs are transformed into ODEs using method of lines (MOL) method. The MOL method converts the PDE into ODE by discretizing one of the independent variables using finite difference methods (Figure D1)

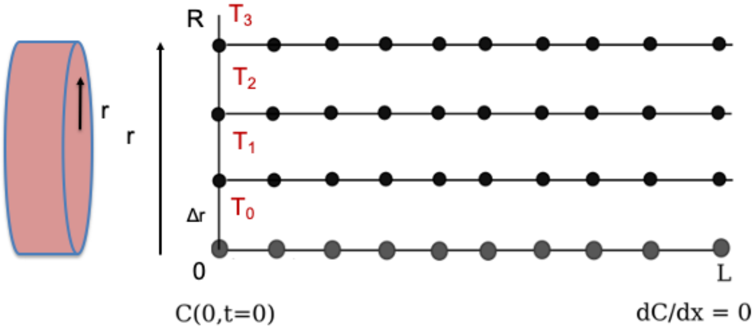

Appendix Figure 6 Schematic description of method of lines

Using finite difference method, the temperature variable is discretized in radial axis. Finite number of temperature nodes (T_0, T_1,..T_N) which are function of z (axial length) are obtained. N is chosen as 6 in this study. The relationships between the temperature nodes are defined with forward, backward and central finite difference equations:

$$\frac{\partial^2 T_i}{\partial r^2} = \frac{T_{i+1} - T_i + T_{i-1}}{\Delta r^2} \; if \; i = 2,3,..,N-1 \tag{D-1}$$

$$\frac{\partial T_i}{\partial r} = \frac{T_{i+1} - T_{i-1}}{2\Delta r} if\ i = 2,3,..,N-1 \tag{D-2}$$

$$\frac{\partial T_i}{\partial r} = \frac{T_{i+1} - T_i}{\Delta r} if\ i = N \tag{D-3}$$

$$\frac{\partial T_i}{\partial r} = \frac{T_i - T_{i-1}}{\Delta r}\ if\ i = 1 \tag{D-4}$$

The constructed set of ODE's are integrated using Ode15s, a built-in function in MATLAB, which is a variable-step and variable-order solver that utilizes numerical differential formulas up to order of 5.

Appendix E Physical Property Correlations

The temperature changes inside the reactor requires thermophysical properties to be estimated within the model. For this purpose, a set of empirical correlations are used to calculate the density, heat capacity, viscosity and thermal conductivity values.

The density is calculated based on the Peng-Robinson (PR)[94] equation of state. Initially, for each species, the pure component parameters are estimated for PR using the following formulas[96]:

$$m_i = 0.37464 + 1.54226\,\omega_i - 0.26992{\omega_i}^2 \tag{E-1}$$

$$\alpha_i = \left(1 + m_i\left(1 - {T_R}^{0.5}\right)\right)^2 \tag{E-2}$$

$$a_i = \alpha_i\, 0.45724\, R^2 \frac{{T_{ci}}^2}{P_{ci}} \tag{E-3}$$

$$b_i = 0.07780\, R \frac{T_{ci}}{P_{ci}} \tag{E-4}$$

where ω_i is acentric factor, T_R is reduced temperature, T_{ci} and P_{ci} are the critical temperatures and pressures of species i in K and bar, respectively. Next, the PR parameters for the mixture are evaluated using the following equations:

$$a_{mixture} = \sum_i \sum_j y_i y_j \sqrt{a_i a_j}\left(1 - k_{ij}\right) \tag{E-5}$$

$$b_{mixture} = \sum_i y_i b_i \tag{E-6}$$

where y_i is the gas phase mole fraction and the k_{ij} is the mixture parameter for PR equation of state. After calculating mixture PR parameters, the following equation is solved for molar volume $\bar{v}$.

$$P = \frac{RT}{(\bar{v} - b_{mixture})} - \frac{a_{mixture}}{\left(\bar{v}(\bar{v} + b_{mixture}) + b_{mixture}(\bar{v} - b_{mixture})\right)} \tag{E-7}$$

where P is the pressure in bar and T is the temperature in K. The resulting molar volume is converted to density using molecular weight of mixture.

$$\rho = \frac{mw_{mixture}}{\bar{v}} \tag{E-8}$$

Appendix Table 1 Physical properties for individual species

Species	MW(g/gmol)	Pc(bar)	Tc(K)	ω
CH_4	16	46.17	190.63	0.01
CO_2	44	73.76	304.15	0.23
CS_2	76	79	552	0.11
DMDS	94	53.6	615	0.2
DME	46	53.7	400.1	0.2
DMS	62	55.3	503.04	0.19
H_2	2	20.47	43.6	0
H_2O	18	221.19	647.35	0.35
H_2S	34	90.07	373.55	0.1
MeOH	32	80.96	512.58	0.56
MeSH	48	72.3	469.95	0.16

Compressibility factor, which will be used for heat capacity calculation, can also be calculated with the same molar volume variable using the following formula:

$$Z = \frac{P\bar{v}}{RT} \tag{E-9}$$

The list of physical property values and mixing parameters that are necessary for the density calculation are taken from Aspen properties database and are given in Appendix Table 1 and 2, respectively.

Appendix Table 2 Mixing parameters for PR equation of state

k_{ij}	CH_4	CO_2	CS	DMDS	DME	DMS	H_2	H_2O	H_2S	MeOH	MeSH
CH_4	0	0.091	0	0	0	0	0.015	0	0	0	0
CO_2	0.091	0	0	0	0	0	-0.16	0.12	0.10	0.02	0
CS_2	0	0	0	0	0	0	0	0	0	0	0
DMDS	0	0	0	0	0	0	0	0	0	0	0
DME	0	0	0	0	0	0	0	0	0	0	0
DMS	0	0	0	0	0	0	0	0	0	0	0
H_2	0.015	-0.16	0	0	0	0	0	0	0	0	0
H_2O	0	0.12	0	0	0	0	0	0	0.04	-0.08	0
H_2S	0	0.10	0	0	0	0	0	0.04	0	0	0
MeOH	0	0.02	0	0	0	0	0	-0.08	0	0	0
MeSH	0	0	0	0	0	0	0	0	0	0	0

Similar to mixture density, mixture heat capacity is also calculated based on PR equation of state. The total heat capacity is composed of an ideal and a residual part. The ideal part is calculated using empirical correlation from Ali and Lee[156]:

$$c_{p,ig} = A_i + B_i \frac{C_i/_T}{\sinh C_i/_T{}^2} + D_i \frac{E_i/_T}{\cosh E_i/_T{}^2} \tag{E-10}$$

where A, B, C, D and E are the empirical constants from JANAF thermochemical tables[157,158], which are given in Appendix Table 3.

Appendix Table 3 Ideal heat capacity empirical constants

Species	A	B	C	D	E
CH_4	33298	79933	2086.9	41602	991.96
CO_2	29370	34540	1428	26400	588
CS_2	30100	33380	896	28930	374.7
DMDS	78430	143640	1583.6	87100	730.65
DME	57431	94494	895.51	65065	2467.4
DMS	60370	137470	1641	79880	743.5
H_2	27617	9560	2466	3760	567.6
H_2O	33363	26790	2610.5	8896	1169
H_2S	33288	26086	913.4	-17979	949.4
MeOH	39252	87900	1916.5	53654	896.7
MeSH	43697	50387	809.24	42223	2192.4

The residual enthalpy is calculated using similar mixture parameters[159]:

$$H^R = RT(Z-1) - \frac{\frac{\partial a_{mixture}}{\partial T}}{2\sqrt{2}b_{mixture}} log\left(\frac{\bar{v} + (\sqrt{2}+1)b_{mixture}}{\bar{v} + (-\sqrt{2}+1)b_{mixture}}\right) \tag{E-11}$$

The residual heat capacity c_p^R is calculated by taking the numerical derivative of the residual enthalpy H^R with respect to temperature. Finally, the mixture heat capacity is calculated from $c_p = c_{p,ig} + c_p^R$.

The viscosity calculation is divided into three parts. First, the pure component viscosity is calculated using DIPPR equation 102[95,96]:

$$\mu_{pure,i} = A_i \frac{T^{B_i}}{\left(1 + \frac{C_i}{T} + \frac{D_i}{T^2}\right)} \tag{E-12}$$

where A, B, C, D are the DIPPR constants for viscosity and T is the temperature in K. DIPPR constants for viscosity is given in Appendix Table 4.

Appendix Table 4 Empirical DIPPR constants for viscosity

Species	A	B	C	D
CH_4	5.25E-07	0.59006	105.67	0
CO_2	2.15E-06	0.46	290	0
CS_2	5.82E-08	0.9262	44.581	0
DMDS	3.23E-08	0.97742	0	0
DME	2.68E-06	0.3975	534	0
DMS	5.29E-07	0.6112	302.85	0
H_2	1.80E-07	0.685	-0.59	140
H_2O	1.71E-08	1.1146	0	0
H_2S	3.93E-08	1.0134	0	0
MeOH	3.07E-07	0.69655	205	0
MeSH	1.64E-07	0.76706	107.97	0

Secondly, after determining the pure component viscosities, the mixture viscosity is calculated using Chapman-Enskog-Brokaw correlation with Wilke mixing rule[96]:

$$\mu_{mixture,0} = \sum_i \frac{y_i \mu_{pure,i}}{y_i + \sum_j y_j \phi_{ij}} \tag{E-13}$$

$$\phi_{ij} = \sqrt{\mu_{pure,i}\mu_{pure,j}} A_{ij} S_{ij} \tag{E-14}$$

$$A_{ij} = m_{ij} \frac{1}{\sqrt{M_{ij}}} \left(1 + \frac{\left(M_{ij} - {M_{ij}}^{0.45}\right)}{2\left(1 + M_{ij}\right) + \frac{\left(1 + {M_{ij}}^{0.45}\right) m_{ij}}{1 + m_{ij}}} \right) \tag{E-15}$$

$$m_{ij} = \left(\frac{4}{\left(1 + \frac{1}{M_{ij}}\right)\left(1 + M_{ij}\right)} \right)^{0.25} \tag{E-16}$$

$$M_{ij} = \frac{mw_i}{mw_j} \tag{E-17}$$

$$S_{ij} = \begin{cases} \dfrac{1 + \sqrt{T_i^* T_j^*} + \dfrac{\delta_i \delta_j}{4}}{\sqrt{\left(1 + T_i^* + \dfrac{{\delta_i}^2}{4}\right)\left(1 + T_j^* + \dfrac{{\delta_j}^2}{4}\right)}}, \delta_i > 0.1, \delta_j > 0.1 \\ 1, \ elsewhere \end{cases} \tag{E-18}$$

$$T_i^* = \frac{T}{\epsilon_{k,i}} \tag{E-19}$$

$$\epsilon_{k,i} = 1.15\left(1 + 0.85\delta_i^2\right)T_{bi} \tag{E-20}$$

$$\delta_i = \frac{2{\mu_{Di}}^2}{V_{bi} T_{bi}} \tag{E-21}$$

where μ_{Di} is the dipole moment of species i in debyes, V_{bi} and T_{bi} are boiling molar volume and boiling temperature, respectively. Only other physical property used in viscosity calculations is the molecular weight. The boiling points and dipole moment are given in Appendix Table 5.

Appendix Table 5 Physical properties required for viscosity mixing rule

Species	μ_D	T_b	V_b
CH_4	0	111.66	0.0379694
CO_2	0	194.7	0.0350189
CS_2	0	319.375	0.062295
DMDS	1.98463	382.9	0.0980576
DME	1.3011	248.31	0.0630445
DMS	1.49896	310.48	0.074986
H_2	0	20.39	0.0285681
H_2O	1.84972	373.15	0.0188311
H_2S	0.968331	212.8	0.0358604
MeOH	1.69983	337.85	0.0427452
MeSH	1.51995	279.106	0.0542058

Lastly, Stiel-Thodos[96] correction for high pressure is taken into account for viscosity calculation:

$$\rho_r = \frac{V_c}{\bar{v}} \tag{E-22}$$

$$\mu_{mix} = \begin{cases} \mu_0 + 1.656\dfrac{\rho_r}{\xi}\ if\ \rho_r < 0.1 \\ \mu_{mixture,0} + 0.0607\ \dfrac{(9.045\rho_r + 0.63)^{1.739}}{\xi}\ if\ 0.1 < \rho_r < 0.9 \\ \mu_0 + \dfrac{e^{\left(4-e^{0.6439-0.1005\rho_r}\right)}}{\xi}\ if\ 0.9 < \rho_r < 2.2 \\ \mu_{mixture,0} + \dfrac{e^{\left(4-e^{0.6439-0.1005\rho_r-4.75\ 10^{-4}\left({\rho_r}^3-10.65\right)^2}\right)}}{\xi}\ if\ 2.2 < \rho_r < 2.6 \\ \mu_0 \end{cases} \tag{E-23}$$

$$\xi = \frac{T_c^{1/6}}{mw^{1/2} P_c^{2/3}} \tag{E-24}$$

Thermal conductivity is calculated using a combination of DIPPR equation 102[95] followed by a mixing rule correlation. The DIPPR equation for pure component viscosity is:

$$k_i = \frac{A_i T^{B_i}}{\left(1 + \frac{C_i}{T} + \frac{D_i}{T^2}\right)} \tag{E-25}$$

where A,B,C,D are the empirical thermal conductivity parameters and T is the temperature in K. Empirical DIPPR constants for thermal conductivity are given in Appendix Table 6.

Appendix Table 6 Empirical DIPPR constants for thermal conductivity

Species	A	B	C	D
CH_4	8.40E-06	1.4268	-49.654	0
CO_2	3.69	-0.3838	964	1860000
CS_2	0.0003467	0.7345	479	0
DMDS	0.00022578	0.892	697	0
DME	0.059975	0.2667	1018.6	1100000
DMS	0.00023614	0.9204	638	0
H_2	0.002653	0.7452	12	0
H_2O	6.20E-06	1.3973	0	0
H_2S	1.38E-07	1.8379	-352.09	46041
MeOH	5.80E-07	1.7862	0	0
MeSH	2.65E-05	1.1631	29.996	32519

For mixture thermal conductivity calculation, Wassiljewa-Mason-Saxena[97] correlation is used[96]:

$$k_{mixture} = \sum_i \frac{y_i k_i}{\sum_j y_j A_{ij}} \tag{E-26}$$

$$A_{ij} = \frac{\left(1 + \sqrt{\frac{\mu_i}{\mu_j}} + \sqrt[4]{\frac{mw_j}{mw_i}}\right)^2}{\sqrt{\left(1 + \frac{mw_i}{mw_j}\right)}} \tag{E-27}$$

The viscosity terms in the equation above are calculated as shown previously for the viscosity calculation.

Appendix F Derived Kinetic Parameters

Appendix Table 7 Derived kinetic parameters – all methods

Dataset	**Method**	**$k_{0,fwd}$**			**$k_{0,bwd}$**		
		mean	**min**	**max**	**mean**	**min**	**max**
n=100 nl=0.1	**LS**	3.22E+05	-	-	2.48E+08	-	-
	LS-CV	3.11E+05	2.96E+05	3.63E+05	2.60E+08	2.25E+08	2.92E+08
	MCMC	2.93E+05	2.64E+05	3.16E+05	3.11E+05	2.10E+08	2.70E+08
	GA	3.26E+05	2.20E+04	3.90E+05	2.60E+08	1.60E+08	3.32E+08
n=50 nl=0.2	**LS**	1.90E+05	-	-	2.05E+08	-	-
	LS-CV	2.13E+05	1.57E+05	3.07E+05	2.39E+08	1.50E+08	3.66E+08
	MCMC	2.11E+05	1.30E+05	3.90E+05	2.16E+08	1.00E+08	4.76E+08
	GA	2.25E+05	1.40E+05	3.70E+05	2.19E+08	1.12E+08	4.73E+08
n=25 nl=0.5	**LS**	1.15E+05	-	-	2.20E+08	-	-
	LS-CV	1.74E+05	1.00E+05	3.89E+05	2.61E+08	2.24E+07	4.18E+08
	MCMC	1.00E+05	7.25E+04	4.18E+05	2.11E+08	1.60E+07	3.80E+08
	GA	1.07E+05	3.01E+04	1.45E+05	2.36E+08	5.58E+06	1.11E+09

Dataset	**Method**	**$E_{a,fwd}$**		
		mean	**min**	**max**
n=100 nl=0.1	**LS**	5.02E+04	-	-
	LS-CV	5.03E+04	4.99E+04	5.07E+04
	MCMC	5.04E+04	5.00E+04	5.09E+04
	GA	5.03E+04	4.87E+04	5.11E+04
n=50 nl=0.2	**LS**	4.84E+04	-	-
	LS-CV	4.87E+04	4.76E+04	5.01E+04
	MCMC	4.87E+04	4.63E+04	5.04E+04
	GA	4.88E+04	4.72E+04	5.12E+04
n=25 nl=0.5	**LS**	4.52E+04	-	-
	LS-CV	4.75E+04	4.02E+04	5.35E+04
	MCMC	4.55E+04	3.73E+04	5.31E+04
	GA	4.58E+04	4.08E+04	4.81E+04

Appendix Table 8 Derived kinetic parameters – LS and LS-CV methods

Dataset		**Meth.**	$k_{0,fwd}$			$k_{0,bwd}$		
			mean	**min**	**max**	**mean**	**min**	**max**
n=100	**nl=0.1**	**LS**	2.86E+05	2.23E+05	3.24E+05	2.61E+08	2.19E+08	3.02E+08
		LS-CV	2.75E+05	2.10E+05	3.30E+05	2.42E+08	2.20E+08	3.17E+08
	nl=0.2	**LS**	2.49E+05	1.72E+05	3.16E+05	2.59E+08	1.78E+08	3.35E+08
		LS-CV	2.88E+05	2.02E+05	3.38E+05	2.78E+08	1.89E+08	3.42E+08
	nl=0.3	**LS**	2.37E+05	1.66E+05	3.29E+05	2.24E+08	1.37E+08	3.29E+08
		LS-CV	2.48E+05	1.73E+05	3.41E+05	2.57E+08	1.42E+08	3.61E+08
	nl=0.5	**LS**	1.77E+05	1.02E+05	3.21E+05	2.31E+08	1.36E+08	3.48E+08
		LS-CV	2.14E+05	1.44E+05	3.66E+05	2.79E+08	1.53E+08	3.84E+08
n=50	**nl=0.1**	**LS**	2.25E+05	1.73E+05	3.15E+05	2.10E+08	1.58E+08	2.76E+08
		LS-CV	2.39E+05	1.68E+05	3.21E+05	2.29E+08	1.62E+08	3.28E+08
	nl=0.2	**LS**	1.91E+05	1.22E+05	3.00E+05	2.03E+08	1.32E+08	3.44E+08
		LS-CV	2.16E+05	1.49E+05	3.24E+05	2.20E+08	1.40E+08	3.61E+08
	nl=0.3	**LS**	1.66E+05	1.09E+05	3.19E+05	2.38E+08	1.60E+08	3.46E+08
		LS-CV	2.11E+05	1.35E+05	3.50E+05	2.00E+08	1.29E+08	3.39E+08
	nl=0.5	**LS**	1.40E+05	1.00E+05	2.92E+05	1.95E+08	1.48E+08	3.40E+08
		LS-CV	2.03E+05	1.26E+05	3.48E+05	2.01E+08	1.32E+08	3.67E+08
n=25	**nl=0.1**	**LS**	2.20E+05	1.41E+05	3.04E+05	1.41E+08	1.02E+08	2.96E+08
		LS-CV	2.41E+05	1.50E+05	3.24E+05	2.00E+08	1.32E+08	3.18E+08
	nl=0.2	**LS**	1.39E+05	1.01E+05	2.89E+05	1.92E+08	1.21E+08	3.24E+08
		LS-CV	1.84E+05	1.31E+05	3.08E+05	2.66E+08	1.50E+08	3.64E+08
	nl=0.3	**LS**	1.38E+05	9.57E+04	2.91E+05	1.38E+08	9.78E+07	3.00E+08
		LS-CV	1.69E+05	1.32E+05	3.07E+05	1.75E+08	1.02E+08	3.56E+08
	nl=0.5	**LS**	1.26E+05	9.29E+04	2.77E+05	2.01E+08	1.10E+08	3.76E+08
		LS-CV	1.86E+05	1.21E+05	3.44E+05	2.28E+08	1.03E+08	3.98E+08

Appendix Table 9 Derived kinetic parameters – LS and LS-CV methods (cont'd.)

Dataset		Meth.	$E_{a,fwd}$		
			mean	min	max
n=100	nl=0.1	LS	4.94E+04	4.89E+04	5.11E+04
		LS-CV	4.96E+04	4.84E+04	5.27E+04
	nl=0.2	LS	4.89E+04	4.63E+04	5.44E+04
		LS-CV	4.93E+04	4.54E+04	5.52E+04
	nl=0.3	LS	4.80E+04	4.42E+04	5.27E+04
		LS-CV	4.89E+04	4.42E+04	5.31E+04
	nl=0.5	LS	4.65E+04	4.31E+04	5.35E+04
		LS-CV	4.79E+04	4.36E+04	5.34E+04
n=50	nl=0.1	LS	4.91E+04	4.78E+04	5.15E+04
		LS-CV	4.93E+04	4.73E+04	5.14E+04
	nl=0.2	LS	4.84E+04	4.68E+04	5.19E+04
		LS-CV	4.88E+04	4.71E+04	5.26E+04
	nl=0.3	LS	4.76E+04	4.63E+04	5.29E+04
		LS-CV	4.83E+04	4.62E+04	5.36E+04
	nl=0.5	LS	4.68E+04	4.44E+04	5.35E+04
		LS-CV	4.77E+04	4.39E+04	5.33E+04
n=25	nl=0.1	LS	4.82E+04	4.66E+04	5.09E+04
		LS-CV	4.83E+04	4.60E+04	5.13E+04
	nl=0.2	LS	4.74E+04	4.53E+04	5.12E+04
		LS-CV	4.84E+04	4.53E+04	5.20E+04
	nl=0.3	LS	4.60E+04	4.34E+04	5.18E+04
		LS-CV	4.78E+04	4.40E+04	5.20E+04
	nl=0.5	LS	4.42E+04	4.13E+04	5.14E+04
		LS-CV	4.69E+04	4.19E+04	5.25E+04

Bibliography

1. Chong ZR, Yang SHB, Babu P, Linga P, Li XS. Review of natural gas hydrates as an energy resource: Prospects and challenges. *Applied Energy.* 2016;162:1633-1652.

2. Amghizar I, Vandewalle LA, Van Geem KM, Marin GB. New Trends in Olefin Production. *Engineering-Prc.* 2017;3(2):171-178.

3. Wang B, Albarracín-Suazo S, Pagán-Torres Y, Nikolla E. Advances in methane conversion processes. *Catalysis Today.* 2017;285:147-158.

4. Kumar G, Lau SLJ, Krcha MD, Janik MJ. Correlation of Methane Activation and Oxide Catalyst Reducibility and Its Implications for Oxidative Coupling. *Acs Catalysis.* 2016;6(3):1812-1821.

5. Galadima A, Muraza O. Revisiting the oxidative coupling of methane to ethylene in the golden period of shale gas: A review. *Journal of Industrial and Engineering Chemistry.* 2016;37:1-13.

6. Alvarez-Galvan MC, Mota N, Ojeda M, Rojas S, Navarro RM, Fierro JLG. Direct methane conversion routes to chemicals and fuels. *Catalysis Today.* 2011;171(1):15-23.

7. Kondratenko EV, Baerns M. Catalysis of Oxidative Methane Conversions. 2011:35-55.

8. Hammond C, Conrad S, Hermans I. Oxidative methane upgrading. *ChemSusChem.* 2012;5(9):1668-1686.

9. Gambo Y, Jalil AA, Triwahyono S, Abdulrasheed AA. Recent advances and future prospect in catalysts for oxidative coupling of methane to ethylene: A review. *Journal of Industrial and Engineering Chemistry.* 2017.

10. Zavyalova U, Holena M, Schlögl R, Baerns M. Statistical analysis of past catalytic data on oxidative methane coupling for new insights into the composition of high-performance catalysts. *ChemCatChem.* 2011;3(12):1935-1947.

11. Farrell BL, Igenegbai VO, Linic S. A viewpoint on direct methane conversion to ethane and ethylene using oxidative coupling on solid catalysts. In: ACS Publications; 2016.

12. Arndt S, Otremba T, Simon U, Yildiz M, Schubert H, Schomacker R. Mn-Na2WO4/SiO2 as Catalyst for the Oxidative Coupling of Methane. What is Really Known? *Applied Catalysis a-General.* 2012;425:53-61.

13. Pak S, Qiu P, Lunsford JH. Elementary reactions in the oxidative coupling of methane over Mn/Na2WO4/SiO2 and Mn/Na2WO4/MgO catalysts. *Journal of Catalysis.* 1998;179(1):222-230.

14. Wang DJ, Rosynek MP, Lunsford JH. Oxidative coupling of methane over oxide-supported sodium-manganese catalysts. *Journal of Catalysis.* 1995;157(1):270-270.

15. Chen S, Zhang Y, Wu M, Fang W, Yang Y. Study on methanethiol synthesis from H2S and dimethyl sulfide over Al2O3 catalysts promoted with phosphorus. *Applied Catalysis A: General.* 2012;431:151-156.

16. Jankowski J, Kubińska M, Zduńczyk Z. Nutritional and immunomodulatory function of methionine in poultry diets–a review. *Annals of Animal Science.* 2014;14(1):17-32.

17. Bunchasak C. Role of dietary methionine in poultry production. *The Journal of Poultry Science.* 2009;46(3):169-179.

18. Redlingshöfer H, Weckbecker C, Dörflein A, Rückriegel M. Catalyst for the synthesis of alkyl mercaptan and process for the production thereof. In: Google Patents; 2009.

19. Sauer J, Von Hippel L, Arntz D, Boeck W. Catalyst, process for its preparation, and use for synthesis of methyl mercaptan. In: Google Patents; 1999.

20. Brand A, Quaschning V. Catalyst for the production of methyl mercaptan from methanol and hydrogen sulfide. In: Google Patents; 2010.

21. Gutiérrez OY, Kaufmann C, Hrabar A, Zhu Y, Lercher JA. Synthesis of methyl mercaptan from carbonyl sulfide over sulfide K2MoO4/SiO2. *Journal of catalysis.* 2011;280(2):264-273.

22. Kramer RL, Reid EE. THE CATALYTIC PREPARATION OF MERCAPTANS. *Journal of the American Chemical Society.* 1921;43(4):880-890.

23. Choi Y, Stenger HG. Water gas shift reaction kinetics and reactor modeling for fuel cell grade hydrogen. *Journal of Power Sources.* 2003;124(2):432-439.

24. Geyer CJ. Practical markov chain monte carlo. *Statistical science.* 1992:473-483.

25. Whitley D. A genetic algorithm tutorial. *Statistics and computing.* 1994;4(2):65-85.

26. Doornkamp C, Ponec V. The Universal Character of the Mars and Van Krevelen Mechanism. *J Mol Catal a-Chem.* 2000;162(1-2):19-32.

27. Lee JS, Oyama ST. Oxidative coupling of methane to higher hydrocarbons. *Catalysis Reviews-Science and Engineering.* 1988;30(2):249-280.

28. Gholipour Z, Malekzadeh A, Hatami R, Mortazavi Y, Khodadadi A. Oxidative coupling of methane over (Na2WO4+Mn or Ce)/SiO2 catalysts: In situ measurement of electrical conductivity. *Journal of Natural Gas Chemistry.* 2010;19(1):35-42.

29. Sinev MY, Fattakhova ZT, Lomonosov VI, Gordienko YA. Kinetics of oxidative coupling of methane: Bridging the gap between comprehension and description. *Journal of Natural Gas Chemistry.* 2009;18(3):273-287.

30. Iglesia KTaE. Mechanistic Aspects and Reaction Pathways for Oxidative Coupling of Methane on Mn Na2WO4 SiO2 Catalysts. *J Phys Chem C.* 2009;113:10131–10145.

31. Otsuka K, Jinno K, Morikawa A. active and selective catalysts for the synthesis of C2H4 and C2H6 via oxidative coupling of methane. *Journal of Catalysis.* 1986;100(2):353-359.

32. Labinger JA. Oxidative coupling of methane: An inherent limit to selectivity? *Catalysis Letters 1.* 1988;1:371-376.

33. Keller GE, Bhasin MM. Synthesis of ethylene via oxidative coupling of methane .1. Determination of active catalysts. *Journal of Catalysis.* 1982;73(1):9-19.

34. Pieter M. Couwenberg QCaGBM. Irreducible Mass-Transport Limitations during a Heterogeneously Catalyzed Gas-Phase Chain Reaction: Oxidative Coupling of Methane. *Ind Eng Chem Res.* 1996;35:415-421.

35. Horn R, Schlogl R. Methane Activation by Heterogeneous Catalysis. *Catalysis Letters.* 2015;145(1):23-39.

36. Jiang ZC, Yu CJ, Fang XP, Li SB, Wang HL. Oxide support interaction and surface reconstruction in the Na2WO4/SiO2 system. *Journal of Physical Chemistry.* 1993;97(49):12870-12875.

37. Wu JG, Li SB, Niu JZ, Fang XP. Mechanistic Study of Oxidative Coupling of Methane over Mn2O3-Na2WO4/SiO2 Catalyst. *Applied Catalysis a-General.* 1995;124(1):9-18.

38. Fleischer V, Steuer R, Parishan S, Schomäcker R. Investigation of the Surface Reaction Network of the Oxidative Coupling of Methane over Na2WO4/Mn/SiO2 Catalyst by Temperature Programmed and Dynamic Experiments. *Journal of Catalysis.* 2016;341:91-103.

39. Liu Y, Xue J, Liu X, Hou R, Li S. Oxidative dehydrogenation of ethane over Na2WO4-Mn/SiO2 catalyst using oxygen and carbon dioxide as oxidants. 1998;119:593-597.

40. Wang D.J. RMP, Lunsford J.H. Oxidative coupling of methane over Na2WO4 CeO2 and related catalysts. *Journal of Catalysis.* 1995;155(2):390-402.

41. Yunarti RT, Gu S, Choi J-W, Jae J, Suh DJ, Ha J-M. Oxidative Coupling of Methane Using Mg/Ti-Doped SiO2-Supported Na2WO4/Mn Catalysts. *ACS Sustainable Chemistry & Engineering.* 2017;5(5):3667-3674.

42. Shahri SMK, Pour AN. Ce-promoted Mn/Na2WO4/SiO2 catalyst for oxidative coupling of methane at atmospheric pressure. *Journal of Natural Gas Chemistry.* 2010;19(1):47-53.

43. Takanabe K, Iglesia E. Rate and selectivity enhancements mediated by OH radicals in the oxidative coupling of methane catalyzed by Mn/Na2WO4/SiO2. *Angew Chem Int Ed Engl.* 2008;47(40):7689-7693.

44. Fleischer V, Littlewood P, Parishan S, Schomäcker R. Chemical Looping as Reactor Concept for the Oxidative Coupling of Methane over a Na2WO4/Mn/SiO2 Catalyst. *Chemical Engineering Journal.* 2016;306:646-654.

45. Mazzara C, Jupille J, Flank AM, Lagarde P. Stereochemical order around sodium in amorphous silica. *J Phys Chem B.* 2000;104(15):3438-3445.

46. Palermo A, Vazquez JPH, Lee AF, Tikhov MS, Lambert RM. Critical influence of the amorphous silica-to-cristobalite phase transition on the performance of Mn/Na2WO4/SiO2 catalysts for the oxidative coupling of methane. *Journal of Catalysis.* 1998;177(2):259-266.

47. Fang XP, Li SB, Lin JZ, Chu YL. Preparation and Characterization of W-Mn Catalysis for Oxidative Coupling of Methane. *Journal of Molecular Catalysis (China).* 1992;6:427–433.

48. Jiang Z-C, Yu C-J, Fang X-P, Li S-B, Wang H-L. Oxide support interaction and surface reconstruction in the sodium tungstate (Na2WO4) silica system. *J Phys Chem.* 1993;97:12870-12875.

49. Jiang ZC, Gong H, Li SB. Methane activation over Mn2O3-Na2WO4/SiO2 catalyst and oxygen spillover. *Spillover and Migration of Surface Species on Catalysts.* 1997;112:481-490.

50. Salehoun V, Khodadadi A, Mortazavi Y, Talebizadeh A. Dynamics of Mn/Na2WO4/SiO2 catalyst in oxidative coupling of methane. *Chem Eng Sci.* 2008;63(20):4910-4916.

51. Sundqvist S, Arjmand M, Mattisson T, Ryden M, Lyngfelt A. Screening of different manganese ores for chemical-looping combustion (CLC) and chemical-looping with oxygen uncoupling (CLOU). *Int J Greenh Gas Con.* 2015;43:179-188.

52. Shulman A, Cleverstam E, Mattisson T, Lyngfelt A. Manganese/Iron, Manganese/Nickel, and Manganese/Silicon Oxides Used in Chemical-Looping With Oxygen Uncoupling (CLOU) for Combustion of Methane. *Energ Fuel.* 2009;23(10):5269-5275.

53. Pak S, Lunsford JH. Thermal effects during the oxidative coupling of methane over Mn/Na2WO4/SiO2 and Mn/Na2WO4/MgO catalysts. *Applied Catalysis A: General.* 1998;168(1):131-137.

54. Wang SB, Zhu ZH. Catalytic conversion of alkanes to olefins by carbon dioxide oxidative dehydrogenation - A review. *Energ Fuel.* 2004;18(4):1126-1139.

55. Terayama K, Ikeda M. Study on thermal decomposition of MnO2 and Mn2O3 by thermal analysis. *Transactions of the Japan institute of metals.* 1983;24(11):754-758.

56. Dose WM, Donne SW. Manganese Dioxide Structural Effects on its Thermal Decomposition. *Materials Science and Engineering: B.* 2011;176(15):1169-1177.

57. Werny MJ, Wang Y, Girgsdies F, Schlögl R, Trunschke A. Fluctuating Storage of the Active Phase in a Mn-Na2WO4/SiO2 Catalyst for the Oxidative Coupling of Methane. *Angewandte Chemie.* 2020;132(35):15031-15036.

58. Takanabe K, Khan AM, Tang Y, et al. Integrated in situ characterization of a molten salt catalyst surface: evidence of sodium peroxide and hydroxyl radical formation. *Angewandte Chemie.* 2017;129(35):10539-10543.

59. Sinev M, Ponomareva E, Sinev I, et al. Oxygen pathways in oxidative coupling of methane and related processes. Case study: NaWMn/SiO2 catalyst. *Catalysis Today.* 2019;333:36-46.

60. Stauffer JE. Methyl mercaptan process. In: Google Patents; 2008.

61. Folkins HO, Miller EL. Synthesis of mercaptans. *Industrial & Engineering Chemistry Process Design and Development.* 1962;1(4):271-276.

62. Barrault J, Boulinguiez M, Forquy C, Maurel R. Synthesis of methyl mercaptan from carbon oxides and H2S with tungsten—alumina catalysts. *Applied catalysis.* 1987;33(2):309-330.

63. Willke T. Methionine production—a critical review. *Applied microbiology and biotechnology.* 2014;98(24):9893-9914.

64. Alexandratos N, Bruinsma J. World agriculture towards 2030/2050: the 2012 revision. 2012.

65. Fanatico A, Arsi K, Upadhyaya I, Ramos JM, Donoghue D, Donoghue A. Sustainable fish and invertebrate meals for methionine and protein feeds in organic poultry production. *Journal of Applied Poultry Research.* 2018;27(4):437-448.

66. Feltrin AN. Energy Equality and the Challenges of Population Growth. *Rel: Beyond Anthropocentrism.* 2018;6:313.

67. Sauer J, Boeck W, Von Hippel L, et al. Catalyst, process for its preparation, and use for synthesis of methyl mercaptan. In: Google Patents; 1998.

68. Hofen W, Boeck W, Rautenberg S, et al. Process for separating the product gas mixture from the catalytic synthesis of methyl mercaptan. In: Google Patents; 1999.

69. Khankal R, Henry H, Hasenberg DM, Barry CM, Refvik MD, Hankinson MS. Process for Conversion of Dimethyl Sulfide to Methyl Mercaptan. In: Google Patents; 2018.

70. Chen S, Wang W, Zhang Y, Wei Y, Fang W, Yang Y. Thiolation of dimethyl sulfide to methanethiol over WO3/ZrO2 catalysts. *Journal of Molecular Catalysis A: Chemical.* 2012;365:60-65.

71. Hawkins DM. The problem of overfitting. *Journal of chemical information and computer sciences.* 2004;44(1):1-12.

72. Brendel M, Mhamdi A, Bonvin D, Marquardt W. An incremental approach for the identification of reaction kinetics. *IFAC Proceedings Volumes.* 2004;37(1):173-178.

73. Hasdemir D, Hoefsloot HC, Smilde AK. Validation and selection of ODE based systems biology models: how to arrive at more reliable decisions. *BMC systems biology.* 2015;9(1):32.

74. Hasdemir D, Hoefsloot HC, Westerhuis JA, Smilde AK. How informative is your kinetic model?: using resampling methods for model invalidation. *BMC systems biology.* 2014;8(1):61.

75. Barnard JP, Aldrich C, Gerber M. Identification of dynamic process systems with surrogate data methods. *AIChE Journal.* 2001;47(9):2064-2075.

76. Hsu C-W, Chang C-C, Lin C-J. A practical guide to support vector classification. 2003.

77. Kim J-H. Estimating classification error rate: Repeated cross-validation, repeated hold-out and bootstrap. *Computational statistics & data analysis.* 2009;53(11):3735-3745.

78. Yadav S, Shukla S. Analysis of k-fold cross-validation over hold-out validation on colossal datasets for quality classification. Paper presented at: 2016 IEEE 6th International Conference on Advanced Computing (IACC)2016.

79. Wong T-T. Performance evaluation of classification algorithms by k-fold and leave-one-out cross validation. *Pattern Recognition.* 2015;48(9):2839-2846.

80. Rodriguez JD, Perez A, Lozano JA. Sensitivity analysis of k-fold cross validation in prediction error estimation. *IEEE transactions on pattern analysis and machine intelligence.* 2009;32(3):569-575.

81. Fushiki T. Estimation of prediction error by using K-fold cross-validation. *Statistics and Computing.* 2011;21(2):137-146.

82. Mashkina A. Synthesis of methylmercaptan from methanol and hydrogen sulfide at elevated pressure on an industrial catalyst. *Petroleum Chemistry.* 2006;46(1):28-33.

83. Sandler SI. *Using Aspen Plus in thermodynamics instruction: a step-by-step guide.* John Wiley & Sons; 2015.

84. Stryjek R, Vera J. PRSV: An improved Peng—Robinson equation of state for pure compounds and mixtures. *The canadian journal of chemical engineering.* 1986;64(2):323-333.

85. Mathias PM, Copeman TW. Extension of the Peng-Robinson equation of state to complex mixtures: evaluation of the various forms of the local composition concept. *Fluid Phase Equilibria.* 1983;13:91-108.

86. Westhaus U, Dröge T, Sass R. DETHERM®—a thermophysical property database. *Fluid phase equilibria.* 1999;158:429-435.

87. Mears DE. Tests for transport limitations in experimental catalytic reactors. *Industrial & Engineering Chemistry Process Design and Development.* 1971;10(4):541-547.

88. Weisz P, Prater C. Interpretation of measurements in experimental catalysis. *Adv Catal.* 1954;6(143):60390-60399.

89. Moré JJ. The Levenberg-Marquardt algorithm: implementation and theory. In: *Numerical analysis.* Springer; 1978:105-116.

90. Browne MW. Cross-validation methods. *Journal of mathematical psychology.* 2000;44(1):108-132.

91. Niu M, Li Y, Wang C, Han K. RFAmyloid: a web server for predicting amyloid proteins. *International journal of molecular sciences.* 2018;19(7):2071.

92. Bauer R. Schlunder, effective radial thermal conductivity of packings in gas flow. Part II thermal conductivity of the packing fraction without gas flow. *International Chemical Engineering.* 1978;18:189-204.

93. Ergun S. Fluid flow through packed columns. *Chem Eng Prog.* 1952;48:89-94.

94. Peng D-Y, Robinson DB. A new two-constant equation of state. *Industrial & Engineering Chemistry Fundamentals.* 1976;15(1):59-64.

95. Daubert TE. Physical and thermodynamic properties of pure chemicals: data compilation. *Design Institute for Physacal Property Data (DIPPR).* 1989.

96. Reid RC, Prausnitz JM, Poling BE. The properties of gases and liquids. 1987.

97. Mason E, Saxena S. Approximate formula for the thermal conductivity of gas mixtures. *The Physics of fluids.* 1958;1(5):361-369.

98. Khankal R, Henry H, Hasenberg DM, Barry CM, Refvik MD, Hankinson MS. Process for conversion of dimethyl sulfide to methyl mercaptan. In: Google Patents; 2019.

99. Pichai P, Rolston J, Schubert S, et al. Process for producing methyl mercaptan from dimethyl sulfide. In: Google Patents; 2020.

100. Levenspiel O. Chemical reaction engineering. *Industrial & engineering chemistry research.* 1999;38(11):4140-4143.

101. Davis ME, Davis RJ. *Fundamentals of chemical reaction engineering.* Courier Corporation; 2012.

102. Fogler HS. *Essentials of Chemical Reaction Engineering: Essenti Chemica Reactio Engi.* Pearson Education; 2010.

103. Matera S, Schneider WF, Heyden A, Savara A. Progress in accurate chemical kinetic modeling, simulations, and parameter estimation for heterogeneous catalysis. *ACS Catalysis.* 2019;9(8):6624-6647.

104. Maria G. A review of algorithms and trends in kinetic model identification for chemical and biochemical systems. *Chemical and Biochemical Engineering Quarterly.* 2004;18(3):195-222.

105. Labovský J, Švandová Z, Markoš J, Jelemenský Lu. Mathematical model of a chemical reactor—useful tool for its safety analysis and design. *Chem Eng Sci.* 2007;62(18-20):4915-4919.

106. Hougen OA, Watson KM. *Chemical process principles.* Vol 1: J. Wiley & Sons, inc.; 1943.

107. Smith JM. *Chemical engineering kinetics.* 1981.

108. Sinnott R. *Chemical engineering design.* Vol 6: Elsevier; 2014.

109. Buzzi-Ferraris G, Manenti F. *Interpolation and regression models for the chemical engineer: Solving numerical problems.* John Wiley & Sons; 2010.

110. Hill CG, Root TW. *An introduction to chemical engineering kinetics & reactor design.* Wiley Online Library; 1977.

111. Venkatasubramanian V. The promise of artificial intelligence in chemical engineering: Is it here, finally? *AIChE Journal.* 2019;65(2):466-478.

112. Kano M, Nakagawa Y. Data-based process monitoring, process control, and quality improvement: Recent developments and applications in steel industry. *Computers & Chemical Engineering.* 2008;32(1-2):12-24.

113. Martín M, Adams II TA. Challenges and future directions for process and product synthesis and design. *Computers & Chemical Engineering.* 2019;128:421-436.

114. Maria G, Muntean O. Model reduction and kinetic parameters identification for the methanol conversion to olefins. *Chem Eng Sci.* 1987;42(6):1451-1460.

115. Park T-Y, Froment GF. Kinetic modeling of the methanol to olefins process. 2. Experimental results, model discrimination, and parameter estimation. *Industrial & engineering chemistry research.* 2001;40(20):4187-4196.

116. Wolberg J. *Data analysis using the method of least squares: extracting the most information from experiments.* Springer Science & Business Media; 2006.

117. Singer AB, Taylor JW, Barton PI, Green WH. Global dynamic optimization for parameter estimation in chemical kinetics. *The Journal of Physical Chemistry A.* 2006;110(3):971-976.

118. Wang F-S, Su T-L, Jang H-J. Hybrid differential evolution for problems of kinetic parameter estimation and dynamic optimization of an ethanol fermentation process. *Industrial & engineering chemistry research.* 2001;40(13):2876-2885.

119. Eftaxias A, Font J, Fortuny A, Fabregat A, Stüber F. Nonlinear kinetic parameter estimation using simulated annealing. *Computers & chemical engineering.* 2002;26(12):1725-1733.

120. Albrecht J. Estimating reaction model parameter uncertainty with Markov Chain Monte Carlo. *Computers & Chemical Engineering.* 2013;48:14-28.

121. Zhang LA, Urbano A, Clermont G, Swigon D, Banerjee I, Parker RS. APT-MCMC, a C++/Python implementation of Markov Chain Monte Carlo for parameter identification. *Computers & chemical engineering.* 2018;110:1-12.

122. Khansary MA, Sani AH. Using genetic algorithm (GA) and particle swarm optimization (PSO) methods for determination of interaction parameters in multicomponent systems of liquid–liquid equilibria. *Fluid Phase Equilibria.* 2014;365:141-145.

123. Mühlenbein H, Schomisch M, Born J. The parallel genetic algorithm as function optimizer. *Parallel computing.* 1991;17(6-7):619-632.

124. Qin SJ, Chiang LH. Advances and opportunities in machine learning for process data analytics. *Computers & Chemical Engineering.* 2019;126:465-473.

125. Qin SJ. Process data analytics in the era of big data. In: Wiley Online Library; 2014.

126. Himmelblau DM. Accounts of experiences in the application of artificial neural networks in chemical engineering. *Industrial & Engineering Chemistry Research.* 2008;47(16):5782-5796.

127. Himmelblau DM. Applications of artificial neural networks in chemical engineering. *Korean journal of chemical engineering.* 2000;17(4):373-392.

128. Bonvin D, Georgakis C, Pantelides C, et al. Linking models and experiments. *Industrial & Engineering Chemistry Research.* 2016;55(25):6891-6903.

129. McLean KA, McAuley KB. Mathematical modelling of chemical processes—obtaining the best model predictions and parameter estimates using identifiability and estimability procedures. *The Canadian Journal of Chemical Engineering.* 2012;90(2):351-366.

130. Graciano J, Mendoza DF, Le Roux GA. Performance comparison of parameter estimation techniques for unidentifiable models. *Computers & Chemical Engineering.* 2014;64:24-40.

131. Foss BA, Lohmann B, Marquardt W. A field study of the industrial modeling process. 1998.

132. Hawkins DM, Kraker J. Deterministic fallacies and model validation. *Journal of chemometrics.* 2010;24(3-4):188-193.

133. Tan N, Rao H, Li Z, Li X. Prediction of chemical carcinogenicity by machine learning approaches. *SAR and QSAR in Environmental Research.* 2009;20(1-2):27-75.

134. Martin TM, Harten P, Young DM, et al. Does rational selection of training and test sets improve the outcome of QSAR modeling? *Journal of chemical information and modeling.* 2012;52(10):2570-2578.

135. Kohavi R. A study of cross-validation and bootstrap for accuracy estimation and model selection. Paper presented at: Ijcai1995.

136. Kulkarni A, Jayaraman VK, Kulkarni BD. Support vector classification with parameter tuning assisted by agent-based technique. *Computers & chemical engineering.* 2004;28(3):311-318.

137. Pirdashti M, Curteanu S, Kamangar MH, Hassim MH, Khatami MA. Artificial neural networks: applications in chemical engineering. *Reviews in Chemical Engineering.* 2013;29(4):205-239.

138. Stone M. Cross-validatory choice and assessment of statistical predictions. *Journal of the Royal Statistical Society: Series B (Methodological).* 1974;36(2):111-133.

139. Kim M, Lee Y-H, Han C. Real-time classification of petroleum products using near-infrared spectra. *Computers & Chemical Engineering.* 2000;24(2-7):513-517.

140. Coley CW, Green WH, Jensen KF. Machine learning in computer-aided synthesis planning. *Accounts of chemical research.* 2018;51(5):1281-1289.

141. Coley CW, Barzilay R, Jaakkola TS, Green WH, Jensen KF. Prediction of organic reaction outcomes using machine learning. *ACS central science.* 2017;3(5):434-443.

142. Marquardt DW. An algorithm for least-squares estimation of nonlinear parameters. *Journal of the society for Industrial and Applied Mathematics.* 1963;11(2):431-441.

143. Roy A, Clermont G, Daun S, Parker RS. A mathematical model of acute inflammatory response to endotoxin challenge. Paper presented at: AIChE Annual Meeting, Salt Lake City, UT, 538pp2007.

144. Zak DE, Stelling J, Doyle III FJ. Sensitivity analysis of oscillatory (bio) chemical systems. *Computers & chemical engineering.* 2005;29(3):663-673.

145. Kreutz C, Raue A, Kaschek D, Timmer J. Profile likelihood in systems biology. *The FEBS journal.* 2013;280(11):2564-2571.

146. Lilliefors HW. On the Kolmogorov-Smirnov test for normality with mean and variance unknown. *Journal of the American statistical Association.* 1967;62(318):399-402.

147. Massey Jr FJ. The Kolmogorov-Smirnov test for goodness of fit. *Journal of the American statistical Association.* 1951;46(253):68-78.

148. Neyman J. On the two different aspects of the representative method: the method of stratified sampling and the method of purposive selection. In: *Breakthroughs in Statistics.* Springer; 1992:123-150.

149. Hastings WK. Monte Carlo sampling methods using Markov chains and their applications. 1970.

150. Chib S, Greenberg E. Understanding the metropolis-hastings algorithm. *The american statistician.* 1995;49(4):327-335.

151. Van Laarhoven PJ, Aarts EH. Simulated annealing. In: *Simulated annealing: Theory and applications.* Springer; 1987:7-15.

152. Stein M. Large sample properties of simulations using Latin hypercube sampling. *Technometrics.* 1987;29(2):143-151.

153. Raue A, Kreutz C, Maiwald T, et al. Structural and practical identifiability analysis of partially observed dynamical models by exploiting the profile likelihood. *Bioinformatics.* 2009;25(15):1923-1929.

154. Young LC, Finlayson BA. Axial dispersion in nonisothermal packed bed chemical reactors. *Industrial & Engineering Chemistry Fundamentals.* 1973;12(4):412-422.

155. Wilkes JO, Birmingham SG. *Fluid Mechanics for Chemical Engineers with Microfluidics and CFD.* Pearson Education; 2006.

156. Aly FA, Lee LL. Self-consistent equations for calculating the ideal gas heat capacity, enthalpy, and entropy. *Fluid Phase Equilibria.* 1981;6(3-4):169-179.

157. Chase Jr M, Curnutt J, McDonald R, Syverud A. JANAF thermochemical tables, 1978 supplement. *Journal of Physical and Chemical Reference Data.* 1978;7(3):793-940.

158. Chase Jr M, Curnutt JL, Downey Jr J, McDonald R, Syverud A, Valenzuela E. JANAF thermochemical tables, 1982 supplement. *Journal of physical and chemical reference data.* 1982;11(3):695-940.

159. Kyle BG. Chemical and process thermodynamics. 1984.